NORTHWESTERN UNIVERSITY

Pushing the Limits on Metal–Organic Frameworks as Catalyst Supports: Small Hydrocarbons Reactions over NU-1000-Supported Catalysts

A DISSERTATION

SUBMITTED TO THE GRADUATE SCHOOL
IN PARTIAL FULFILLMENT OF THE REQUIREMENTS

for the degree of

DOCTOR OF PHILOSOPHY

Field of Chemical and Biological Engineering

by

Sol Ahn

EVANSTON, ILLINOIS

June 2019

Abstract

Heterogeneous catalysts based on metal oxides are of significant interest for many industrial chemical reactions. These catalysts, however, often suffer from ill-defined structures that preclude better understanding of the surface phenomena. Thus, structurally well-defined catalysts have received growing attention by making it feasible to understand the kinetics and reaction mechanisms. Structurally precise catalysts can be achieved by utilization of atomically controlled synthesis technologies and/or structurally well-defined catalyst supports. Zr based metal–organic framework (MOF), NU-1000 (NU stands for Northwestern University) is a suitable candidate for the well-defined catalyst support as grafting sites are regularly ordered and isolated from each other. This dissertation seeks to develop a more fundamental understanding of how NU-1000-supported metal oxide catalysts serve as well-defined analogs to conventional metal oxide catalysts.

Chapter 1 introduces the reason why NU-1000 is one good candidate as a catalyst support and presents a synthesis protocol, post-modification methods, physicochemical properties (given by N_2 isotherm, powder x-ray diffraction, diffuse reflectance infrared Fourier transform spectroscopy, scanning electron microscopy), and additional characterization methods (x-ray absorption spectroscopy and difference envelope density measurements) to investigate structures upon modification of NU-1000. Lastly, this part enumerates examples of application of NU-1000-supported metal oxides as heterogeneous catalysts.

Chapter 2 through Chapter 4 focus on my own contribution to develop synthesis-structure-activity relationships of NU-1000-supported metal oxide catalysts in small hydrocarbon reactions. To be specific, Chapter 2 presents NU-1000-supported Nb oxide as Lewis acid catalysts to study H_2O_2 activation in the condensed-phase cyclohexene epoxidation. Since NU-1000 provides

isolated grafting sites, almost all Nb oxide sites are accessible despite high Nb loading. In Chapter 3, motivated to further understand H_2O_2 activation in the vapor-phase, our team has built a vapor-phase hydrogen peroxide reactor, and we study kinetics and selectivity trends of the same epoxidation reaction over supported metal oxide catalysts, which are Ti or Nb grafted on SiO_2 and NU-1000 supports. Moreover, Chapter 4 discusses pushing the limit of NU-1000 as a catalyst support under harsh reaction conditions to investigate the applicability as a solid acid catalyst through installing isolated W oxide or clusters of W oxide in NU-1000, and then by testing isomerization and disproportionation of *o*-xylene as a model reaction. Separately, the Appendix summarizes my collaborating works with other research groups to develop understanding of MOFs as catalysts in oxidation and oxidative dehydrogenation reactions. The synthesis-structure-function relationships developed here have important implications for the rational design of MOFs as catalyst supports in the industrially relevant reactions.

Acknowledgements

First and foremost, thank you and praise God for everything. I know I will never be able to thank you enough for always being there for me. I would like to thank my advisors, Prof. Justin M. Notestein and Prof. Omar K. Farha for your support, guidance, and most importantly your patience. I am always amazed your wealth of knowledge and passion for research every time I meet with you to discuss science. I am a truly lucky person as I have been able to learn from both of you, having you two as role models for my future career. In particular, I will never forget Justin for always being there for me as my father, as my friend, and as my mentor whenever I had to get through all the tough times for the past four years. I can always feel your kindness and friendship regardless of my language barrier. Also, I will miss Omar's tremendous drive, all the chemistry knowledge, and energetic leadership, each of which that I wish to possess one day. I am very much grateful to Prof. Neil M. Schweitzer for teaching me every single detail of instruments and catalysis as well as for your patience every time I bug you. I owe a great deal of thanks to Neil as he answers all of my absurd/repeating questions, and I have learned from you that instruments are not just black boxes which widens my approach to the research. I want to thank Prof. Linda J. Broadbelt for serving on my committee. I will never forget and wish to learn your passion and energy, not just limited to research but also extended to teaching, mentoring, and leadership in chemical engineering community.

To my mentors Dr. Nick E. Thornburg and Dr. Zhanyong Li: thank you for your mentorship and patience. When I started my PhD career, you two were always there for me to help and to answer every single question. I am also grateful to Dr. Scott L. Nauert for your help on my projects with your amazing advice. I would like to thank Dr. Stephanie Kwon for enormous amounts of advice regarding basically everything inside the lab; advice on graduate and post-graduate life as well as especially the trouble shooting of building and running the peroxide reactor, and outside the lab; answering all of my annoying and relentless questions regarding everything. Special thanks to Timothy A. Goetjen for correcting my English. I would like to thank Jian Liu as being one of two members of the 85 club, and I will miss our meaningless chatting and all the jokes. I want to thank Hyunho Noh, Yijing Chen, Xingjie Wang for being my office mates as you guys always bear with my endless complaints about many things. I am very grateful to all other Notestein and Farha group members for helping me to complete this marathon. I would like to express my gratitude to my Korean friends at Northwestern: Musung Kweon, Dongjoon Rhee, June Lee, Dr. Wonbae Bang, Dr. Joohoon Kang. I will never forget all the time we spent together as you encouraged/amused me during my PhD.

To my parents, I will never thank you enough for your support and unconditional love for my life. I owe an inexpressible debt of gratitude. To my brother, thank you for your support and being there for me. I would like to thank my brother-in-law, mother-in-law, and farther-in-law for their prayer and looking out for my family and me. I also owe them a great deal of gratitude. Lastly, but most importantly, I express my gratitude to my beloved wife Yuri Kim and my beloved son Joseph Y. Ahn. We are the best team and you two make me smile under all circumstances. I cannot thank you enough for your support, encouragement, and love. I would not be here without you two. With you, I am not afraid of the future.

Table of Contents

List of Tables

List of Figures

List of Schemes

Chapter 1. NU-1000 as a Catalyst Support

1.1 Introduction

With increasing production of natural gas, its efficient processing provides new opportunities for energy efficiency and resource conservation. Often, natural gas requires conversion to liquid form for ease of storage or transport. One promising treatment is to produce energy carriers from natural gas with the following catalysis; (i) selective oxidation of light alkanes to alcohols, (ii) dehydrogenation of light alkanes to alkene intermediates (also, the reverse reaction), and (iii) selective oligomerization reactions as well as the reverse. To mention a single example, selective oxidation of hydrocarbons is of significant importance, because it provides one of the easiest routes for functionalization of hydrocarbon molecules.[1-3] Subsequently, it has contributed significantly to the development of society today, for its products are incorporated into a large proportion of the materials and commodities in daily use.[4]

In principle, selective oxidation reactions can be catalyzed by heterogeneous catalysts based on metal oxides. From an industrial point of view, heterogeneous catalysts are preferred due to their easy separation from the reactants and products after the chemical process. However, they often have complicated and non-uniform surface structures, including catalytically active sites that are often present as minority species. On the other hand, since homogeneous catalysts have only one well-defined active species in the system, they are able to provide a detailed mechanistic understanding of the catalytic system. Thus, many researchers strive to go beyond typical metal oxide catalysts that are often ill-defined as well as less active when compared to homogeneous catalysts.

Similarly to many heterogeneous catalysts, supported metal oxide catalysts are prepared by depositing and/or reacting organometallic complexes (i.e. metal precursor) on hydroxyl groups of many supports, such as silica, alumina, zirconia, and other metal oxides. These supports play a significant role in the activity and stability of catalysts. These supports, however, have multiple unique hydroxyl groups on their surface. For example, silica, which can be considered as a simple support, has isolated, vicinal, geminal, and nest hydroxyl groups on its surface. The relative amount and distribution of these groups are different. Such surface inhomogeneity obscures both practical catalytic science and better understanding of surface phenomena.[5] As progress in catalysis often emerges from understanding of active sites, many efforts have been made to develop atomically precise supported metal oxide catalysts. This in turn allows the design of a new class of catalysts for better understanding of surface phenomena.

Metal–organic frameworks (MOFs), a class of hybrid porous materials comprised of metal nodes and organic linkers, have crystalline structures. Owing to their well-defined nature as well as high surface area, MOFs have been considered as promising catalytic supports to better understand surface phenomena. Also, they have found potential applications in gas storage and release,[6-9] separation,[10] sensing[11] and catalysis.[12-14] Furthermore, Zr-based MOFs exhibit relatively high chemical,[15-17] thermal,[18-19] and mechanical stability.[19-20] Among the various reported Zr-MOFs, NU-1000, consisting of a Zr_6 node and tetratopic pyrene based linker, can be a suitable candidate for catalytic support due to its high chemical and hydrothermal stability,[21] and relative ease of scalability.[22] In addition, it can be easily modified post-synthetically[23-25] and provides grafting sites for deposited metals,[26] as hydroxyl and aqua groups are present on the Zr_6 nodes (Figure 1.1).[27] Moreover, the lengthy organic linkers provide spacing between adjacent metal nodes (> 1 nm), which minimizes surface diffusion, by means of aggregation, of the active metal ions during post-synthetic treatment and catalysis.[28]

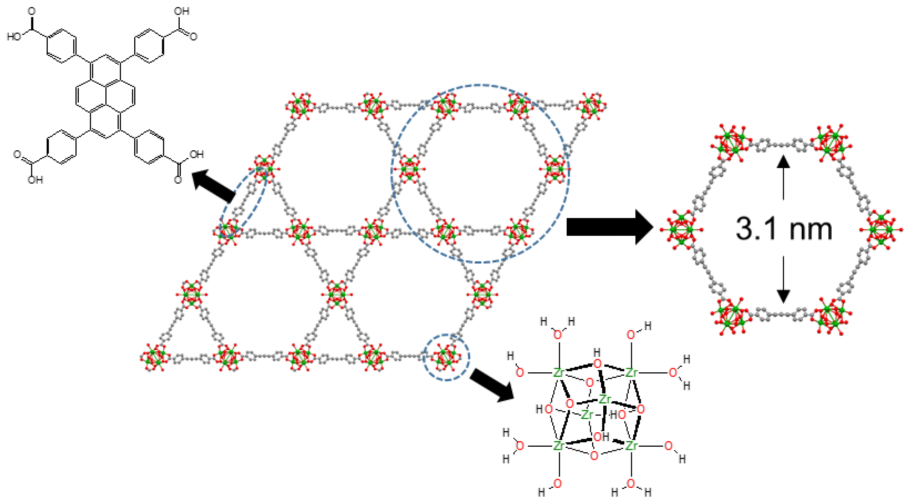

Figure 1.1. Structure of representation of NU-1000, highlighting organic linker (TBAPy^{4-}: 1,3,6, 8-tetrakis(*p*-benzoic acid)pyrene) and Zr_6 node ($[Zr_6(\mu_3\text{-}O)_4(\mu_3\text{-}OH)_4(OH)_4(H_2O)_4]^{8+}$).

1.2 Characterization methods

1.2.1 N_2 isotherm

Surface area is one of the most important descriptors of catalyst supports as it can be used to calculate surface density of metal oxide sites. Surface areas are commonly given as BET (Brunauer, Emmett, and Teller) surface areas calculated by applying the BET equation (considering multilayer adsorption) to N_2 isotherms collected at 77 K.

$$\frac{p/p_o}{v(1-p/p_o)} = \frac{1}{v_m C} + \frac{C-1}{v_m C}(p/p_o)$$

However, when applying the BET equation to calculate surface areas of microporous materials (ex. MOFs and zeolites), the overlap of monolayer formation and pore-filling may invalidate the assumption of BET theory. Thus, it is very important to meet the consistency criteria when applying the BET equation to MOFs.[29] The criteria are given as follows:

(1) The term $v(1 - P/P_o)$ should increase monotonically with P/P_o. ($R^2 > 0.995$)

(2) The C value resulting from the linear regression should be positive.

(3) The monolayer loading (v_m) should correspond to P/P_o falling within the selected range.

(4) P/P_o corresponding to v_m $(1/\sqrt{C}+1)$ should be equal to pressure determined in (3).

Figure 1.2(a) shows N_2 isotherm of NU-1000, and the inset presents the BET plot satisfying the criterion (1) ($0.004 < P/P_o < 0.05$, $R^2=0.9999$). Moreover, the resulting C value is 490 (positive, criterion (2)) as well as 490 cm^3/g STP of v_m is falling within the selected P/P_o range (at $P/P_o \sim 0.045$, criterion (3)). Lastly, the term $(1/\sqrt{C}+1)$ is 0.044 that is very close to P/P_o from (3) (criterion (4)). Based upon the consistency criteria, BET surface area of NU-1000 is 2,140 m^2/g. Pore size distribution can be obtained *via* a fitting of density functional theory (DFT) calculated models. Fitting of the desorption branch isotherm of NU-1000 with DFT models, NU-1000 possess two characteristic pores that are 12 Å and 31 Å (Figure 1.2(b)). Pore sizes from the N_2 isotherm agree well with that from the simulated structure.

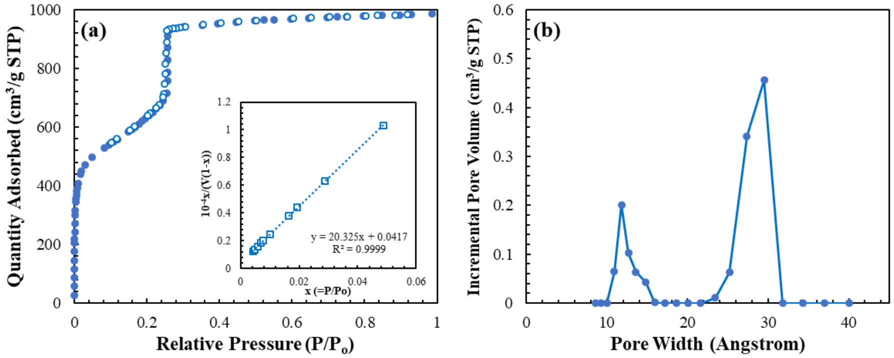

Figure 1.2. (a) N_2 adsorption/desorption isotherm (inset: BET linear plot with a range of $0.004 < P/P_o < 0.05$), and (b) DFT pore size distribution of NU-1000 (carbon slit pore N_2 77 K kernel).

1.2.2 Powder x-ray diffraction

Owing to the crystallinity of MOFs, NU-1000 shows a characteristic powder x-ray diffraction (PXRD) pattern (Figure 1.3). This serves as one of the criteria to roughly examine phase purity upon synthesis. For example, if a peak at 2θ = 5.1 is as high as (or higher than) a peak at 2θ = 2.5, one may assume the presence of the NU-901 phase which possesses same Zr_6 node and linker of NU-1000 but a different topology (Figure 1.4). Moreover, PXRD patterns can serve as a tool for examining integrities of bulk structure upon modification and/or catalysis.

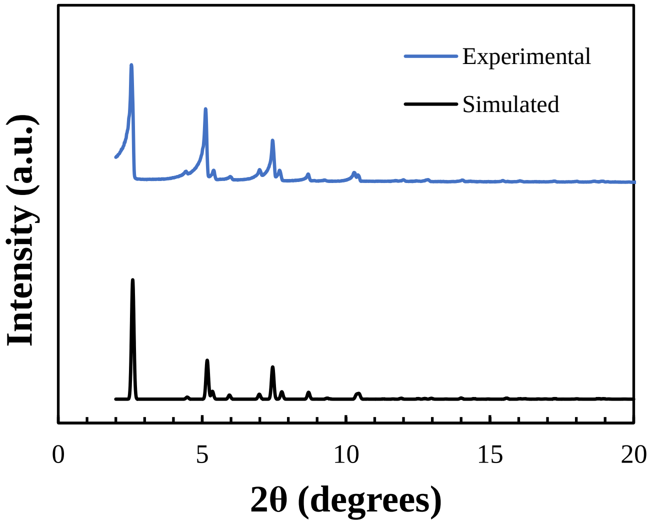

Figure 1.3. PXRD patterns of NU-1000: experimentally measured and simulated patterns.

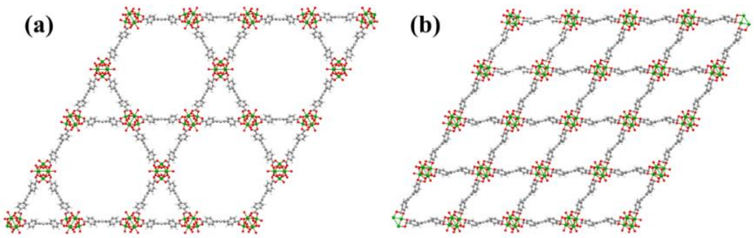

Figure 1.4. Structures of (a) NU-1000 and (b) NU-901 viewed through the c-axis.

1.2.3 Difference envelope density measurement

PXRD patterns can be utilized further to localize electron density of deposited metal oxide in NU-1000. Scheme 1.1 briefly presents how a difference envelope density (DED) map is obtained from PXRD patterns. First, the structure envelope (SE) of parent NU-1000 is required, here the SE is an electron density map derived from the PXRD pattern of parent NU-1000. Second, one needs to collect the PXRD pattern of NU-1000-supported metal oxide to obtain the SE of the modified MOF. By subtracting the electron density contribution from the parent material, we can identify regions of extra electron density upon post modification. This technique is very useful as we can explore the distribution of deposited metal oxide and the lattice perturbation induced by the metal oxide. However, this technique requires the use of a synchrotron x-ray source (0.73 Å) instead of Cu-Kα radiation source (1.54 Å) to obtain higher quality diffraction patterns.

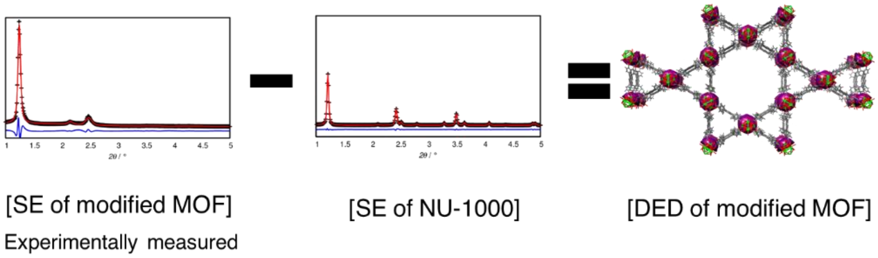

Scheme 1.1. Schematic illustration of DED measurement.

1.2.4 Diffuse reflectance infrared Fourier transform spectroscopy

Characteristic O–H stretch from –OH and H_2O groups on the Zr_6 node can be detected by diffuse reflectance infrared Fourier transform spectroscopy (DRIFTS). Figure 1.5 shows the peak at 3670 cm^{-1} corresponding to –OH and H_2O groups reduces upon dehydration *via* thermal treatment or binding chemically with guest species *via* post-modification. This disappearance is one indicator of modification of NU-1000. Unfortunately, the organic linker prevents extracting useful information from the low wavenumber regime.

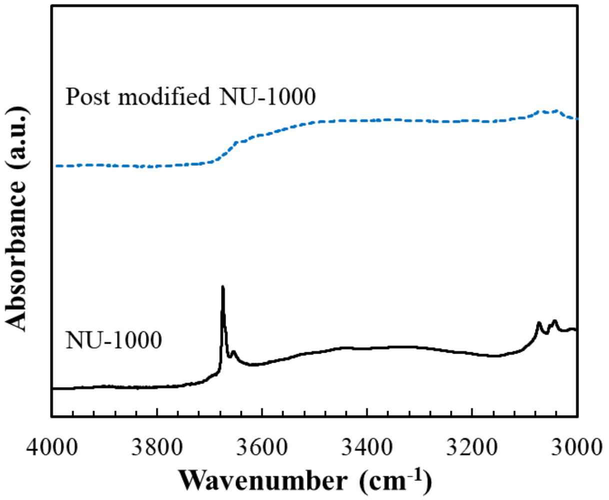

Figure 1.5. DRIFT spectra of post modified NU-1000 and parent NU-1000.

1.2.5 Scanning electron microscopy

Scanning electron microscopy (SEM) images can be a good indicator of phase purity and crystal size, both of which potentially can affect catalytic activity. For instance, if there is NU-901 phase present in the middle of NU-1000 crystal, large organometallic precursor or metal oxide clusters may not be able to diffuse through the middle of the crystal, which results in non-uniform installation of metal oxide along the crystal. Also, crystal size may be critical in terms of reactant/product diffusion under condensed-phase reaction conditions, as NU-1000 crystals can be considered a pseudo-1D porous material. Figure 1.6 illustrates images of both phase impure (Figure 1.6(a)) and phase pure (Figure 1.6(b)) NU-1000 crystals. In addition, energy-dispersive x-ray spectroscopy (EDS) provides qualitative information of metal species in NU-1000. Here, Figure 1.6(a) shows that Nb is deposited uniformly along the NU-1000 crystal.

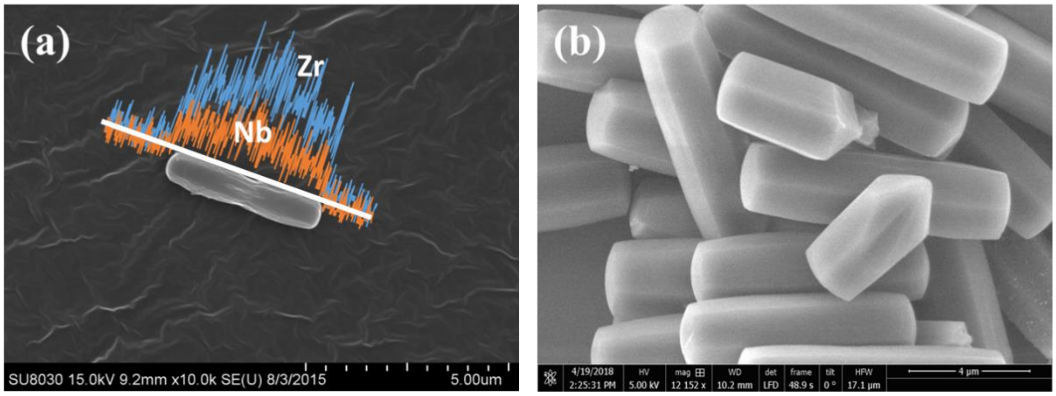

Figure 1.6. SEM images of (a) NU-1000 possessing NU-901 phases in the middle of the crystal along with EDS line scans of Zr and Nb, and (b) phase pure NU-1000.

1.2.6 X-ray absorption spectroscopy

X-ray absorption spectroscopy (XAS) gives element specific information on oxidation state, symmetry, and local coordination environment of metal oxide upon installation in NU-1000. XAS consists of two regimes; the x-ray absorption near edge structure (XANES) and the extended x-ray absorption fine structure (EXAFS). The XANES regime provides information on specific electronic transitions which are sensitive to oxidation state and ligand coordination, whereas the EXAFS regime provides geometric information which is associated with scattering of photoelectrons.

Processing data from the XANES regime provides coordination numbers of deposited metal oxide. Our team has developed a fitting procedure for Nb oxide to correlate coordination numbers and the pre-edge feature.[30] This procedure is slightly modified from previously reported procedures to take into account the weak pre-edge feature of Nb.[31-32] $YNbO_4$ (4-coordinate), $CaNb_2O_6$ (5-coordinate), and $KNbO_3$ (6-coordinate) are used as standards of known coordination numbers. Nb_2O_5 is utilized as a standard of a distorted 6-coordinate sample, as well. Figure 1.7(a) shows representative example of peak fitting exercise for Nb oxide in NU-1000. First, two power laws are fitted through the baseline and the white line regimes. In between the two regimes, a single Gaussian function is fitted to the pre-edge regime. The sum of the power laws and the Gaussian fits is subjected to a least squares regression to fit the data points, and then optimized parameters are used to obtain Gaussian peak heights of standards and catalysts. The peak heights of catalysts are interpolated from a linear regression of known standards to obtain coordination numbers of catalysts. Figure 1.7(b) indicates that NU-1000-supported Nb catalysts (denoted as Nb-AIM and Nb-SIM, here) are undercoordinated, suggesting the presence of Lewis acid sites.

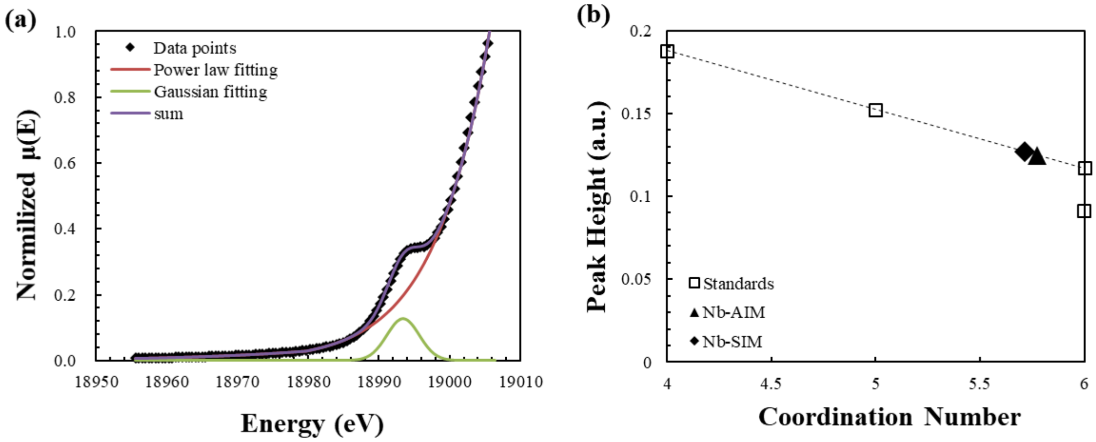

Figure 1.7. (a) Representative Nb K-edge XANES and a fitting of pre-edge feature of Nb-SIM, and (b) linear correlation between Gaussian peak height and coordination numbers.

1.3 Application as heterogeneous catalysts

Herein, applications of NU-1000 as a catalyst support in small hydrocarbon reactions are listed in Table 1.1. Note that examples given here only focus on NU-1000-supported catalysts. Our team recently has been contributing to improved understanding of catalytic applications of NU-1000 as a support. Applications include wide ranges of converting small hydrocarbons over various catalytic species.

Table 1.1. NU-1000 as a catalyst support in small hydrocarbon reactions.

Reaction	**Reactant**	**Catalytic Species**	**References**
Hydrogenation/oligomerization	Ethylene	Ni complexes	33
		Ir complexes	25-26, 34-35
		Ni oxide	28, 36
		Cr oxide	37
		Re oxide	38
		Pt clusters	39
Semi-hydrogenation	Acetylene	Cu nanoparticles	40
	Propyne	Rh-Ga complexes	41
Oxidation	Methane	Cu oxide	42
	Cyclohexene	Nb oxide	43
		Mo oxide	44
	Benzyl alcohol	Co-Al oxide	45
	Anisyl alcohol	V oxide	46-47
Oxidative dehydrogenation	Propane	Co oxide	48-49
		Co oxide at M oxide (Mo, Ti, Al, Zn, Ni)	50
Dehydration	Ethanol	Al oxide	51
	Isopropanol	Si oxide	52
Isomerization/disproportionation	*o*-xylene	W oxide	53
Knoevenagel condensation	Benzaldehyde and Ethyl cyanoacetate	Al oxide, Zn oxide	54

1.4 Objectives and Thesis Outline

The primary goal of this disseration is to understand NU-1000-supported metal oxide catalysts as well-defined analogs to conventional supported catalysts. Achieving this goal can potentially contribute to design strategies of heterogeneous catalysts. This goal will be achieved through the following three objectives:

I. Explore synthesis-structure-activity relationships for Nb-NU-1000 catalysts in the condensed-phase cyclohexene epoxidation.
II. Expand relationships developed in I in the vapor-phase cyclohexene epoxidation.
III. Study synthesis-structure-activity relationships for W-NU-1000 catalysts in *o*-xylene isomerization and disproportionation.

Chapter 2 outlines the work necessary to understand synthesis-structure-activity relationships for H_2O_2 activation in condensed-phase. Nb oxides are deposited in NU-1000 via two post-synthetic methods, and then used as catalysts for a proof-of-concept reaction (cyclohexene epoxidation in condensed-phase). Also, this chapter demonstrates a titration method of counting catalytically relevant sites and its applicability on NU-1000-supported catalysts.

In Chapter 3, the relationships developed in Chapter 2 are explored further by studying the vapor-phase cyclohexene epoxidation with the absence of external solvent. In pursuit of investigating H_2O_2 activation in vapor-phase, we have built a vapor-phase hydrogen peroxide reactor. This chapter presents and compares the behavior of NU-1000- and SiO_2-supported Ti and Nb catalysts with previous studies in condensed-phase.

While Chapters 2 and 3 focus on Lewis acid catalysis, Chapter 4 illustrates another application in solid acid catalysis under relatively aggressive reaction conditions. W oxides are installed in NU-1000 to yield isolated sites and clusters. These catalysts are examined to study their activities for the benchmark strong acid-catalyzed reaction (*o*-xylene isomerization and disproportionation at 250 and 300 °C).

Lastly, Chapter 5 recapitulates the key findings presented in this study. Separately, the Appendix exemplifies the use of metal nodes of MOFs as catalysts for oxidation and oxidative dehydrogenation. To be specific, we study cyclohexene epoxidation in both condensed- and vapor-phases with H_2O_2 over the V node of MIL-47(V). Also, we investigate behavior of the Fe trimer node of MIL-100(Fe) for cyclohexane oxidation with H_2O_2 in the condensed-phase. Lastly, I contribute to understand the catalytic behavior of tri-metallic nodes (Fe_3, Fe_2Mn, Fe_2Co, Fe_2Ni) of M-PCN-250 in gas-phase oxidative dehydrogenation of cyclohexane with N_2O.

Chapter 2. Stable Metal–Organic Framework-Supported Niobium Catalysts

This chapter presents a modified version of the following research article:

Sol Ahn, Nicholas E. Thornburg, Zhanyoung Li, Timothy C. Wang, Leighanne C. Gallington, Karena W. Chapman, Justin M. Notestein, Joseph T. Hupp, and Omar K. Farha, *Inorg. Chem.*, **2016**, 55 (22), 119540-11961.

2.1 Introduction

Heterogeneous catalysts based on metal oxides are of paramount interest for industrial chemical processes.[55-57] In particular, 'single-site' heterogeneous catalysts have received growing attention. In these materials, nearly all sites are considered to participate similarly in the catalytic reaction, making it easier to understand the kinetics and mechanism of the catalysis from both experimental and computational perspectives.[58] Strategies to achieve these structurally well-defined catalyst sites include grafting metal-organic complexes,[59] atomic layer deposition (ALD),[60] and templated techniques.[61-62]

Catalyst supports have been demonstrated to play a significant role in the activity and stability of single-site catalysts and in supported oxides in general.[63] Metal–organic frameworks (MOFs), a class of porous materials comprised of metal nodes and organic linkers, are structurally well-defined and have found potential applications in, but not limited to, gas storage and release[6-9] and separation,[10] sensing[11] and catalysis.[12-14] Due to their high surface areas, MOFs have been considered as promising candidates as catalytic supports. Furthermore, Zr- and Hf-based MOFs exhibit relatively high chemical,[15-17] thermal,[18-19] and mechanical stability[19-20] that is attributable to the oxophilic nature of the Zr_6/Hf_6 clusters and Coulombic attraction, manifested as strong ionic bonding, between these cationic metal nodes and anionic organic linkers.

Among the various reported Zr-MOFs, NU-1000 is a suitable candidate for such application due to its high chemical and thermal stability.[21] In addition, it is readily modifiable post-synthetically[23-25] and provides grafting sites for deposited metals[26] as hydroxyl and/or aqua groups are present on Zr_6 nodes (see Figure 2.1).[27] Moreover, the lengthy organic linkers provide spacing between adjacent nodes (> 1 nm), which eliminates surface diffusion as a mechanism for aggregation of the active metal ions during deposition, post-synthetic treatment, and catalysis.[28] Two post-synthetic methods have been reported for the metalation of these Zr_6 nodes in NU-1000: (1) vapor-phase ALD in a MOF (AIM) using organometallic or coordination complexes as the metal precursors,[28, 54, 64-65] and (2) solution-phase grafting in a MOF (SIM) using organometallic precursors and anhydrous organic solvents.[66]

Separately, we and others have reported that supported niobium oxide materials are effective catalysts in selective oxidation.[30, 67-76] Highly dispersed Nb(V) oxide supported on silica can act as a strong Lewis acid catalyst and is demonstrated to be more active for alkene epoxidation using hydrogen peroxide as an oxidant than the benchmark Lewis acid catalyst, titanium oxide on silica.[30, 77-79] In this reaction, the epoxidation with aqueous hydrogen peroxide is well known for its sustainability since water is the only byproduct from this oxidant.[80] Recently, some of us have demonstrated the importance of bulky precursors for achieving a preponderance of under-coordinated and highly active Nb(V)-silica sites for alkene epoxidation with H_2O_2.[81]

In this study, we synthesize highly active and isolated metal oxide catalysts consisting of NbOx on NU-1000. Nb(V) oxides were supported onto NU-1000 via both AIM and SIM methods, and we compare their physicochemical properties via powder x-ray diffraction (PXRD), inductively coupled plasma atomic emission spectroscopy (ICP-AES), nitrogen adsorption isotherms, and difference envelope density (DED) measurements. Additionally, we examined their active site by titration with phenylphosphonic acid during cyclooctene epoxidation. Finally, we evaluated their reactivity and selectivity as heterogeneous catalysts for the epoxidation of cyclohexene at 65 °C with H_2O_2 as an oxidant.

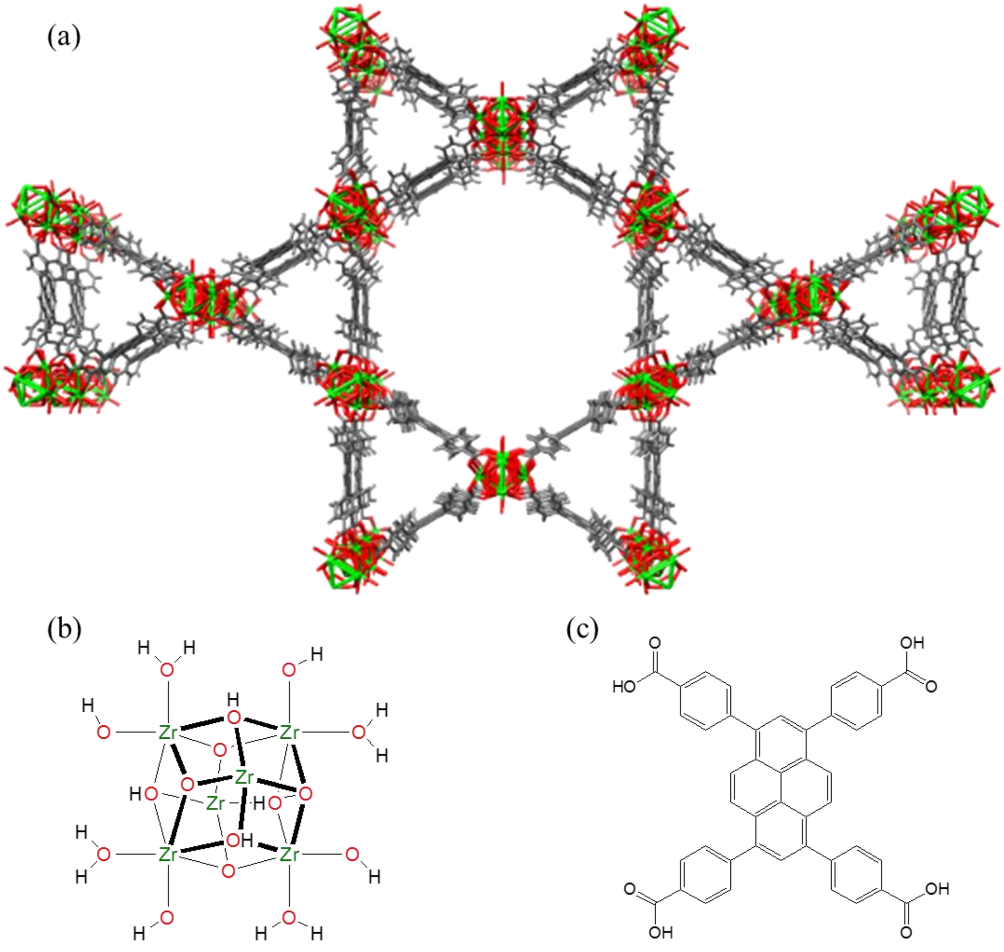

Figure 2.1. Structure of NU-1000: (a) packing along the c axis; (b) Zr_6 node ($[Zr_6(\mu_3\text{-}O)_4(\mu_3\text{-}OH)_4(OH)_4(H_2O)_4]^{8+}$); (c) organic linker ($TBAPy^{4-}$).

2.2 Experimental Methods

2.2.1 Synthesis of Catalysts

The catalytic support, NU-1000 (nominally 5 µm length crystallites), was synthesized and activated following a modified procedure in the literature.[22] Smaller NU-1000 crystallites (2.5 µm length) were synthesized by controlling both node-to-linker ratio and reaction time, according to a literature protocol previously established by our team.[82]

(*tert*-Butylimido)tris(diethylamido)niobium(V) (98 %) was used as-received from Strem Chemicals as the niobium precursor for both ALD and condensed phase grafting. For the synthesis of Nb(V) ALD in MOF (Nb-AIM), NU-1000 (10 mg, 4.67 µmol Zr_6 nodes) was loaded in an ALD sample holder. The sample was placed in a Cambridge Nanotech Savannah 100 ALD reactor and the sample was dried of physisorbed water under 15 sccm N_2 flow for 20 min at 125 °C and this temperature was maintained during the deposition process. The niobium precursor was heated up to 110 °C, and then pulsed for 1 sec repeatedly for 400 half-cycles to ensure the saturated metalation of Zr_6 node in NU-1000. Each half-cycle comprised of a quasi-static exposure of the precursor in which the reactor was isolated from rough pumping for 90 sec followed by a 90 sec purge under 2 sccm high-purity N_2. H_2O was used as the second reactant at room temperature; it was pulsed for 0.02 sec repeatedly for 25 half-cycles to remove the ligands from the grafted Nb(V) precursor. Likewise, each half cycle consisted of isolating the reactor from rough pumping for 120 sec followed by a 120 sec purge under the same flow rate of N_2. For Nb(V) on commercial zirconia (Nb-ZrO_2), commercial zirconia (99 % trace metals basis, Sigma Aldrich) was used as the substrate instead of NU-1000 under the same ALD condition.

For condensed phase grafting (Nb-SIM), NU-1000 (50 mg, 23.3 µmol Zr_6 nodes) was introduced to a solution containing the Nb(V) precursor (35 μL, 93.2 μmol) dissolved in 3 mL heptane (99 %, anhydrous, Sigma Aldrich) in an Ar-filled glove box. The reaction was allowed to take place over 24 h period with occasional agitation of the solution. The mixture was decanted, and then washed 3 times with 3 mL of heptane. At this point, the material was removed from the glove box, and subsequently washed in air 3 times with 5 mL of acetone.[66] For comparison Nb-SiO_2 was synthesized by grafting at a loading of 0.27 mmol/g following a procedure previously established by some of us.[30]

2.2.2 Characterization of Catalysts

Powder X-ray diffraction (PXRD) was used to verify the integrity of the structure of the materials using a Rigaku SmartLab diffractometer with a Cu-Kα radiation source (45 kV, 160 mA tube voltage and current). Diffraction patterns were measured over the 2θ range of 2–15° with a 0.05° step width and a 5°/min scan speed.

Niobium (309.418, 316.340, 319.498, and 322.548 nm) and zirconium (327.305, 339.198, 343.832, and 349.621 nm) contents were measured using inductively coupled plasma atomic emission spectroscopy (ICP-AES, iCAP 7600, Thermo Scientific), which are compared to the ICP standard solutions. NU-1000-supported Nb(V) catalysts (*ca.* 1 mg) were dissolved in 0.75 mL sulfuric acid (ACS reagent, 95-98 %, Sigma Aldrich) and 0.25 mL of 30 wt.% H_2O_2 (aqueous, Sigma Aldrich) mixture, followed by microwave digestion using Initiator+ (Biotage) at 150 °C for 5 min. Nb-ZrO_2 were fused in a lithium metaborate and a lithium tetraborate mixture, and then Zr and Nb contents were measured by ICP-OES (Galbraith Laboratories, Inc., 2323 Sycamore Dr., Knoxville, TN 37921).

Nitrogen adsorption isotherms were measured at 77 K using a Micromeritics Tristar II instrument, and DFT pore size distributions were obtained from the desorption branch of the resulting isotherms. Prior to analysis, samples were pre-treated under dynamic vacuum at 120 °C for 18 h using a Micromeritics Smart VacPrep.

2.2.3 Difference Envelope Density Measurement

Powder X-ray diffraction patterns were collected at ambient temperature at beamline 17-BM-B at the Advanced Photon Source. 17.04 keV (0.72768 Å) x-rays were used with an amorphous silicon area detector, allowing for rapid acquisition of data. Powdered samples were loaded into polyimide capillaries, which were placed into a sample changer cassette. Patterns were collected at a nominal distance of 1 m. Calibration of detector to sample distance, beam center, detector tilt, rotation and reduction of the acquired data were performed using GSAS-II.[83]

Le Bail whole pattern fitting was utilized to extract lattice parameters and peak intensities from powder diffraction data.[84] The previously reported P6/mmm crystal structure for NU-1000 was used as a starting point for these analyses.[54] Lattice and pseudo-Voigt parameters were refined using a 2θ range of 1–5°. Structure envelopes (SEs) were generated from the extracted peak intensities from powder diffraction data.[85] SEs of NU-1000 were subtracted from those of both Nb-AIM and Nb-SIM to generate difference envelope densities (DED)[86] to estimate the distribution of electron density associated with deposited Nb(V).

2.2.4 Active Site Titration and Cyclohexene Epoxidation

An aqueous solution of 50 mM of phenylphosphonic acid (PPA, Sigma Aldrich) was used as a titrant to probe Lewis acid sites at 65 °C.[87] MOF-supported catalysts (4 mg, 5.5 μmol based on Nb(V) content), *cis*-cycoloctene (550 μmol, 75 μL, 95 %, Sigma Aldrich), 1,2-dichlorobenzene (internal standard, 1.3 mmol, 60 μL, 98 %, Alfa Aesar), and acetonitrile (reaction solvent, 4.5 mL, > 99 %, spectrophotometric grade, Alfa Aesar) were mixed in 20 mL septum capped glass vial. This vial was shaken on a Glas Col heated vortexer at 700 rpm, for each titration. Discrete amounts of PPA were added from 0 to 1.5 equivalents (0, 0.25, 0.50, 0.75, 1.0, and 1.5) of PPA relative to total Nb(V) as determined by ICP-AES. After one hour of equilibration at 65 °C, aqueous H_2O_2 (1.65 mmol, 100 μL, 50 wt%, Sigma Aldrich) was added to initiate the titration. The initial rate of each titration was calculated from the epoxide concentration vs. time data over the first 15 minutes of reaction.

In a typical cyclohexene epoxidation catalytic reaction, cyclohexene (11 mmol, 1.1 mL, > 99%, Sigma Aldrich), and 1,2-dichlorobenzene (1.3 mmol, 150 μL), were dissolved in acetonitrile (9 mL), to which Nb-AIM or Nb-SIM (8 mg, 11 μmol based on Nb(V) content) were added. After one hour of mixing, 4.0 M H_2O_2 in a acetonitrile solution (1.1 mmol, 270 μL) was added to initiate the reaction. This low-water H_2O_2 solution was prepared by diluting aqueous H_2O_2 (10 mL, 30 wt%) in acetonitrile (20 mL), followed by drying over anhydrous $MgSO_4$ (7g, > 99%, Sigma Aldrich), which was then centrifuged and decanted.[81] The amount of Nb-AIM and Nb-SIM was adjusted to the following molar ratio, cyclohexene : H_2O_2 : Nb(V) = 1000 : 100 : 1.

Aliquots (0.1 mL) from both titration and epoxidation were collected into GC sampling vials with silver powder (*ca.* 0.5 mg, > 99 %, Sigma Aldrich) to quench excess H_2O_2 to prevent oxidation during GC analysis.[30] Products were identified using GC-MS (Shimadzu QP2010 CG/MS, Zebron ZB 624 capillary column) and quantified using GC-FID (Shimadzu QP2010 GC-

FID, TR-1 capillary column). For all reactions, mass balances calculated from GC-FID peak areas were ≥ 90 %.

2.3 Results and Discussion

2.3.1 Synthesis and Characterization

Table 1 summarizes the Nb(V) loadings of the different catalysts examined in this study. The Nb(V) content in Nb-AIM can be controlled by the number of precursor pulses in ALD process. In this study, we found that 400 pulses gave 4 Nb(V) per Zr_6 node and that the crystallinity of the NU-1000 was maintained (Figure 2.2). Higher numbers of pulses increased the Nb(V) loading, but excessively degraded the MOF crystallinity and were not studied further. SIM occurred with quantitative grafting of the Nb(V) precursor, and Nb-SIM was synthesized to match the Nb(V) loading of Nb-AIM. No change in the crystallinity of the NU-1000 support was observed in the synthesis of Nb-SIM as well as after cyclohexene epoxidation reaction with Nb-SIM (Figure 2.2).

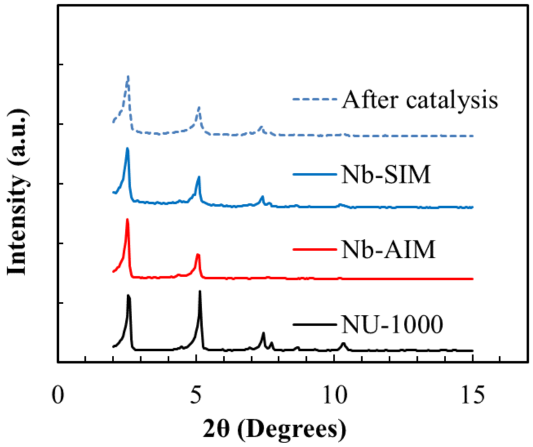

Figure 2.2. PXRD patterns of NU-1000, Nb-AIM, Nb-SIM as synthesized and after cyclohexene epoxidation

Finally, Nb-ZrO_2 was synthesized under the same ALD conditions (number of pulses) as Nb-AIM, and it gave a similar Nb(V) surface density when expressed as Nb(V) per surface Zr atoms. Although surface densities are typically given per BET surface area, this value is not particularly meaningful for MOF-supported catalysts, since much of the surface area originates from the linkers, rather than the nodes onto which the precursors graft. The Nb(V) content in MOF-supported catalysts is approximately an order of magnitude higher than that on zirconia (Table 2.1) as expected since commercial zirconia has a significantly lower density of grafting sites when compared to NU-1000.

Table 2.1. Summary of catalysts.

Catalyst	**MOF crystal size**[a] **[µm]**	**Nb per Zr_6 node**[b] **[-]**	**Nb content**[b] **[mmol/g]**	**Nb surface density [Nb/Zr_{surf}]**
ZrO_2	-	-	-	-
NU-1000	5	-	-	-
Nb-ZrO_2	-	-	0.19	0.30[c]
Nb-SIM	5	3.7	1.41	0.62[d]
Nb-SIM(H)[e]	2.5	3.6	1.35	0.58[d]
Nb-AIM	5	4.4	1.62	0.73[d]
Nb-AIM(H)[e]	2.5	4	1.50	0.67[d]

[a] From SEM, controlled by synthesis conditions
[b] From ICP-AES
[c] Using Zr surface density of zirconia is 7.34 Zr/nm^2 [88-89]
[d] Assuming every Zr is presented on the surface
[e] H: half crystal size (2.5 µm length) of MOF

Nitrogen isotherms (Figure 2.3(a)) show that the surface areas of both Nb-SIM (1,470 m^2/g) and Nb-AIM (470 m^2/g) decrease compared to the parent NU-1000 (2,180 m^2/g); the loss of surface area is consistent with our previous studies.[54] Interestingly, a reduction in the mesopore size of Nb-SIM is observed in Figure 2.3(b), as opposed to no apparent change in the mesopore size with Nb-AIM. Combined with the differences in surface area, this gives a preliminary indication that the two synthetic methods may result in different local structures of the Nb(V) ions on the NU-1000 node or within the crystallite.

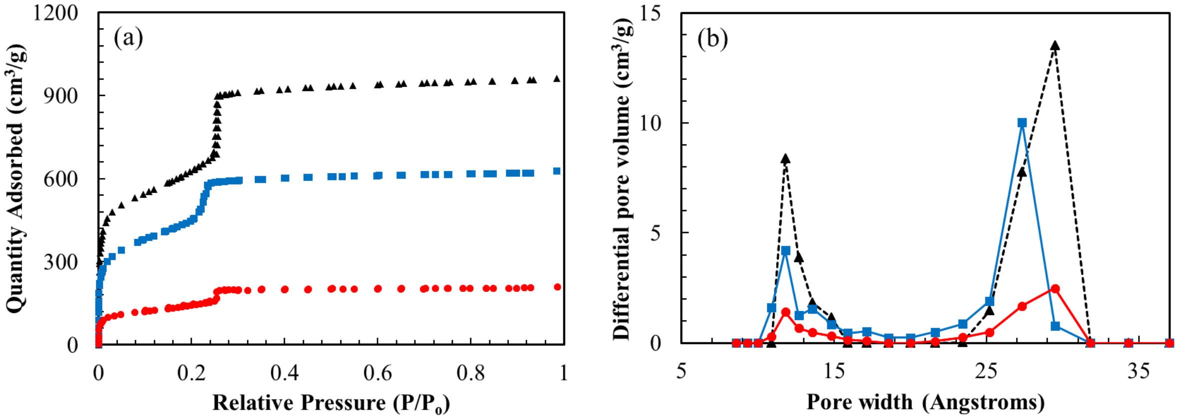

Figure 2.3. (a) N_2 isotherms and (b) DFT pore size distributions for NU-1000 (black triangles), Nb-SIM (blue squares), and Nb-AIM (red circles)

To elucidate the structural changes of Nb-SIM and Nb-AIM as compared to the parent MOF, NU-1000, we utilized a technique called difference envelope density (DED). By subtracting the electron density contribution from the parent material, NU-1000, we can clearly see that there are deposited Nb(V) atoms in Nb-AIM uniformly distributed in the lateral cavities between the two adjacent Zr_6 nodes along the c-axis (Figure 2.4 (a) and (b)). Detailed study of this preferential binding of the Nb(V) ions to the small aperture of NU-1000 is still in progress and will be reported on in the near future. In contrast, solution-phase grafting results in deposition in the same cavities, but with a bilobal distribution of electron density, which may suggest formation of Nb oxide dimers (Figure 2.4 (c) and (d)).[90]

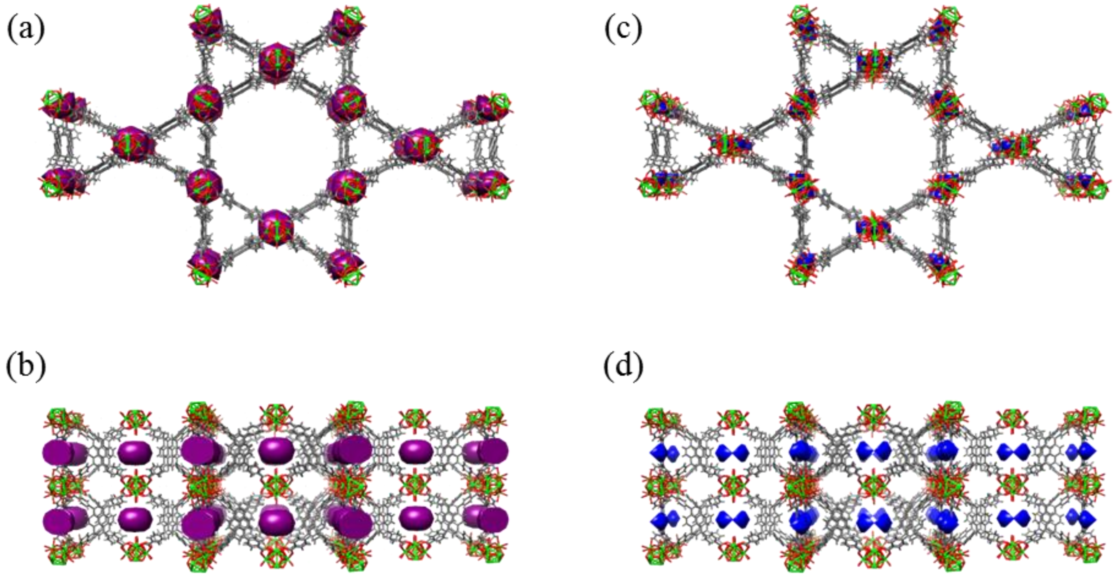

Figure 2.4. Difference envelope densities (DED) map of Nb-AIM (a) view along the c axis, (b) a axis and Nb-SIM (c) view along the c axis and (d) a axis.

2.3.2 Catalysis

Titration with phenylphosphonic acid (PPA) during cyclooctene epoxidation reaction has been used to quantify the number of Lewis acid sites in silica-supported Group IV and V metal oxide catalysts.[87, 91] Since cyclooctene assesses the total reactivity and is highly selective to a single epoxide product, this is a good model system for the liquid-phase *in situ* titration. Here, we employ this technique to count the number of the active Lewis acidic sites in the MOF-supported materials. It is important to note that the titration analysis is restricted to PPA/Nb(V) < 0.75 because PPA displaces the pyrene linker at high concentrations,[92] as evidenced, in part, in the loss of MOF crystallinity (Figure 2.5).

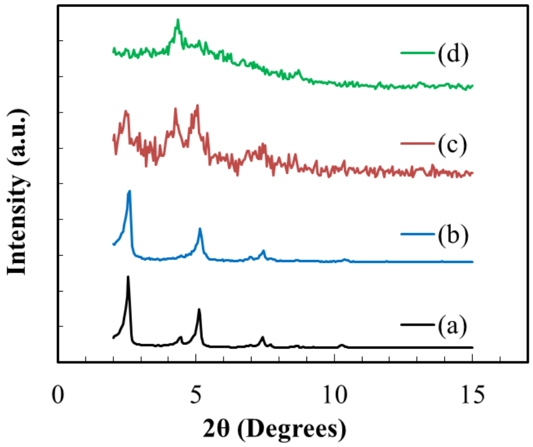

Figure 2.5. PXRD patterns of Nb-SIM after PPA titration with ratio of PPA-to-Nb(V) (a) 0.25, (b) 0.5 (c) 0.75, and (d) 1

However, the data points at sub-stoichiometric PPA-to-Nb(V) concentrations exhibit a linear relationship (Figure 2.6) between the amount of titrant added and the initial rate of cyclooctene epoxidation (*vide infra*). Extrapolating the rate decrease to the baseline gives a maximum of 1.8 mmol/g active sites in Nb-AIM (111 % of the number of Nb(V) atoms) and 1.4 mmol/g active sites in Nb-SIM (99 % of the number of Nb atoms). Bare NU-1000 also possesses mild activity due to the Brønsted acidity of the zirconium oxide nodes;[93] subtracting this contribution gives an active site count of 1.5 mmol/g (93 %) and 1.3 mmol/g (93 %) for Nb-AIM and Nb-SIM, respectively. Under the reasonable assumptions of 1:1 titrant-to-active site ratio and the preferential titration of strong Nb(V) Lewis acid sites over weaker Zr Lewis acid sites, this close agreement between the number of active sites titrated using PPA and the Nb(V) content from ICP suggests that nearly all Nb(V) atoms act as reactive sites. This contrasts with more typical oxide-supported Nb(V), where less than 65 % was kinetically relevant, even in the best cases.[81] However, even though the catalysts have approximately the same amount of kinetically relevant Nb(V), apparent rates are different. The mode of synthesis clearly is a significant factor in controlling activity. For these well-defined catalysts, the salient difference with regard to Nb(V) activity presumably is the mode of arrangement of the catalytic atoms. In the SIM case, Nb(V) may exist as isolated oxide pairs on each node, while Nb(V) appears to exist as slightly larger oxide clusters in Nb-AIM.

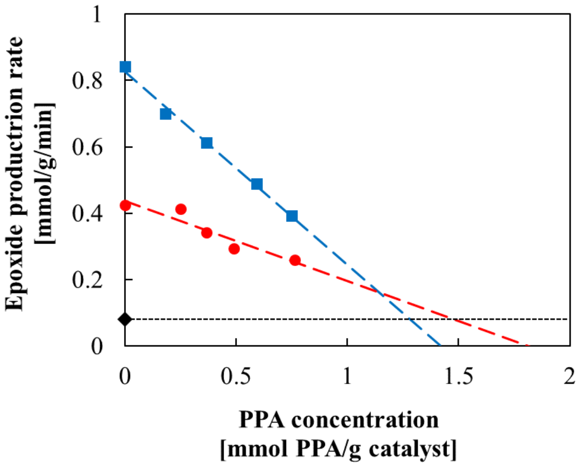

Figure 2.6. PPA titration of NU-1000 (black diamond), Nb-SIM (blue squares), and Nb-AIM (red circles). Extrapolation of the linear fits to the black dotted line (contribution from the support) or to zero activity gives the range of kinetically relevant active sites.

Motivated to further understand the reactivity differences in the poisoning experiments for cyclooctene epoxidation, we then examine cyclohexene epoxidation to study trends in selectivity.

Selectivity in cyclohexene oxidation is assessed as a pathway selectivity for how each catalyst activates H_2O_2; conventional product selectivity is given in Table 2.2.

Scheme 2.1 describes the proposed reaction network with competing radical and non-radical oxidation pathways.[94-96] Pathway selectivity is calculated from Eq. (2.1):

$$\text{Pathway selectivity} = (\text{mol}_{\text{epoxide}} + \text{mol}_{\text{diol}} - (\text{mol}_{\text{enol}} - \text{mol}_{\text{enone}})) / \text{mol}_{\text{all } C_6 \text{ products}} \times 100\% \quad (2.1)$$

which combines epoxide and its hydrolysis product cyclohexanediol, and subtracts cyclohexenol to account for epoxidation via cyclohexenyl hydroperoxide. It should be noted that epoxide hydrolysis tends to increase with conversion for all catalysts (Table 2.2) due to the simultaneous formation of H_2O from H_2O_2 utilization;[97] this does not impact the pathway selectivity. Figure 2.7 shows a representative concentration time-course plot (plots for other catalysts are shown in Figure 2.8) for this reaction and a fit to a first-order rate law. All of these catalysts run without apparent deactivation as confirmed by fitting to a first-order rate law (Figure 2.9).

Table 2.2. Summary of products selectivity.

Catalyst	**Selectivity at ~25 % yield [%]**				**Selectivity at 5 h [%]**			
	Epoxide	**Diol**	**Enol**	**Enone**	**Epoxide**	**Diol**	**Enol**	**Enone**
ZrO_2	6	11	59	24	5	11	58	26
NU-1000	-	-	-	-	55	29	12	4
Nb-ZrO_2	28	7	45	20	43	13	27	17
Nb-SIM	61	23	12	4	38	43	14	5
Nb-SIM(H)	35	20	27	18	31	34	21	14
Nb-AIM	46	36	14	4	31	58	8	3
Nb-AIM(H)	51	14	23	12	32	37	18	13
Nb-SiO_2	83	12	4	1	67	28	4	1

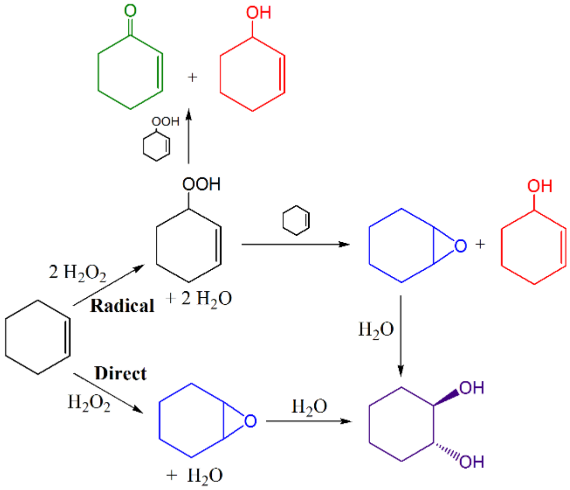

Scheme 2.1. Proposed reaction network for cyclohexene oxidation.

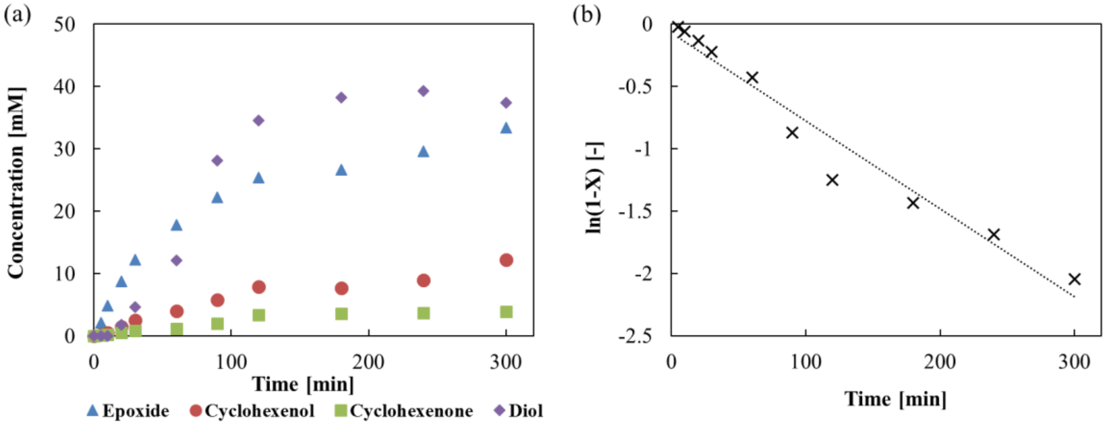

Figure 2.7. (a) Representative product yields vs. time for cyclohexene epoxidation at 65 °C with Nb-SIM and (b) a fit to a first-order rate law with no evidence of deactivation in the rate of cyclohexene consumption.

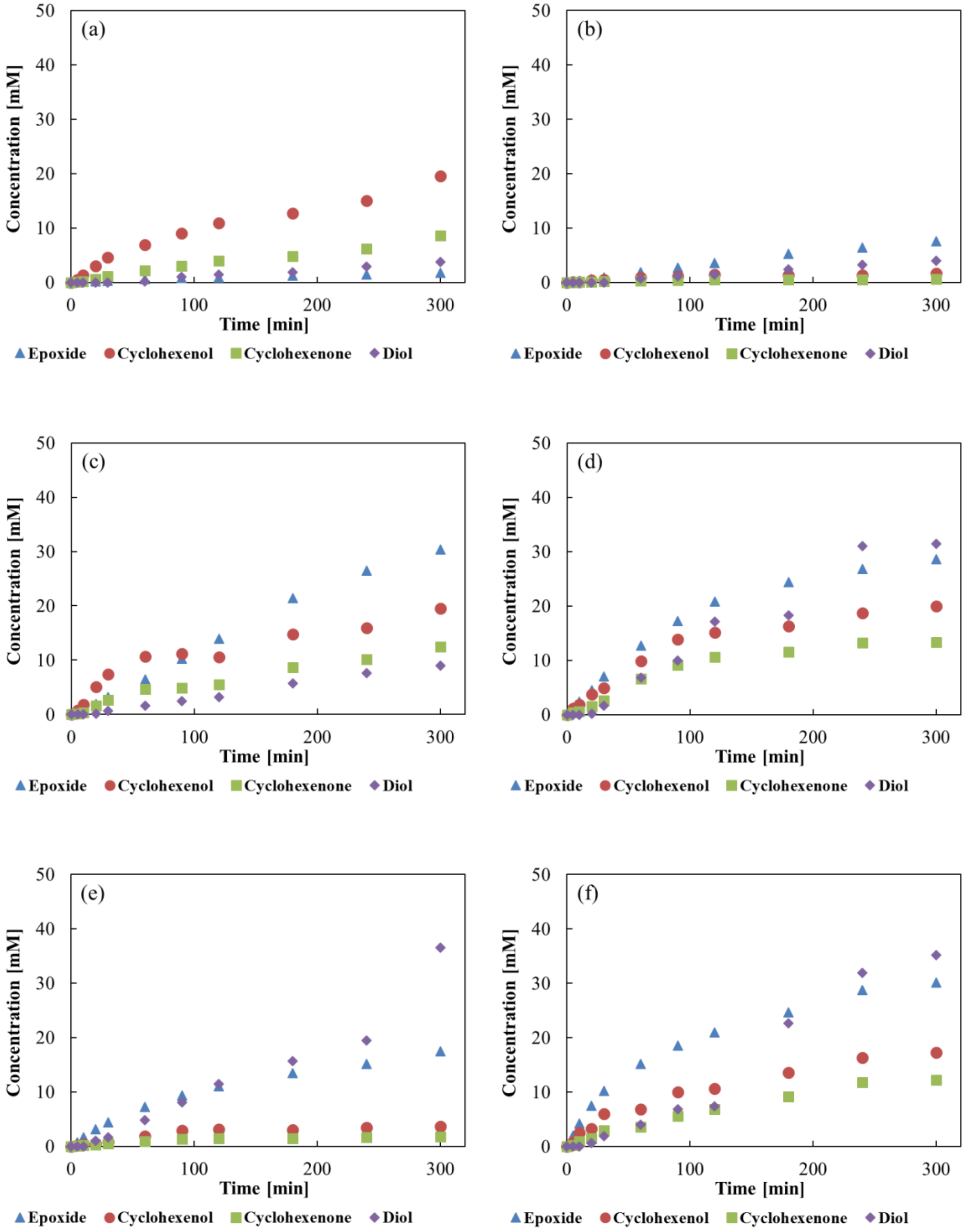

Figure 2.8. Product yields vs. time for cyclohexene epoxidation at 65 °C with (a) ZrO_2, (b) NU-1000, (c) Nb-ZrO_2, (d) Nb-SIM(H), (e) Nb-AIM, and (f) Nb-AIM(H)

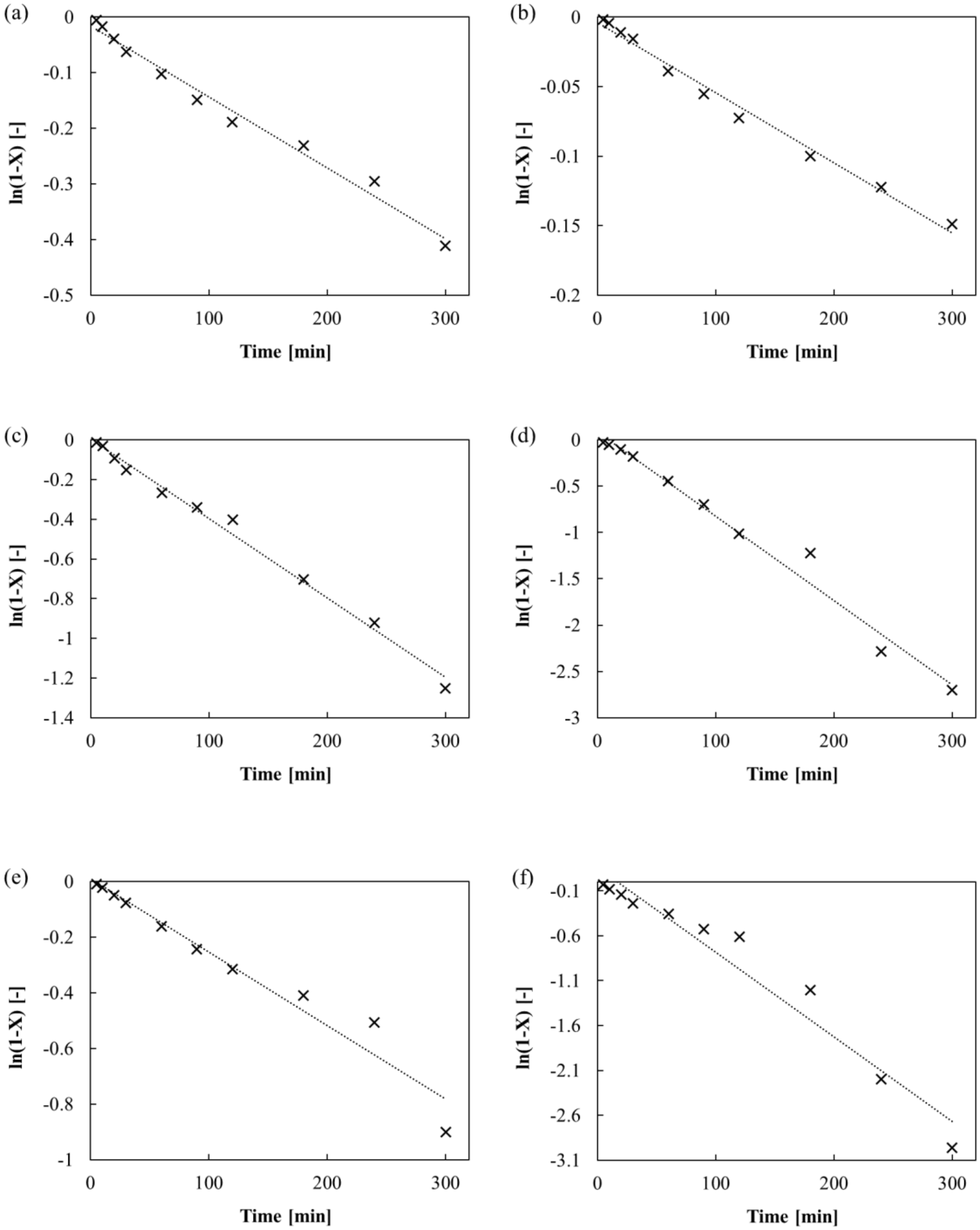

Figure 2.9. First to a first-order rate law for cyclohexene epoxidation at 65 °C with (a) ZrO_2, (b) NU-1000, (c) Nb-ZrO_2, (d) Nb-SIM(H), (e) Nb-AIM, and (f) Nb-AIM(H)

The reactivity data for the cyclohexene epoxidation of the MOF-supported Nb(V) catalysts and control materials are summarized in Table 2.3. Unmodified ZrO_2 (entry 1) and NU-1000 (entry 3) both give low initial rates and 5-h yields. Unmodified ZrO_2 gives exclusively oxidation products that arise from radical decomposition of H_2O_2, whereas bare NU-1000 is selective to direct cyclohexene oxidation, albeit with low yields.

Nb-ZrO_2 (entry 2) engenders a much higher yield than ZrO_2 and ultimately reaches ~ 45% pathway selectivity, indicating that the Nb(V) sites are responsible for the direct cyclohexene epoxidation observed. All of the 5-μm MOF catalysts (entries 3, 4, and 6) show high pathway selectivity, while the pathway selectivity decreases somewhat for the smaller crystallites (entries 5 and 7). Combined, these results suggest that the radical pathway oxidation products arise from an initial burst of H_2O_2 decomposition that occurs on crystallite external surfaces at the beginning of the reaction; proper catalyst preconditioning may mitigate this effect.

The oxide-supported catalyst Nb-ZrO_2 and the benchmark Nb-SiO_2 both display high initial TOFs, but all of the MOF-supported catalysts are faster on a per-g basis due to their high Nb(V) loadings. The rates and yields of the MOF-supported catalysts are both increased significantly by decreasing the MOF crystallite size (entries 5 and 7), and both Nb-SIM(H) and Nb-AIM(H) have oxygenate yields exceeding that of the benchmark Nb-SiO_2 catalyst. Decreasing the crystallite size had a particularly positive effect on Nb-AIM, consistent with the even distribution of Nb(V) throughout the pseudo-1D pores of the material, as inferred from the DED analysis (Figure 4a and 4b) discussed above. This analysis also indicates that further improvements in TOF may be possible, potentially approaching that of the oxide-supported materials, if further size-reduced support can be successfully utilized.

Table 2.3. Summary of kinetic data.

Entry	Catalyst[a]	Initial rate[b] $[\mathrm{mol\ mg_{catalyst}^{-1}\ min^{-1}}]$		Initial TOF[c] $[\mathrm{mol\ mol_{Nb}^{-1}\ min^{-1}}]$		5 h	
		Total	Direct[d]	Total	Direct[d]	Total Yield[e] [%]	Direct Pathway Selectivity [d] [%]
1	ZrO_2	0.14	0	n/a	n/a	34	0
2	Nb-ZrO_2	0.47	0	2.53	0	71	45
3	NU-1000	0.06	0.02	n/a	n/a	14	76
4	Nb-SIM	0.8	0.61	0.57	0.43	87	72
5	Nb-SIM(H)	0.92	0.31	0.68	0.23	93	57
6	Nb-AIM	0.52	0.40	0.32	0.25	59	88
7	Nb-AIM(H)	1.43	0.63	0.95	0.42	95	64
8	Nb-SiO_2	0.51	0.47	1.89	1.75	75	93

[a] Cyclohexene epoxidation at 65 °C with molar ratio of $C_6 : H_2O_2 : \mathrm{Nb(V)} = 1000 : 100 : 1$

[b] Product formation on a catalyst weight basis.

[c] Product formation on a total number of Nb(V) moles basis.

[d] Relative rate contribution to direct (non-radical) pathways.[94-96]

[e] Yield = $(\mathrm{mM_{all\ C_6\ products}})/(103\ \mathrm{mM_{H_2O_2,0}}) \times 100\%$. Limited by H_2O_2.

2.4 Conclusions

NU-1000-supported Nb(V) catalysts were synthesized with high Nb(V) content (up to 1.6 mmol/g) *via* two different approaches, namely AIM and SIM. One of the obvious advantages of the MOF-supported catalysts is that Nb(V) loadings (per g) can be much higher than for conventional oxide-supported catalysts, such as Nb-ZrO_2 or Nb-SiO_2, while still maintaining high TOF per Nb(V) atom. The MOF crystallinity and high porosity were preserved after Nb(V) deposition, as confirmed by PXRD and nitrogen isotherms, respectively. Of particular interest, DED map studies indicate that Nb(V) ions are regularly distributed through the framework with a preference for deposition on the c-axis in both AIM and SIM cases, but that the *local* structure of the Nb(V) ions depends on whether AIM or SIM was used for the deposition. PPA titrations were also used for the first time to quantify the amount of active grafted oxide sites in a MOF-based material, and the result suggests that all Nb(V) sites, within uncertainty, are active for the electrophilic oxidation. This contrasts with more typical oxide-supported Nb(V), where less than 65% was kinetically relevant, even in the best cases.[81] Cyclohexene epoxidation reaction was examined, and MOF-supported catalysts are more selective and, due to the much higher Nb(V) loadings, much more active than the chemically similar Nb-ZrO_2 on a per-gram basis. Finally, the apparent rate of the Nb-AIM catalyst increased by nearly 3-fold when the support particle size was reduced, indicating significant rate limitations due to reactant diffusion within individual particles. This observation is consistent with the observed uniform distribution of Nb(V) sites along pseudo-1D pores of this material. This result suggests that by using nano-sized NU-1000, Nb-AIM catalysts displaying turnover frequencies approaching those of the oxide-supported catalysts, but with rates per gram nearly an order of magnitude higher, could potentially be realized. Further studies are currently in progress involving this and other catalyst modifications, as well as additional detailed characterization to elucidate structure/activity relationships.

Chapter 3. Determining the Critical Role of Solvation in Supported Ti and Nb Epoxidation Catalysts via Vapor-phase Kinetics

This chapter presents a modified version of the following manuscript:

Sol Ahn, Scott L. Nauert, Kenton E. Hicks, M. Alexander Ardagh, Neil M. Schweitzer, Omar K. Farha, and Justin M. Notestein, *Manuscript in Preparation*, **2019**.

3.1 Introduction

Hydrogen peroxide (H_2O_2) is considered to be an attractive oxidant because its reaction byproducts are water and oxygen as well as oxygen atom efficiency is higher than organic peroxides.[98] H_2O_2 plays an important role as a terminal oxidant of innumerable oxidation reactions such as alkene epoxidation, alcohol oxidation, sulfoxidation, and so on.[99] Alkene epoxidation is of particular interest as epoxides serve as building blocks of resins and fine chemicals.[100] Among them, epoxidation of cyclohexene provides a lot of information about the mechanism of H_2O_2 activation because the reaction products are indicative of the reaction pathway which directly leads to understand direct/radical activation of H_2O_2.[94-95, 101]

Most of previous studies, however, have focused on the condensed phase reactions when using aqueous H_2O_2 or organic peroxide despite following limitations. First and foremost, reaction solvents can affect reactivity and/or selectivity significantly due to competitive adsorption between solvents and reactants, effect of solvent acidity, solubility of reactants and products, and so on.[102-104] Second, active site such as V ions often can leach into reaction solvent. On the other hand, UiO-66-supported V catalyst showed a good time-on-stream stability under gas-phase oxidative dehydrogenation of cyclohexene without a metal ion leaching.[105] Although we can circumvent aforementioned limitations, practical issues restrict selective oxidation with H_2O_2 under flow conditions. These issues arise from a competition between vaporization and decomposition at elevated temperature. To the best of our knowledge, there are only two reported examples of heterolytic activation of H_2O_2 in flow reactors.[106-107] Herein, motivated further from previous two studies, we present a new vapor-phase peroxide reactor which is robust and improved for the purpose of studying H_2O_2 activation in the vapor-phase. With this reactor, we compare the kinetic behavior of vapor-phase cyclohexene epoxidation over Ti and Nb grafted on a conventional support (SiO_2) and on an unconventional support (Zr based metal–organic framework, NU-1000). Furthermore, we compare kinetics and thermodynamics of the vapor-phase cyclohexene epoxidation with high fidelity kinetics of alkene epoxidation collected previously in the condensed phase.[108-110]

3.2 Experimental Methods

3.2.1 Synthesis of Catalysts

For the synthesis of M-SiO_2, 5 g of Selecto SiO_2 (Fisher Chemical, 6 nm pore size, 550 m^2/g, 63-200 μm particle size) was dried for 30 min at 120 °C in a glass oven. Then, the SiO_2 was added to an oven dried 250 mL round bottom flask along with 50 mL of freshly distilled anhydrous toluene (Sigma-Aldrich, ACS Reagent, > 99.5%) and stirred at 200 rpm with an oven dried teflon stir bar at ambient temperature. Metal precursors, 227 mg of titanocene dichloride ($Cp_2Ti(IV)Cl_2$, Strem Chemicals, > 99%) and 269 mg of niobocene dichloride ($Cp_2Nb(IV)Cl_2$, Strem Chemicals, > 99%), were added to the mixture with the intent to be highly dispersed (0.2 Metal/nm^2) for Ti-SiO_2 and Nb-SiO_2, respectively. Then, the mixtures were allowed to stir for 1 hr at ambient temperature. Then, the mixtures were filtered using a vacuum filter, washed with 200 mL of toluene and hexanes (Fisher Chemical, Certified ACS, > 98.5%), and dried in air for 5 min. The as-made Cp_2Ti-SiO_2 and Cp_2Nb-SiO_2 were loaded into the muffle furnace and calcined at 550 °C for 6 hours with a 10 °C/min ramp rate to yield Ti-SiO_2 and Nb-SiO_2, respectively.

The catalyst support, NU-1000, was prepared and activated following the method that is previously established by our team.[22] For the synthesis of M-NU-1000, 200 mg of NU-1000 (185.1 μmol of Zr_6 node) and 449.3 μL of titanium(IV) isopropoxide (Sterm, min. 98%) and 555.1 μL of (with the intent to add 8 Metal equivalent to one Zr_6 node) of (tert-butylimido) tris(diethyl-amino)niobium(V) (Strem, min. 98%) were mixed in 10 mL heptane (Sigma Aldrich, 99 %, anhydrous) for Ti-NU-1000 and Nb-NU-1000, respectively. These reaction mixtures were in a glove box for overnight with occasional swirling. The mixtures were decanted, and then added 10 mL of fresh heptane (one heptane washing cycle). The heptane washing cycle was repeated for four times to remove unreacted metal precursors. After this heptane washing steps, the materials were transferred out from the glove box, and then acetone washing step was repeated for four times. Remaining ligands from the Ti and Nb precursors were removed to yield TiO_x and NbO_x on the nodes of NU-1000 via hydrogen transfer in the moist air.

3.2.2 Characterization of Catalysts

M-SiO_2 catalysts (ca. 2 mg) were digested in a mixture of 1 mL of hydrofluoric acid (Macron, 48 wt.%) [CAUTION: handle HF with extreme care] and 9 mL of nitric acid (Fisher Chemicals, 67-70 % w/w, trace metal grade) with mixing on a shaker plate. M-NU-1000 catalysts (ca. 2 mg) were digested in 2 mL of nitric acid with the aid of microwave using Initiator+ (Biotage) at 150 °C for 15 min. Titanium (323.452, 334.941, 336.121, and 337.280 nm), niobium (309.418, 316.340, 319.498, and 322.548 nm), and zirconium (327.305, 339.198, 343.823, and 349.621 nm) loadings were analyzed using inductively coupled plasma atomic emission spectroscopy (ICP-AES, iCAP 7600, Thermo Scientific) by comparing calibrated standard solutions.

Prior to nitrogen physisorption, catalysts were degassed at 120 °C under dynamic vacuum for 18 h using a Smart VacPrep (Micromeritics). Nitrogen adsorption/desorption isotherms were collected at 77 K using a Tristar II (Micromeritics). Cyclohexene vapor adsorption isotherms on bare supports (NU-1000 and SiO_2) were collected at 313 K, 353 K, and 383 K using a 3 Flex (Micromeritics). Isosteric heat of adsorption of cyclohexene on SiO_2 was calculated between 0.5-2 cm^3 (STP)/g_{SiO2} (a regime that adsorption amounts depend linearly on cyclohexene pressure) using Equation (3.1).

$$\frac{d}{dT}(\ln(\mathrm{P_{c6}}))\bigg|_{\mathrm{n_{ads}}} = \frac{\Delta H_{ads}}{RT^2}\bigg|_{\mathrm{n_{ads}}} \tag{3.1}$$

3.2.3 Catalysis

A reactor system was built by our team based on a design shown in Scheme 3.1. The system has equipped with a syringe pump (KDS) to inject liquid-phase H_2O_2 through a FEP (fluorinated ethylene propylene) capillary tube (Valco Instruments, 1/16 inch OD, 0.03 inch ID), such tube material has advantage over stainless-steel tube with regard to minimize decomposition of H_2O_2, connected to a plastic syringe (Norm-Ject, 10 mL). A reactant vapor (cyclohexene in this study) was introduced through a quartz bubbler (Wilmad Labglass, 1/4 inch connection with extra coarse frit). The reactor furnace (Northwestern University Instrument Shop) consists of three aluminum heating blocks separated by ceramic insulator to minimize heat conduction between adjacent blocks. The temperatures of all three aluminum heating blocks were individually controlled by a Quad-K temperature controller (J-KEM scientific) that were connected with K-type thermocouples (Omega) and stainless-steel sheath cartridge heaters (Omega, 150 Watts). During kinetic tests, temperature of inlet block is fixed at 110 °C to minimize H_2O_2 thermal decomposition (Figure 3.1 presents massive fluctuation of product TOS at 150 °C), as well as to ensure complete vaporization of H_2O_2 liquid (Figure 3.2 shows discontinuity on TOS at 80 °C), and that of outlet block is fixed at 115 °C to minimize products thermal decomposition (an example at 150 °C is given in Figure 3.3).

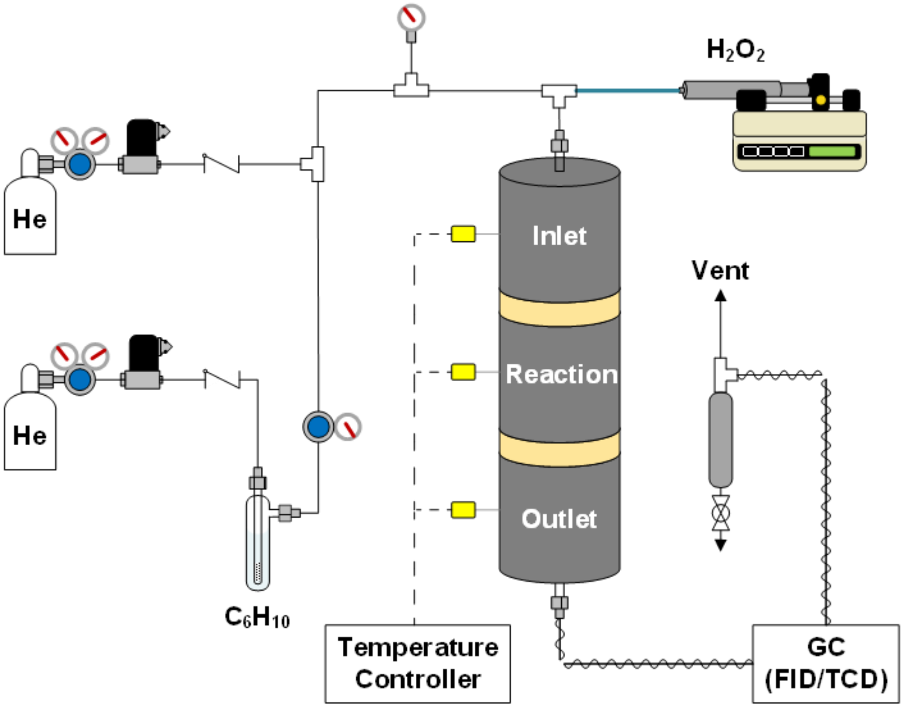

Scheme 3.1. Vapor-phase hydrogen peroxide reactor scheme.

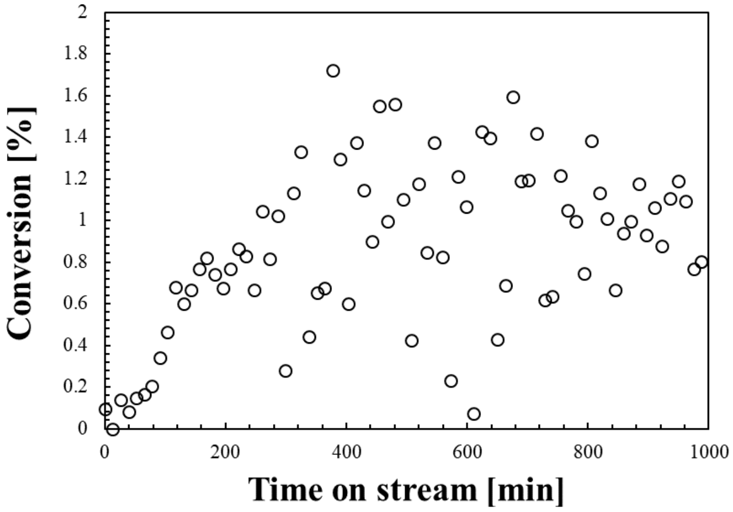

Figure 3.1. Conversion profile at 150 °C of inlet heating block temperature.

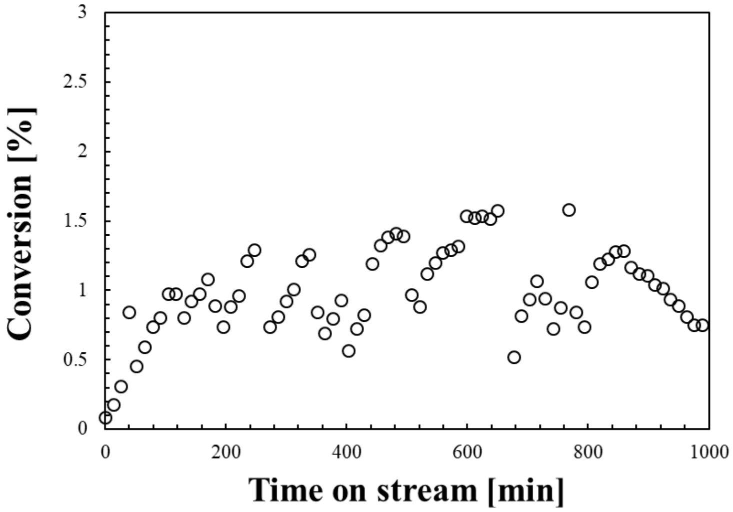

Figure 3.2. Conversion profile at 80 °C of inlet heating block temperature.

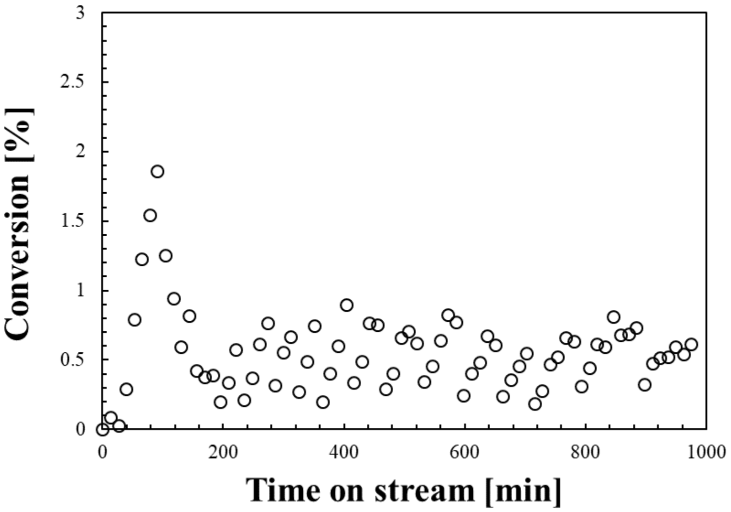

Figure 3.3. Conversion profile at 150 °C of outlet heating block temperature.

Kinetic tests were performed at a temperature of the reaction heating block, and this temperature was varied (110, 120, 130, 140, and 150 °C) to test apparent activation barriers of catalysts. M-SiO_2 (20 mg) and M-NU-1000 (10 mg) were both diluted in 200 mg of quartz sand, and these catalysts bed were supported on quartz wool in a quartz tube reactor (Wilmad Labglass, 18 inch long and 3/4 inch diameter). The reactor block kept at the reaction temperature before loading the catalyst bed. After loading the quartz tube reactor, cyclohexene (Sigma-Aldrich, ≥ 99.0 %) was introduced by He (5 mL/min, 99.999 %, Airgas) bubbler and diluted by He (20 mL/min) with ambient pressure at 25 °C (11.9 kPa). Two He flow rates were controlled by mass flow controllers (Brooks Instruments). Molar concentration of cyclohexene was varied by above two He flow rates (sum of total He flow rates kept same, i.e. 25 mL/min in total), and this concentration was used to calculate partial pressure that varied 0.6 to 3 kPa. Aqueous H_2O_2 (30 wt. %) was diluted in acetonitrile (10 mL H_2O_2 and 20 mL acetonitrile), and then 7 g of anhydrous magnesium sulfate was added to dry water, followed by decanting to yield 4 M H_2O_2 in acetonitrile solution.[43] Then, this solution was loaded in a plastic syringe with an extra care to remove any bubbles in it, and then this solution was injected directly into the quartz tube reactor with a rate of 0.2 mL/hr. Unlike cyclohexene case, we diluted 4 M H_2O_2 further with acetonitrile to vary its partial pressure (0.8 to 3 kPa), and the injection rate was fixed at 0.2 mL/hr. Here, a vertical location of the end tip of the FEP capillary tube was required to be located inside of the inlet heating block, otherwise a droplet would be formed and then lead incomplete vaporization as well as discontinuity of the oxidant injection (Figure 3.4) Concentration profiles of the reactant and products were collected up to 1000 min of time-on-stream (TOS). Carbon products were separated by HP-INNOWAX (50 m length, 0.2 mm diameter, 0.4 μm film) column. Identification and quantification of them were analyzed by a flame ionization detector (FID) that is equipped in a 7890 A GC (Agilent Technologies). Carbon products detected in this work were cyclohexene oxide (epoxide), trans-1,2-cyclohexane diol (diol), 2-cyclohexen-1-one (cyclohexenone), 2-cyclohexen-1-ol (cyclohexenol), and cyclohexanone (cyclohexanone). Oxygenated products (H_2O, O_2, CO_2) were separated by a combination of HP-PLOT/Q (30 m length, 0.53 mm diameter, 40 μm film) and HP-MOLESIEVE (15 m length, 0.53 mm diameter, 50 μm film). A thermal conductivity detector (TCD) in the same GC were used to analyze oxygenated products and He (Airgas, 99.999 %) was used as a carrier gas.

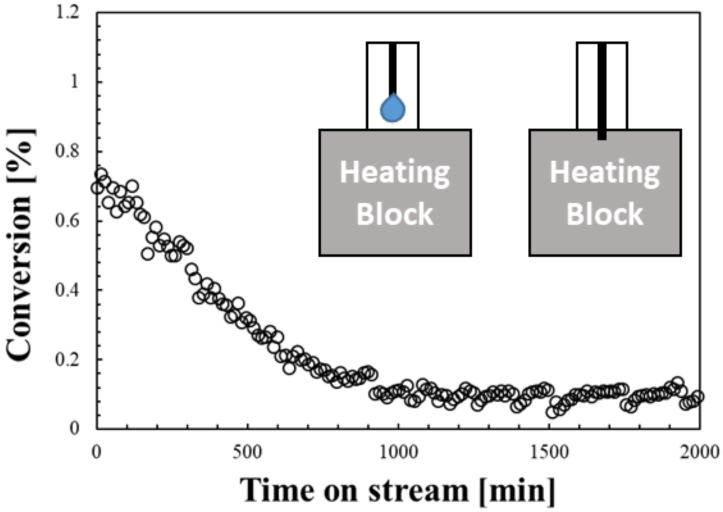

Figure 3.4. Conversion profile with the end tip of the FEP capillary tube being located above heating block (shown as left scheme in the Figure, right scheme is favorable).

Cyclohexene conversions were calculated by Equation (3.2). All conversions collected for all kinetic measurements were in the differential conversion regime (< 10 %). Steady (> 400 min TOS) conversion was extrapolated linearly to time at 0 min to calculate turnover frequencies (TOF). H_2O_2 conversions were not directly measured, however we detected via TCD that all H_2O_2 converted to H_2O.

$$\text{cyclohexene conversion} = \frac{\sum \text{mol}_{\text{product}}}{\text{mol}_{\text{reactant}} + \sum \text{mol}_{\text{product}}} \tag{3.2}$$

Here, a summation of molar concentration of products was obtained by Equation (3.3).

$$\sum \text{mol}_{\text{product}} = \text{mol}_{\text{epoxide}} + \text{mol}_{\text{diol}} + \text{mol}_{\text{enone}} + \text{mol}_{\text{enol}} + \text{mol}_{\text{anone}} + \frac{\text{mol}_{\text{CO}_2}}{6} \tag{3.3}$$

3.3 Results

3.3.1 Catalysts Synthesis

Table 3.1 summarizes the bulk properties of the catalysts synthesized in this study. All catalysts were synthesized with the intent to possess low surface density (i.e. a high dispersion of MO_x). This would lead to active Lewis acid sites for heterolytic H_2O_2 activation as shown in our previous works.[30, 43, 81] In the case of M-NU-1000, we were able to achieve low surface density with high metal loading due to spatial isolation of grafting sites (Zr_6 node) by a lengthy (~ 1 nm) linkers. As one can expect, surface areas of bare supports is decreased upon grafting of metal precursors. For M-SiO_2, we calcined the catalysts after grafting of metal precursors to generate MO_x sites. On the other hand, in the case of M-NU-1000, we exposed the catalysts in the ambient air after grafting to yield MO_x sites. This is because NU-1000 support would collapse and burn with high calcination temperature (550 °C).

Table 3.1. Summary of catalysts.

Catalyst	**M loading [wt. %]**	**Surface density [M/nm^2]**	**BET Surface area [m^2/g$_{catalyst}$]**
Ti-SiO_2[a]	0.87	0.2	380
Nb-SiO_2[a]	1.66	0.2	300
Ti-NU-1000[b]	5.16	0.3	1930
Nb-NU-1000[b]	9.55	0.3	1330

[a] Bare SiO_2 surface area 550 m^2/g.
[b] Bare NU-1000 surface area 2160 m^2/g.

3.3.2 Catalysis

Vapor-phase cyclohexene epoxidation with H_2O_2 was examined to study trends in reactivity and selectivity over M-SiO_2 and M-NU-1000. Although there are complexities such as temperature of inlet box, a placement of H_2O_2 feed tube (discussed in experimental section) that are arising from introduction of cyclohexene vapor and vaporized H_2O_2, we can achieve stable conversion profile over long time-on-stream (Figure 3.5 and Figure 3.6). All kinetic tests were performed in the differential conversion regime for cyclohexene. The reaction is run in the absence of external transport limits (Figure 3.7) with epoxide/diol selectivity being independent on temperature, partial pressures of cyclohexene and H_2O_2 for all materials tested.

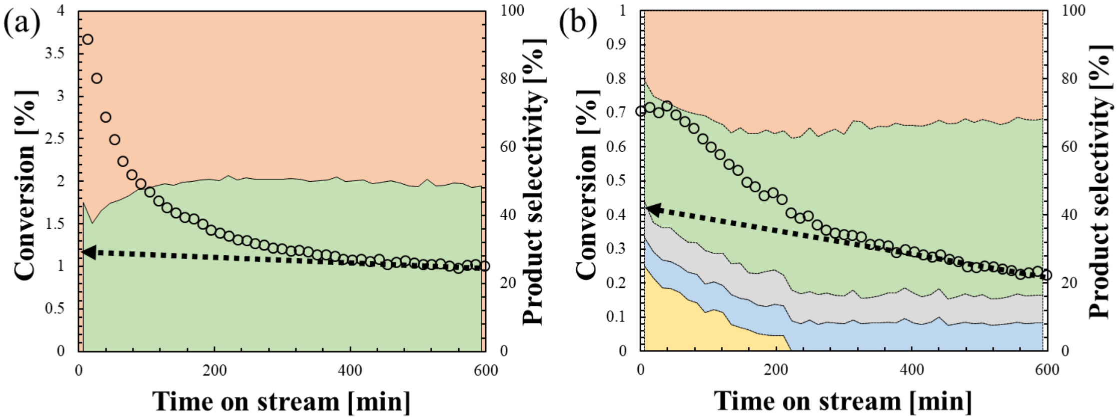

Figure 3.5. Representative time-on-stream conversion and C_6 product selectivity profiles of cyclohexene epoxidation with H_2O_2 at 120 °C, cyclohexene 3 kPa, H_2O_2 3 kPa over (a) Ti-SiO_2 and (b) Ti-NU-1000. (○ cyclohexene conversion, 🟩epoxide, 🟧diol, 🟨cyclohexanone, 🟦cyclohexenol, ⬜cyclohexenone) Dashed direction lines show how steady conversions (back to time at 0 min) are considered. Only selectivity to C_6 products show in (b) for clarity. See Figure 3.8 (a) for representative selectivities including CO_2.

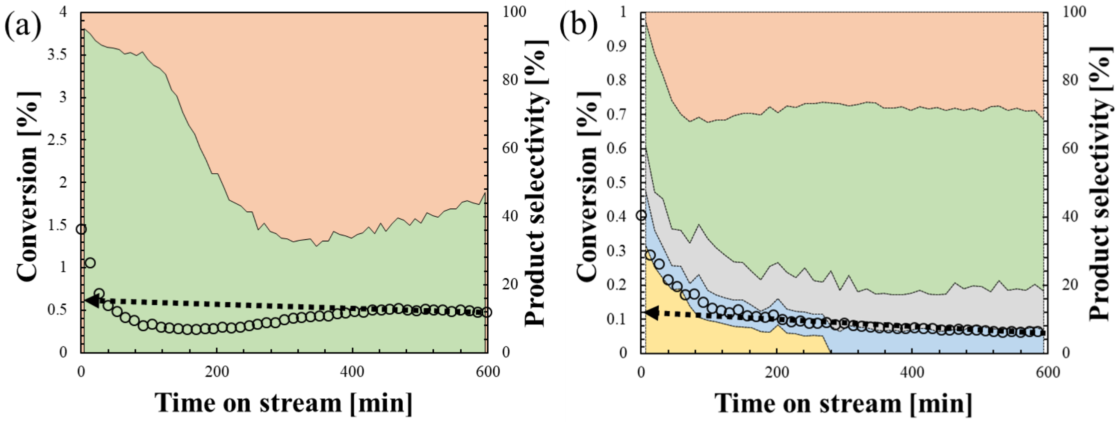

Figure 3.6. Representative time-on-stream conversion and C_6 product selectivity profiles of cyclohexene epoxidation with H_2O_2 at 120 °C, cyclohexene 3 kPa, H_2O_2 3 kPa over (a) Nb-SiO_2 and (b) Nb-NU-1000. (○ cyclohexene conversion, 🟩epoxide, 🟧diol, 🟨cyclohexanone, 🟦cyclohexenol, ⬜cyclohexenone) Dashed direction lines show how steady conversions (back to time at 0 min) are considered. Only selectivity to C_6 products show in (b) for clarity. See Figure 3.8 (b) for representative selectivities including CO_2.

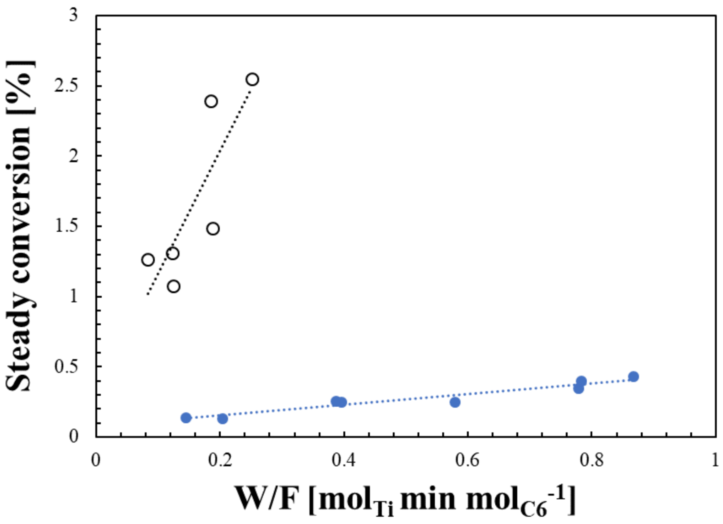

Figure 3.7. Cyclohexene steady conversions under different W/F at 120 °C, cyclohexene 3 kPa, H_2O_2 3 kPa (○Ti-SiO_2, ● Ti-NU-1000).

Conversion profiles of both catalysts trend same as they decrease sharply over the first ~ 200 min, then reach a relatively steady conversion. After the initial period, the activity over Ti-SiO_2 or Nb-SiO_2 (Figure 3.5 (a) and Figure 3.6 (a)) is very stable, while the activity over Ti-NU-1000 or Nb-NU-1000 continues to decrease with TOS. For these catalysts, selectivity within the C_6 species is largely constant after the initial period. On the other hand, assuming all M sites are accessible over two catalysts, rate of cyclohexene conversion over Ti-SiO_2 (0.107 mol_{C6} mol_{Ti}^{-1} min^{-1}) is ten times faster than the rate over Ti-NU-1000 (0.011 mol_{C6} mol_{Ti}^{-1} min^{-1}). In addition, there is a products selectivity difference between two catalysts. Silica supported Ti catalyst yields only epoxide and trans-cyclohexanediol each at ~50% selectivity under all reaction conditions studied. Neither allylic oxidation C_6 products (e.g. cyclohexanol) nor CO_2 were detected under all temperatures and pressures studied with the M-SiO_2 catalysts. No cis-cyclohexanediol was detected, indicating that all diol was derived from hydrolysis of epoxide, rather than direct cisdihydroxylation.[111] In contrast, NU-1000 supported Ti and Nb (Figure 3.5 (b) and Figure 3.6 (b)) catalysts produce a variety of C_6 products including cyclohexanone, cyclohexenol, and cyclohexanone, in addition to epoxide and diol. Among those products, cyclohexanone only appears at the beginning of TOS (~ 200 min). This is an uncommon product from cyclohexene oxidation that we will discuss below. On the other hand, selectivity of other C_6 products (epoxide, diol, cyclohexenol, and cyclohexanone) remains constant.

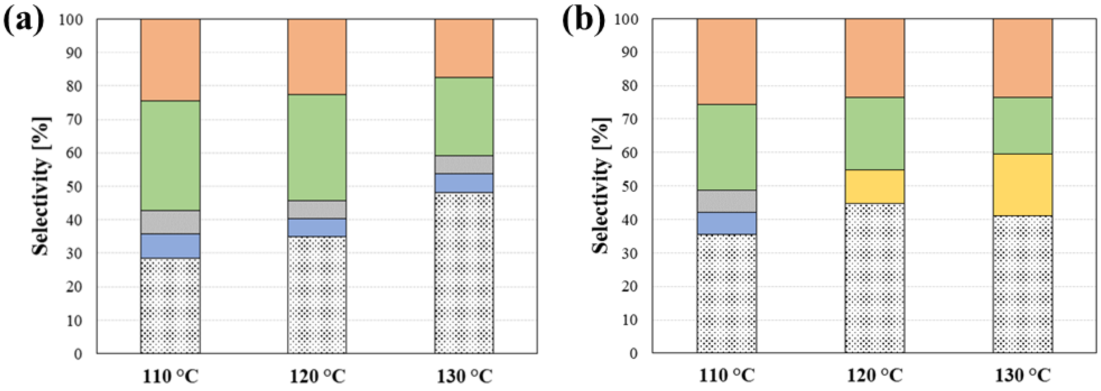

Figure 3.8. Selectivity dependence on reaction temperatures over (a) Ti-NU-1000 and (b) Nb-NU-1000 (cyclohexene 3 kPa, and H_2O_2 3 kPa) at 400 min (▨CO_2/6, 🟦cyclohexenol, ⬜ cyclohexenone, 🟩epoxide, 🟧diol).

In addition, we observe over oxidation product (i.e. CO_2) that is only generated over M-NU-1000 catalysts. Figure 3.8 shows selectivity trends with respect to reaction temperatures (110 – 130 °C). Data were not collected above 130 °C for M-NU-1000 due to instability in the reaction rate. Selectivity to CO_2 and the radical-derived products cyclohexanol and cyclohexanone increases from ~ 40 % to ~ 60 % with increasing temperatures. However, selectivity among the other C_6 products is largely independent of reaction temperatures over the temperature range studied. The ratio between cyclohexenol and cyclohexenone is 1:1 regardless of reaction temperatures, consistent with a common origin through the decomposition of cyclohexenyl hydroperoxide.[94-96] As for M-SiO_2, all detected diol is trans-cyclohexanediol, indicating that it is produced from epoxide hydrolysis.

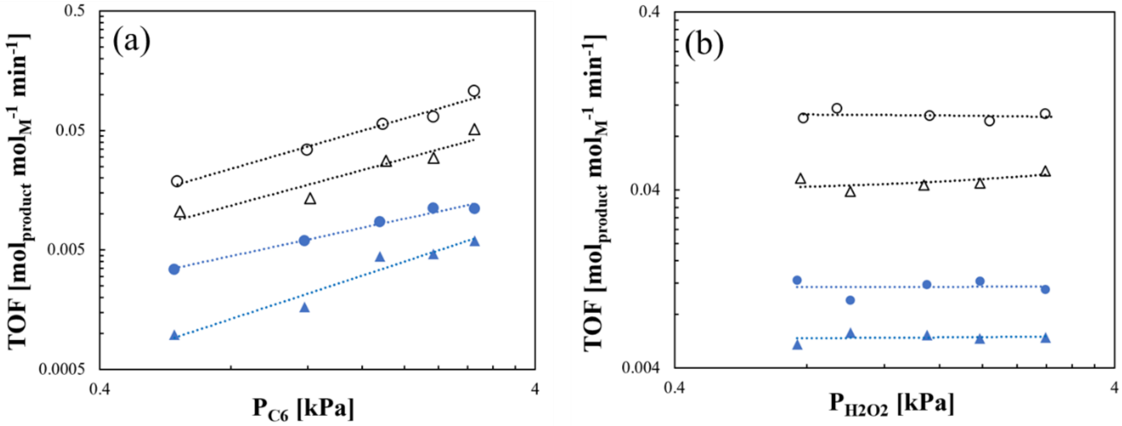

Figure 3.9. Reaction orders at 120 °C with respect to (a) cyclohexene (partial pressure: 0.6 to 3 kPa) with fixed H_2O_2 partial pressure at 3 kPa, and (b) H_2O_2 (partial pressure: 0.8 to 3 kPa) with fixed cyclohexene partial pressure at 3 kPa (○: Ti-SiO_2, △: Nb-SiO_2, ●: Ti-NU-1000, ▲: Nb-NU-1000). C_6 products and CO_2 are considered when calculating TOF.

Figure 3.9 gives reaction orders of M-SiO_2 and M-NU-1000 with respect to cyclohexene and H_2O_2. Orders of reaction with respect to cyclohexene are close to unity over all catalysts (Ti-SiO_2 1.1, Nb-SiO_2 1.0, Ti-NU-1000 0.8, Nb-NU-1000 1.3). Reaction orders with respect to H_2O_2 are near zero for all catalysts.

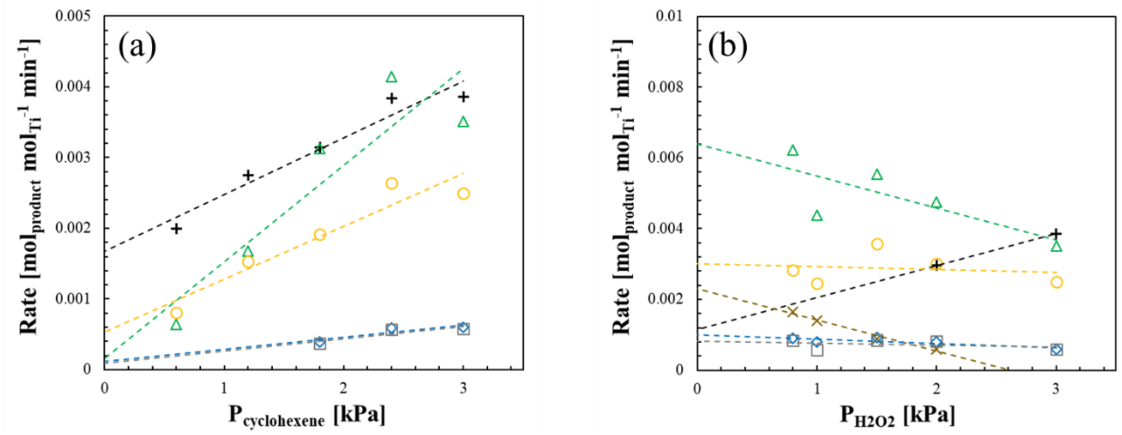

Figure 3.10. Rate of products formation dependence on reactant and oxidant partial pressures over Ti-NU-1000 at reaction temperature 120 °C at 400 min. Dependence on (a) cyclohexene partial pressures with H_2O_2 3 kPa (b) H_2O_2 partial pressures with cyclohexene 3 kPa (+CO_2/6, △epoxide, ○diol, ×cyclohexanone, ◇cyclohexenol, □cyclohexenone).

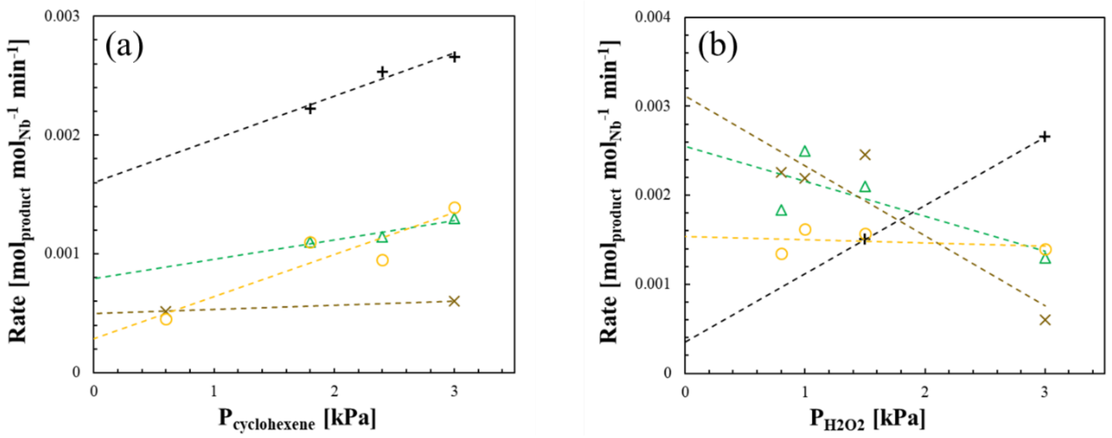

Figure 3.11. Rate of products formation dependence on reactant and oxidant partial pressures over Nb-NU-1000 at reaction temperature 120 °C at 400 min. Dependence on (a) cyclohexene partial pressures with H_2O_2 3 kPa (b) H_2O_2 partial pressures with cyclohexene 3 kPa (+CO_2/6, △epoxide, ○diol, ×cyclohexanone, ◇cyclohexenol, □cyclohexenone).

Moreover, we varied partial pressures of cyclohexene and H_2O_2 to study reaction orders dependence of products. Figure 3.10 (a) indicates that all rate of C_6 products and CO_2 formation linearly depend on partial pressure of cyclohexene. Note that only CO_2 has a non-zero intercept, presumably from organic solvent remaining in NU-1000. Varying H_2O_2 partial pressure (Figure 3.10 (b)), has a more complex impact on the reaction orders of product formation. As shown in Figure 3.5 (b) and Figure 3.6 (b), selectivites among epoxide, diol, cyclohexenol and cyclohexenone are relatively stable with TOS, but show a dependence with P_{H2O2}, where the diol/epoxide ratio increases at higher H_2O_2. This is consistent with epoxide hydrolysis via H_2O produced from H_2O_2 decomposition. In contrast, cyclohexanone selectivity always decreases with TOS. At a 400 min TOS (Figure 3.10 (b) and Figure 3.11 (b)), cyclohexanone decreases with P_{H2O2}, and CO_2 increases with P_{H2O2}. It should be noted that the low reaction rate of M-NU1000 means that as selectivites fall for some of these compounds, they fall below detection limits, but are presumably still present at lower amounts.

Nb-SiO_2 shows similar products selectivity in longer TOS to that of Ti-SiO_2 (Figure 3.6 (a)). In contrast, Nb-NU-1000 products have similar dependencies with respect to H_2O_2 and cyclohexene partial pressure. However, the selectivity to hydration/dehydration to diol and anone are higher, while there are even fewer C_6 radical species (cyclohexenol and cyclohexenone) than for Ti-NU1000 (Figure 3.11). This is consistent with trends seen in the condensed phase for Ti-SiO_2 vs. Nb-SiO_2.[30]

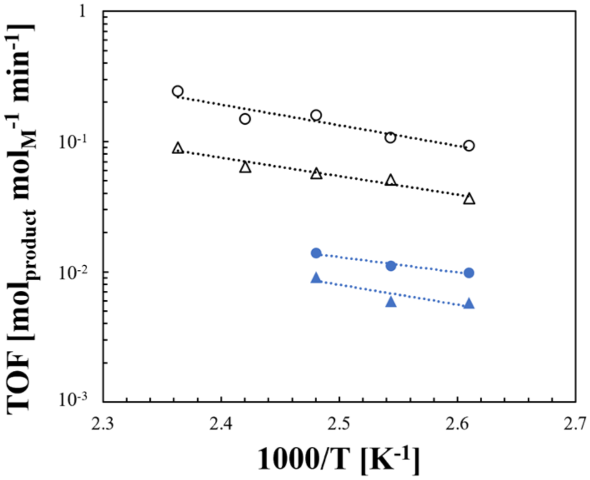

Figure 3.12. Arrhenius plot of catalysts. Cyclohexene 3 kPa and H_2O_2 3 kPa. Reaction temperatures: 110-150 °C over M-SiO_2, and 110-130 °C over M-NU-1000. (○: Ti-SiO_2, △: Nb-SiO_2, ●: Ti-NU-1000, ▲: Nb-NU-1000). C_6 products and CO_2 are considered when calculating TOF.

Figure 3.12 gives an Arrhenius plot of all catalysts collected at 3 kPa partial pressure of both cyclohexene and H_2O_2. All four catalysts have similar slopes, corresponding to apparent activations barriers of 26 ± 4 kJ mol^{-1} (Table 3.2). Table 3.2 also presents calculated activation enthalpies and entropies of all catalysts. As similar with apparent barriers, all catalysts have similar activation enthalpies (23 ± 4 kJ mol^{-1}) as well as similar activation entropies (-130 ± 20 kJ mol^{-1} K^{-1}). Only the data between 110-130 °C were used for M-NU-1000, because reaction rates to become unstable at higher temperatures.

Table 3.2. Apparent activation barriers, activation enthalpies and entropies of catalysts.

Catalyst	**E_a [kJ mol^{-1}]**	**$\Delta H^{\ddagger}$ [kJ mol^{-1}]^a**	**$\Delta S^{\ddagger}$ [kJ mol^{-1} K^{-1}]^a**
Ti-SiO_2	30	27	-110
Nb-SiO_2	27	24	-130
Ti-NU-1000	22	19	-150
Nb-NU-1000	29	26	-140

[a] Reported values are calculated using Eyring equation (Figure S8) and steady TOF.

3.4 Discussion

3.4.1 Cyclohexene epoxidation mechanism in the vapor-phase: M-SiO_2 vs. M-NU-1000

Gas phase reaction of H_2O_2 and cyclohexene over M-SiO_2 produces only epoxide and diol. The absence of any detectable radical-derived products (i.e. resulting from homolytic activation of H_2O_2) cyclohexenol and cyclohexanone contrasts with the results at typical condensed phase conditions, e.g. 65 °C, 1M cyclohexene in acetonitrile, where the direct epoxidation selectivity (i.e. only taking into account of heterolytic H_2O_2 activation) of Ti-SiO_2 and Nb-SiO_2 are 52 % and 84 %, respectively.[30] The results here are more comparable to selectivities observed by other studies at more dilute conditions over M-beta (< 50 mM cyclohexene in acetonitrile) that epoxide is the only product.[108] There is also no detectable over-oxidation to CO_2. Using cis-3-hexene (instead of cyclohexene) and H_2O_2 over M-SiO_2 catalysts result in only cis-3,4-epoxyhexane. This is consistent with epoxide formation by a concerted mechanism. Higher selectivity toward direct pathway (epoxide and diol) can be attributed from (1) low reactant partial pressures and attendant low C_6 surface concentrations, making it less likely that homolytic decomposition of the Ti-OOH will react with a C_6 species and (2) intrinsically more favorable direct pathway over radical pathway at higher reaction temperatures. Homolytic decomposition of H_2O_2 has a lower or comparable barrier to epoxidation over M-SiO_2 catalysts,[110] from which one would expect selectivity to improve with temperature.

This also contrasts with reaction selectivity over M-NU1000 where we see cyclohexenol, and cyclohexenone, in approximately 1:1 ratio, until the catalyst deactivates to the point that these species are no longer observable. This is consistent with radical oxidation to produce cyclohexenyl hydropeorixide as a primary product. We also detect CO_2 as a result of total oxidation of cyclohexene. At initial time on stream, we also detect cyclohexanone, which is not typically observed in the condensed phase at reaction $T < 85$ °C. Direct feed of cyclohexenol (with and without H_2O_2) does not produce cyclohexanone, ruling out its isomerization as a route to cyclohexanone. Direct feed of epoxide, without oxidant, also does not produce any cyclohexanone, ruling out its isomerization. Instead, co-feeding epoxide and H_2O_2 does produce cyclohexanone, suggesting that epoxide hydrolysis (from the H_2O formed by decomposing H_2O_2) to form trans-diol can then be followed by dehydration to cyclohexanone. Diol dehydration by ZrO_2 has frequently been reported,[112-116] such results suggest dehydration of diol is favorable over the free zirconia nodes of M-NU-1000 at elevated temperature. Unfortunately, the low vapor pressure of cyclohexanediol precludes direct addition of that species for aforementioned control test. In addition, the absence of cis/trans isomerization for M-SiO_2 argues against a stepwise radical attack at the C=C bond, which could in principle lead directly to cyclohexanone. The lower activity of M-NU1000 precluded this experiment over these materials. Interestingly, increasing either P_{H2O2} or exposure time of H_2O_2 (i.e. longer TOS) results in cyclohexanone decrease that is coupled with CO_2 increase. This may be the consequence of the surface modification by H_2O_2 contact above a certain threshold, which may lead changes from dehydration sites to combustion sites.

We propose an overall reaction mechanism shown in Scheme 3.2 and a simplified mechanism of radical pathways in Scheme 3.3.

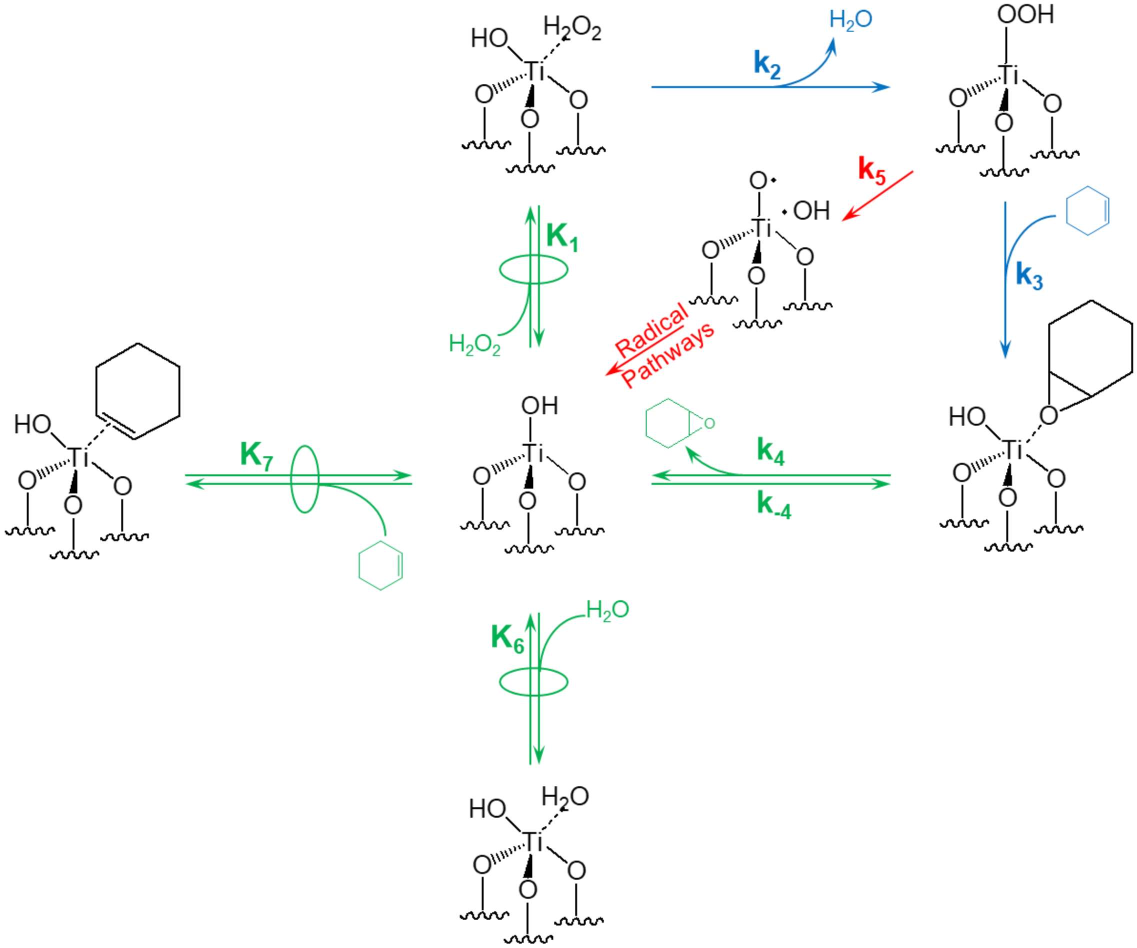

Scheme 3.2. Proposed mechanism of vapor-phase cyclohexene epoxidation in steady conversion regime with H_2O_2 over Ti-SiO_2/Ti-NU-1000

Scheme 3.2 illustrates proposed mechanism of cyclohexene epoxidation over TiO_x catalysts with a series of elementary steps. Analogous steps would be written on Nb-based catalysts. In all cases, we exclude cyclohexanone steps that are not relevant for longer periods of TOS under most of reaction conditions, and which may or may not be occurring on the MO_x sites. This proposed catalytic cycle presents quasi-equilibrated adsorption/desorption steps of H_2O_2 (K_1), water (K_6), and cyclohexene (K_7) on a bare Ti site. Following the mechanism of Bregante et. al.,[110] we assume Ti-OOH intermediate is formed upon irreversible activation of H_2O_2 (k_2). This active intermediate can form epoxide via a reaction with cyclohexene (k_3) or can undergo homolytic decomposition (k_5) that lead to radical pathways discussed further below. Upon epoxide formation, the epoxide can reversibly desorb (k_4/k_{-4}) or react further to diol which we will not consider for rate laws.

For $M\text{-}SiO_2$, since there are no evidences of radical-derived C_6 products or of CO_2, we do not consider the role of k_5 towards forming products. Here, measured rate is defined as the rate of epoxidation formation (r_{epox}):

$$r_{epox} = k_3[\text{Ti-OOH}][C_6H_{10}] \tag{3.4}$$

where k_x is the rate constant for step x in Scheme 3.2 and [A] is the concentration of species A, especially $[C_6H_{10}O^*]$ is the concentration of epoxide bound sites.

$$\frac{rate}{[\mathrm{M}]} = K_1 k_2 [H_2O_2]/\alpha \tag{3.5}$$

where [M] denotes total number of active sites, and α is the sum of all surface intermediates.

$$\alpha = 1 + K_1[H_2O_2] + \frac{K_1 k_2 [H_2O_2]}{k_3[C_6H_{10}] + k_5} + \frac{1}{k_4}\left(\frac{K_1 k_2 k_3 [C_6H_{10}][H_2O_2]}{k_3[C_6H_{10}] + k_5} + k_{-4}[C_6H_{10}O]\right) + K_6[H_2O] + K_7[C_6H_{10}] \tag{3.6}$$

where terms in Equation (3.6) represent bare active sites and those occupied by H_2O_2, Ti-OOH, epoxide, water, or cyclohexene, respectively. As mentioned above, we neglect k_5 (due to the absence of radical pathway products) to simplify.

Since $k_4 >> k_{-4}$, Equation (3.5) simplifies to

$$\frac{rate}{[M]} = k_3[C_6H_{10}] \tag{3.7}$$

which is consistent with the reaction orders shown in Figure 3.9, which is first orders with respect to cyclohexene and zeroth orders with respect to H_2O_2.

For M-NU-1000, we ought to consider radical pathways due to radical products (cyclohexenol, cyclohexenone, and CO_2) to obtain rates.

$$r_{epox} + r_{radical} = k_3[\text{Ti-OOH}][C_6H_{10}] + \mathrm{k}_5[\text{Ti-OOH}] \tag{3.8}$$

Thus, there is additional term corresponding to the rate of homolytic decomposition ($r_{radical}$) as shown in Equation (3.8).

$$\frac{rate}{[M]} = \mathrm{K}_1 k_2[H_2O_2]/\alpha \tag{3.9}$$

Over Ti-NU-1000, Equation (3.9) is identical to Equation (3.5). In this case, however, we must consider k_5 term.

Since $k_4 >> k_{-4}$, Equation (3.9) can be written as

$$\frac{rate}{[M]} = k_3[C_6H_{10}] + k_5 \tag{3.10}$$

which also is consistent with the reaction orders presented in Figure 3.9.

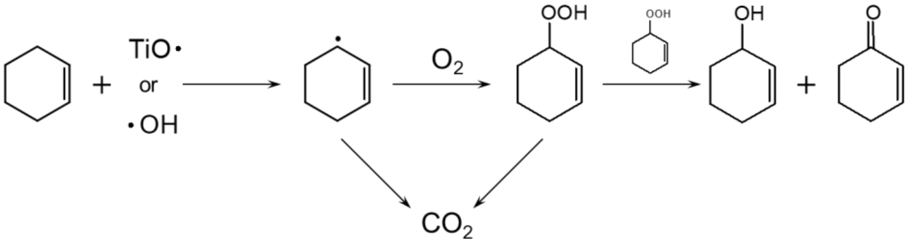

Scheme 3.3. Proposed mechanism of radical pathways

Herein, we propose simplified radical pathways – which are relevant for M-NU-1000 - in Scheme 3.3. Once cyclohexenyl hydroperoxide species formed, it can undergo a bimolecular pathway to yield cyclohexenol and cyclohexanone. Also, we observe CO_2 formation which can be the result of serial radical reactions to oxidize cyclohexene radical or cyclohexenyl hydroperoxide fully. As discussed above, we assume cyclohexanone comes from dehydration of diol, not from radical pathways.

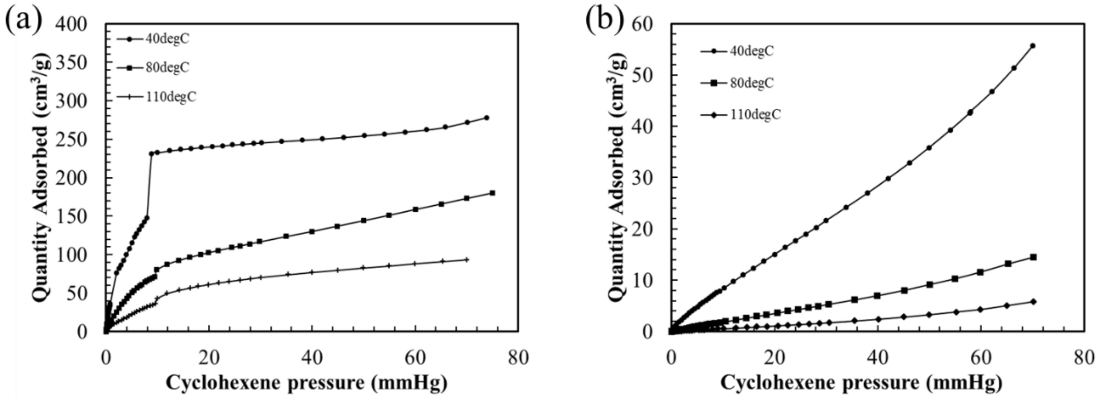

Figure 3.13. Cyclohexene vapor adsorption isotherms at 40, 80, and 110 °C on bare supports (a) on bare NU-1000, and (b) on bare SiO_2 (Quantity adsorbed measured at STP: standard temperature and pressure).

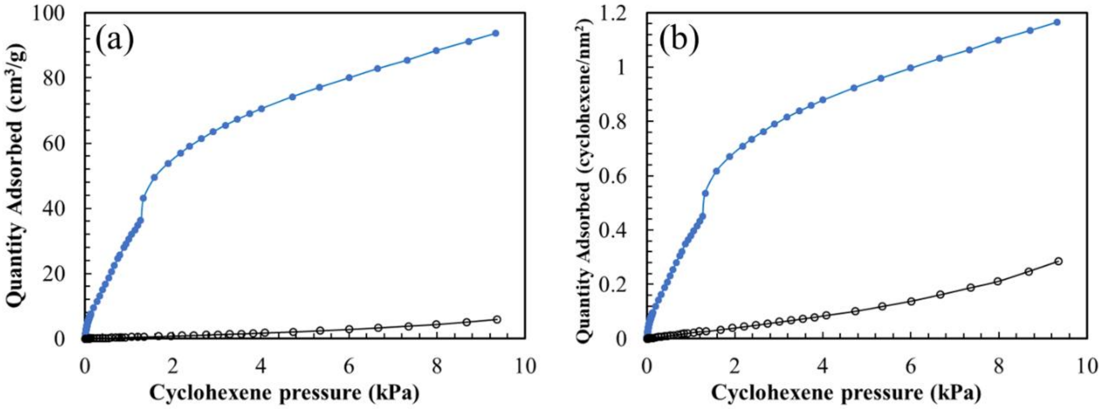

Figure 3.14. Cyclohexene vapor adsorption isotherms at 110 °C on bare supports (a) volume (at STP: standard temperature and pressure) of cyclohexene per mass of catalysts basis, (b) number of cyclohexene molecule per area of catalysts basis (○: SiO_2, ●: NU-1000).

To understand the reactant adsorption on bare supports, we collected cyclohexene vapor adsorption isotherms at 40, 80, and 110 °C (Figure 3.13). Among three temperatures, adsorption isotherms at 110 °C (Figure 3.14) were collected to represent reaction temperatures. Unlike SiO_2, NU-1000 shows a mesoporous step at 1.3 kPa as also shown in N_2 physisorption isotherms. At 110 °C and cyclohexene pressure at 3 kPa, which represents reaction condition, uptakes are 0.8 cyclohexene/nm^2 and 0.06 cyclohexene/nm^2 for NU-1000 and SiO_2, respectively (Table 3.3). Such difference leads to a high pore concentration of cyclohexene within NU-1000 under all realistic cyclohexene partial pressures. This difference in reactant population on surfaces may explain why homolytic decomposition of M-OOH species would then lead to radical oxidation of cyclohexene over M-NU-1000, whereas it would only lead to loss of oxidizing species over M-SiO_2.

Table 3.3. Cyclohexene uptake and heat of adsorption.

Support	**Uptake [cm^3/g$_{support}$]^a**	**Uptake [cyclohexene/nm^2]^a**	**Uptake [cyclohexene/M]^a**	**Heat of adsorption [kJ/mol]^b**
SiO_2	1.3	0.06	0.3	45
NU-1000	63.4	0.8	2.4	N/A^c

[a] Uptakes at 110 °C and 3 kPa to reflect reaction condition.
[b] Calculated using Equation 1 at 40, 80, and 110 °C.
[c] Complexity of NU-1000 isotherms in small uptake regimes preclude proper extracting heat of adsoprtion.

3.4.2 Selectivity difference between vapor- and condensed-phase: Nb-NU-1000.

Previously, we have investigated the same reaction over Nb-NU-1000 (indicated as Nb-SIM in the previous study), but in condensed-phase (acetonitrile as a reaction solvent, 1M cyclohexene) at 65 °C.[43] In previous study, Nb-NU-1000 showed 57-72 % of direct pathway selectivity (over 300 min) depending on NU-1000 crystal size. In other words, this catalyst activated 28-53 % of H_2O_2 homolytically. As a result, we have observed cyclohexenone and cyclohexenol products. However, in vapor-phase, as mentioned above, we observe cyclohexanone and CO_2 additionally that we argue cyclohexanone comes from direct pathway and CO_2 does from radical pathways. We adopt similar approach from our previous work to calculate direct pathway selectivity (Equation (3.13)) of the reaction at 120 °C, it is 63 % (at 100 min TOS) initially and decays to 53 % (at 600 min TOS) in steady conversion regime that are comparable with results from the condensed-phase. In this equation, we consider contributions from cyclohexanone (as one of direct products) and CO_2 (as one of all products) that are not produced in condensed-phase.

$$\text{Pathway selectivity} = (\text{mol}_{\text{epoxide}} + \text{mol}_{\text{diol}} + \text{mol}_{\text{anone}}) / \text{mol}_{\text{all products}} \times 100\% \qquad (3.13)$$

Decrease in pathway selectivity is owing to decay of cyclohexanone in longer TOS. Interestingly, C_6 selectivities under both reaction phases are similar, indicating that the presence or absence of solvent does not change the *relative* barriers to formation of the various C_6 products.

3.4.3 Comparison of vapor- and condensed-phase: M-SiO_2.

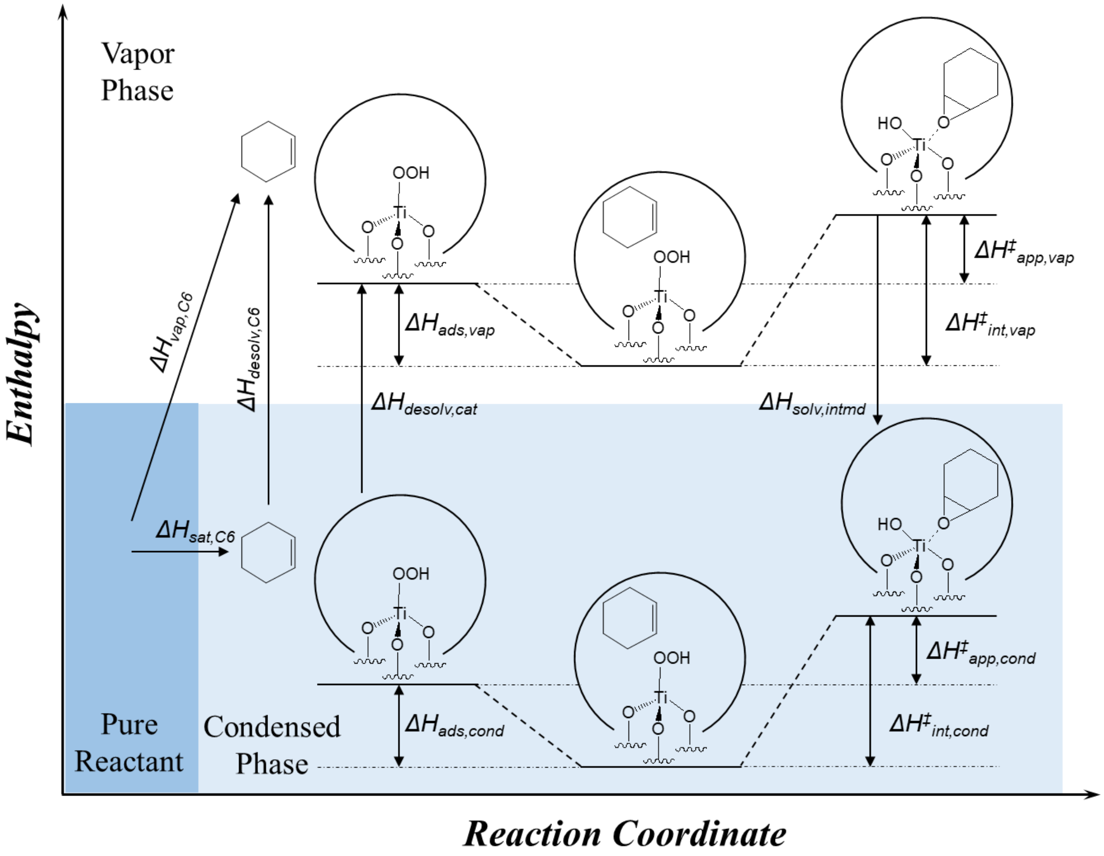

Scheme 3.4. Proposed Born-Haber thermochemical cycle[117] of cyclohexene epoxidation in condensed phase and vapor phase

Scheme 3.4 presents proposed Born-Harber thermochemcial cycle of cyclohexene epoxidation in condensed- and vapor-phases. We can obtain intrinsic reaction barrier ($\Delta H^{\ddagger}_{int}$) by Equation (3.14).

$$\Delta H^{\ddagger}_{app} = \Delta H^{\ddagger}_{int} - |\Delta H_{ads}| \tag{3.14}$$

Resulting $\Delta H^{\ddagger}_{int}$ for Ti-SiO_2 and Nb-SiO_2 are 72 kJ/mol and 69 kJ/mol, respectively. Interestingly, these barriers do not depend on the identity of MO_x sites when surfaces are not surrounded by reaction solvent. This contrasts with previous finding of styrene epoxidation in condensed phase, which intrinsic barriers differ by 30 kJ/mol between TiO_x and NbO_x (Ti-SiO_2: 48 kJ/mol, Nb-SiO_2: 75 kJ/mol).[110] Unfortunately, due to the absence of heat of adsorption of cyclohexene (in acetonitrile) on bare SiO_2, we are not able to compare intrinsic barriers in condensed- and vapor-phases directly. However, given apparent barriers of M-beta catalysts (Ti-β: 43 kJ/mol, Nb-β: 72 kJ/mol)[108] as well as considering intrinsic barriers are independent of the identity of support,[110] we can carefully expect that intrinsic barrier of TiO_x in both phases are similar (72 kJ/mol vs. (43 + $|\Delta H_{ads}|$) kJ/mol) and that of NbO_x are different to some extent (69 kJ/mol vs. (72 + $|\Delta H_{ads}|$) kJ/mol). This may indicate a role of solvent affecting reactivity in condensed-phase condition.

3.5 Conclusions

A vapor-phase peroxide reactor has been built to study H_2O_2 activation during cyclohexene epoxidation over Lewis acid sites, and the results of SiO_2- and NU-1000-supported TiO_x and NbO_x catalysts were compared. We observe that the two catalyst supports give very different selectivity from each other in the vapor-phase, which was not seen as significantly in the condensed-phase reaction. M-SiO_2 catalysts in this work do not yield any conceivable radical derived products but only do yield direct products (epoxide and diol), the results contrast with the results from previous condensed-phase studies. On the other hand, M-NU-1000 catalysts produce radical species (cyclohexenol, cyclohexenone, and CO_2) in the vapor-phase. In particular, Nb-NU-1000 shows similar direct pathway selectivity (about 60%) with our observation in condensed-phase. Based upon the results of cyclohexene vapor adsorption, we hypothesize that the presence of radical products over M-NU-1000 may be attributed to more reactant population than over M-SiO_2. Consequences of such population could be related to more chances for radicals to react further with neighboring reactant. Moreover, the absence of an external reaction solvent can potentially result in difference of intrinsic barriers between vapor- and condensed-phases. The ability to understand H_2O_2 activation in the absence of an external solvent is expected to be broadly useful in understanding Lewis acid catalysts.

Chapter 4. Pushing the Limits on Metal–Organic Framework as a Catalyst Support: NU-1000 Supported Tungsten Catalysts for *o*-xylene Isomerization and Disproportionation

This chapter presents a modified version of the following manuscript:

Sol Ahn, Scott L. Nauert, Cassandra T. Buru, Martino Rimoldi, Hyeju Choi, Neil M. Schweitzer, Joseph T. Hupp, Omar K. Farha, and Justin M. Notestein, *J. Am. Chem. Soc.*, **2018**, 140 (27), 8535-8543.

4.1 Introduction

Isomerization and disproportionation reactions of hydrocarbons such as hexane and xylene are crucial reactions in the production of fuels and basic petrochemicals, and these reactions have also long been model reactions that provide structural information on solid acid catalysts.[118-120] Tungstated zirconia (WO_x-ZrO_2) is one example of a material capable of carrying out a wide range of solid acid catalysis such as alkane isomerization,[121-122] alcohol dehydration[123] and etherification,[124] and *o*-xylene isomerization.[125-127] WO_x-ZrO_2 is typically synthesized by impregnation on amorphous supports and subsequent calcination. These materials have very strong structure sensitivity,[128] in which the structure of the active material strongly influences the rate. As such, the use of conventional syntheses that cause heterogeneity of active sites can complicate the understanding of the material's overall reactivity. Phosphotungstic acid (PTA, $H_3PW_{12}O_{40}$) is a Keggin polyoxometalate (POM) cluster that can provide the tungsten oxide active sites for the aforementioned model reactions owing to its activity for acid catalysis. For instance, pure PTA has been reported for depolymerization of polytetrahydrofuran[129] and alkylation of toluene.[130] Researchers have extensively studied PTA as heterogeneous acid catalysts on various supports.

Kukovecz et al. reported sol-gel incorporation of PTA on silica for alkene isomerization,[131] Devassy et al. impregnated PTA on zirconia for phenol alkylation,[132] and Macht et al. deposited PTA on SiO_2 via incipient wetness impregnation for alcohol dehydration.[133]

Separately, many researchers have been studying metal–organic frameworks (MOFs) as catalyst supports potentially capable of creating uniform active sites placed in controlled pore environments.[12-13, 134-135] It is generally hypothesized that catalysts with more uniform and isolated active sites will lead to better understanding of the catalytic surface phenomena.[28, 43] In addition, MOFs have various applications in many fields such as gas storage and separation,[6-10] drug delivery,[136] or sensors.[11, 137] In particular, the zirconium-based MOF, NU-1000, possesses outstanding chemical and hydrothermal stability relative to many MOFs.[17, 21] Further, the hexa-zirconium (Zr_6) nodes are only 8-connected via tetracarboxylate (1,3,6,8-tetrakis(p-benzoate)pyrene, $(TBAPy)^{4-}$) linkers, providing four additional grafting sites on each node in the form of four terminal and four bridging hydroxyl groups. The size of the tetracarboxylate linkers places each Zr_6 cluster at least 1.0 nm from one another, ensuring site isolation for small grafted species such as single metal ions.[39, 50] Finally, three distinct pore openings are created with csq-net topology. Hexagonal and triangular pores of 3.1 and 1.2 nm, respectively, are aligned along the a-axis, while 1.0 nm rhomboid pores are aligned along the c-axis (Figure 4.1).[54]

Recently, Zhang et al. encapsulated PTA in MIL-101, a Cr-based MOF, for sugar dehydration.[138] Also, Wang et al. synthesized WO_x-ZrO_2 using UiO-66 as a precursor for acetalization of benzaldehyde.[139] These studies among others[140-145] have significantly developed MOF-based Brønsted-acidic catalysts, but in some cases, MOFs are unstable under the reaction conditions. In this study, we encapsulate a high weight-loading of PTA within NU-1000 and show that the POM and MOF structures remain intact following the representative strong acid-catalyzed reaction of *o*-xylene isomerization/transmethylation. The structures and reactivities of NU-1000-supported PTA catalysts are compared to a reference WO_x-ZrO_2 and to a WO_x-loaded NU-1000 synthesized by an alternate route. To the best of our knowledge, this work provides the first example of an acid-catalyzed, hydrocarbon skeletal isomerization reaction – a class of important benchmark strong Brønsted acid-catalyzed reactions for the petrochemicals industries – occurring within a MOF.

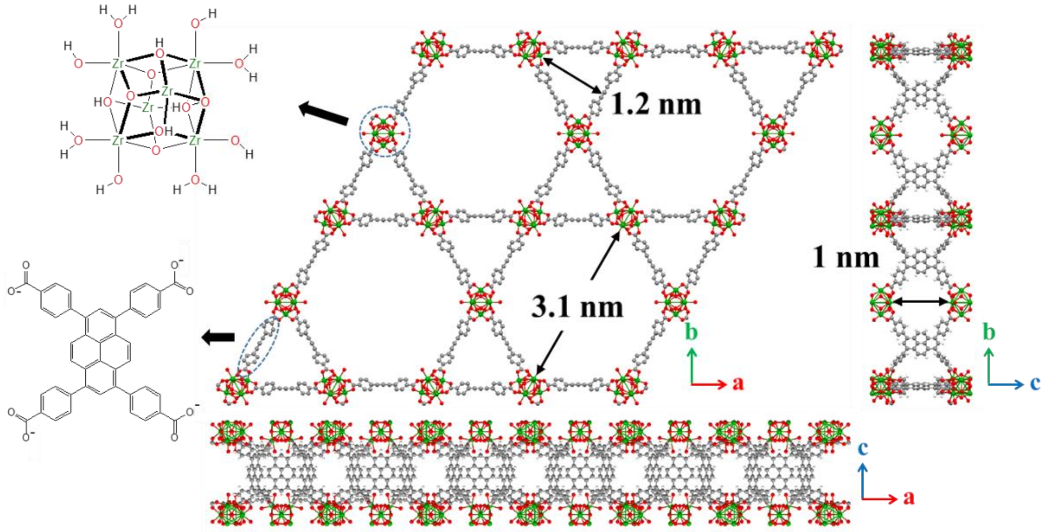

Figure 4.1. Crystal structure of NU-1000. The structures of Zr_6 node (top left) and organic linker (bottom left) are given. Dark green=Zr, red=O, gray=C, white=H

4.2 Experimental Methods

4.2.1 Synthesis of Catalysts

The catalyst support, NU-1000, was synthesized and activated following the published literature.[22] The control material WO_x-ZrO_2 was synthesized via incipient wetness impregnation and calcined according to a protocol in the literature.[125] Phosphotungstic acid ($H_3PW_{12}O_{40}$) was encapsulated in NU-1000 (PW_{12}@NU-1000) via addition of PTA (2 eq. PTA to Zr_6 node for 0.9 PW_{12}@NU-1000 and 0.5 eq. PTA to Zr_6 node for 0.5 PW_{12}@NU-1000) dissolved in water following a procedure previously developed by our team.[146] For the synthesis of W-SIM (Solution phase grafting in MOFs), 200 mg of NU-1000 (92.6 μmol of Zr_6 node) and 235.1 μL (8 tungsten equivalents to one Zr_6 node) of bis(tert-butylimido)bis(dimethylamino)tungsten (VI) (Strem, min. 97% BTBMW) were dissolved in 5 mL heptane (99 %, anhydrous, Sigma Aldrich) in an argon-filled glove box for 24 h with occasional swirling. The mixture was decanted, and then mixed 5 mL of fresh heptane for 4 times to remove unreacted tungsten precursor. After this washing step, the material was transferred out from the glove box, and then a similar washing step was repeated but with acetone. Upon exposure to moist air, both amines and imines ligands from the tungsten precursor were removed to form tungsten oxide clusters on the nodes of NU-1000.[66]

4.2.2 Characterization of Catalysts

Tungsten (209.475, 209.860, 224.875, and 239.709 nm) and zirconium (327.305, 339.198, 343.832, and 349.621 nm) loadings were collected using inductively coupled plasma atomic emission spectroscopy (ICP-AES, iCAP 7600, Thermo Scientific). One mg amounts of catalysts were digested in 0.75 mL sulfuric acid (ACS reagent, 95-98 %, Sigma Aldrich) and 0.25 mL of 30 wt.% hydrogen peroxide (aqueous, Sigma Aldrich) solution with the aid of microwave using Initiator+ (Biotage) at 150 °C for 5 min.

Nitrogen physisorption isotherms at 77 K were collected using a Tristar II (Micromeritics), and DFT (Density Functional Theory) pore size distributions were derived from the desorption isotherms. Prior to the measurement, samples were dried at 120 °C under dynamic vacuum for 18 h using a Smart VacPrep (Micromeritics).

Powder X-ray diffraction (PXRD) patterns were collected on a SmartLab diffractometer (Rigaku) with a Cu-Kα radiation source (45 kV and 160 mA for tube voltage and current, respectively). Diffraction patterns were recorded over the 2θ range of 2–20° with a 0.05° step width and a 5°/min scan speed.

Solid-state CP MAS ^{13}C and ^{31}P NMR spectra were collected on a 400 MHz VNMRS spectrometer (Varian) equipped with a conventional triple resonance 5 mm probe-head in double resonance mode. Samples were packed in a zirconia rotor, and the spinning frequency was set at 10 kHz. Chemical shifts (δ [ppm]) were referenced to adamantane and $(NH_4)H_2PO_4$ for ^{13}C and ^{31}P, respectively. Solution ^{1}H NMR spectra were recorded on an AVANCE III 600 MHz (Bruker). Used catalysts were washed with CD_2Cl_2 (Cambridge Isotope Laboratories, D 99.8 %) to extract organic molecules from the samples. Spectra were obtained applying a 30° pulse, an acquisition time of 2.7 s, a delay time of 5 s (after finding that the much longer delay value of 20 s did not affect the area ratios between STD and analyte), and accumulating 16 scans. Spectra were carefully phased and baseline corrected. Quantification was performed comparing the areas of the peaks of the reference compound (1,4-dimethoxybenzene) and the target compound (*o*-xylene). Spectra were collected at the IMSERC (Integrated Molecular Structure Education and Research Center) facility at Northwestern University.

W L_3-edge X-ray absorption spectroscopy (XAS) was performed at sector 5 of the Advanced Photon Source, Argonne National Laboratory, on the Dupont-Northwestern-Dow Collaborative Access Team (DND-CAT) bending magnet D beamline using a Si(111) double crystal monochromator. All measurements were performed in transmission mode with Canberra ionization chambers. Energies were calibrated against a W foil reference spectrum collected with each sample spectrum by setting the W foil first inflection point at the known W L_3-edge to 10207 eV. Catalysts pellets were pressed into specially made Al sample holders, dried under vacuum at 120 °C, then cooled and switched to flowing He before data collection. Scans were performed with a 0.6 eV increment in the pre-edge region and 0.05 $Å^{-1}$ intervals between 3.0 $Å^{-1} < k < 14.0$ $Å^{-1}$. Counting time per data point was increased from 1 to 5 s from beginning to end of scans to maximize signal count at high k. XAS spectra were processed in Athena using standard methods. Spectra were normalized by fitting a cubic polynomial to 150-700 eV above the edge and subtracting the expected absorption at the edge. The background was removed using the AUTOBK algorithm with R=1.0 and spline range from 0.5 $Å^{-1} < k < 13.5$ $Å^{-1}$ when computing $\chi(k)$. The Fourier transform was performed on the k^2-weighted $\chi(k)$ function over the range 3 $Å^{-1} < k < 12.8$ $Å^{-1}$ using a Hanning window function with width dk = 0.5 $Å^{-1}$.

4.2.3 Catalysis

Kinetic studies were carried out in a flow reactor at 523 K using 50-100 mg of catalysts to maintain differential conversion regime (< 10 %). Catalysts that were supported on quartz wool were loaded in a quartz tube reactor. The reactor was heated to 523 K with a ramp rate of 5.0 K/min under flow of H_2 (10 mL/min, 99.999 %, Airgas). *o*-xylene (≥ 99.0 %, Sigma-Aldrich) was introduced by Ar (10 mL/min, 99.999 %, Airgas) bubbler with a total pressure of 1 bar at 298 K (0.87 kPa of reactant). Reactions were carried out at 523 K for 4 h, and then heated at 5.0 K/min to 573 K for 4 hours under same flow condition. Subsequently, only Ar (20 mL/min) was supplied throughout the system to remove physisorbed species for 6 h at 573 K. Gas flow rates were controlled by mass flow controllers (Altamira Instruments). Online products identification and quantification were performed by a 7890 A GC (Agilent Technologies) equipped with a flame ionization detector (FID) and HP-INNOWAX (30 m length, 0.32 mm diameter, 0.15 mm film). The mass balance with respect to the products and unreacted *o*-xylene for all runs exceeded 95 %. Initial turnover frequencies were calculated based on conversions extrapolated linearly to time at 0 min from the trend of time-on-stream *o*-xylene conversion between 80 and 240 min. The reaction and online GC analysis were performed in Clean Cat core facility at Northwestern University.

4.3 Results and Discussion

4.3.1 Synthesis and Characterization

Table 4.1 summarizes the bulk properties of the W-loaded catalysts synthesized in this study. The reference WO_x-ZrO_2 possesses 16.5 wt% W, corresponding to 1.6 W/nm^2, or 22% of a monolayer (0.22 W/Zr_{surf}), when considering the N_2 physisorption surface area and Zr atom surface density of the original support. W-SIM (<u>S</u>olution phase grafting <u>i</u>n <u>M</u>OFs) is synthesized by a self-limiting method that gives a similar W loading by mass, but a much lower surface density based on total N_2 physisorption surface area, due to the high total surface area of the MOF. However, surface density may be more useful if normalized to surface zirconium atoms, since W will not be grafted directly on the organic linkers. Assuming that all the Zr atoms in the nodes are accessible, W-SIM reaches 0.41 W/Zr_{surf} or 2.5 W per Zr_6 node. This loading is typical of deposition of mononuclear precursors by grafting or atomic layer deposition (ALD) within NU-1000, which typically does not exceed 4 metals per Zr_6 node when the MOF is intact.[28, 43-44, 46, 51, 65] In W-SIM, ^{1}H NMR confirmed the complete removal of the precursor ligands (*tert*-butylimido and dimethylamino) and thus the conversion of W-N and W=N into a supported WO_x. Finally, two different loadings of PW_{12}@NU-1000 are synthesized by exposure of NU-1000 to aqueous PTA solutions. To synthesize 0.5 PW_{12}@NU-1000, NU-1000 is exposed to 0.5 equivalents of PTA to one Zr_6 node resulting in loadings of 30.6 wt% W, 0.4 W/nm^2 total N_2 physisorption surface area, and 0.9 W per surface Zr. To obtain higher POM loading, 0.9 PW_{12}@NU-1000 was synthesized with two equivalents of PTA per Zr_6, following a previously published procedure.[146] Our team previously shown uniform distribution of PTA within the NU-1000 in case of 0.9 PW_{12}@NU-1000,[146] and we confirmed uniform distribution of PTA of 0.5 PW_{12}@NU-1000 as well (Figure S1). With exposure to excess PTA, the material contains 44.9 wt% W, corresponding to 0.5 W/nm^2, or 1.7 W/Zr_{surf}. This is equivalent to 10.3 W per Zr_6 node or 0.86 POM per Zr_6 node; approximately 1 POM per node appears to be the maximum value. After loading the W-containing species, W-SIM and the two PW_{12}@NU-1000 samples have lower surface areas than the original NU-1000 based on gravimetric surface area, as expected, and these composites still possess the characteristic mesopores (step around P/P_o=0.2-0.25 in Figure 4.2 (a) and pore widths in Figure 4.2 (b)) as well as micropores of NU-1000. Additionally, diffuse reflectance infrared Fourier transform (DRIFT) spectra (Figure 4.3) show a decrease in the O-H stretch (3670 cm^{-1}) from the non-H bonded hydroxyl and aqua ligands for both W-SIM and 0.9 PW_{12}@NU-1000 relative to the starting material, consistent with anchoring/encapsulation of WO_x clusters via the hydroxyl ligands of NU-1000.

Table 4.1. Summary of catalysts.

Catalyst[a]	W loading		BET Surface area	Volumetric Surface area	Surface density	Surface density
	[wt% W]	[W/Zr_6 node]	[$m^2/g_{catalyst}$]	[$m^2/cm^3_{NU\text{-}1000}$]	[W/nm^2]	[W/Zr_{surf}]
ZrO_2	n/a	n/a	270	n/a	n/a	n/a
WO_x-ZrO_2	16.5	n/a	125[b]	n/a	1.59	0.22[b]
NU-1000	n/a	n/a	2160	1050	n/a	n/a
W-SIM	17.0	2.5	930[c]	560	0.20	0.41[c]
0.5 PW_{12}@NU-1000	30.6	5.4	1150[c]	840	0.37	0.90[c]
0.9 PW_{12}@NU-1000	44.9	10.3	740[c]	700	0.54	1.72[c]

[a] These values were reproducible in errors of ± 3.5 % from three different catalyst synthesis batches

[b] Calculated based on surface Zr density of zirconia,[88-89] 7.34 Zr/nm^2

[c] Assuming every Zr of NU-1000 node is exposed on the surface

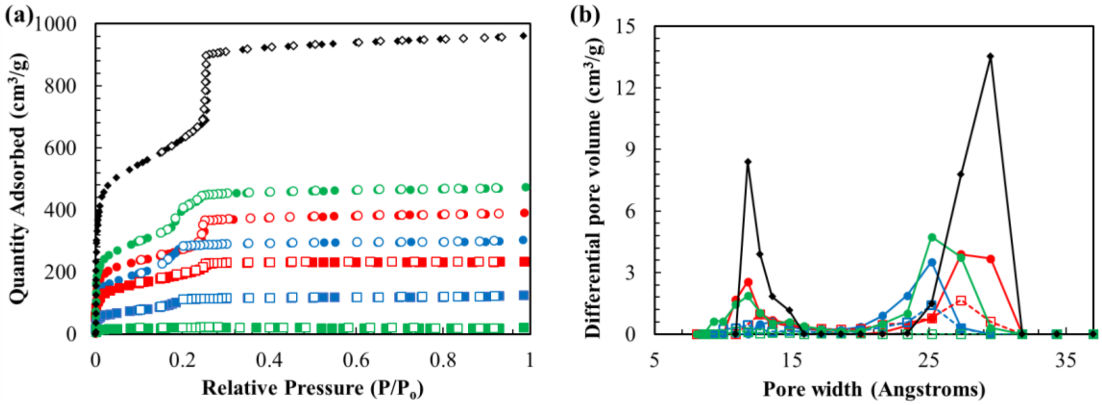

Figure 4.2. (a) N_2 physisorption adsorption/desorption isotherms and (b) DFT (carbon slit pore N_2 77 K kernel) pore size distributions of W-SIM (red), 0.5 PW_{12}@NU-1000 (green), and 0.9 PW_{12}@NU-1000 (blue). Circles: as synthesized, squares: after catalysis.

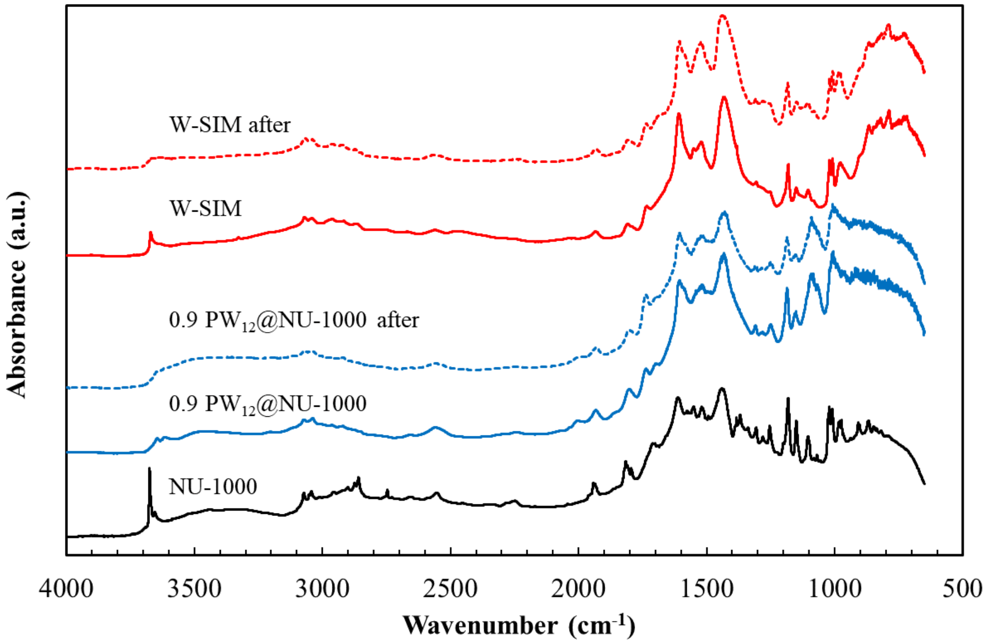

Figure 4.3. DRIFT spectra of catalysts

Considering the W loadings and surface densities alone, the two PW_{12}@NU-1000 catalysts and the control WO_x-ZrO_2 are expected to contain some active WO_x clusters, while the W-SIM may possess highly dispersed W atoms that would not be catalytically active. In addition, the relatively low diffuse reflectance UV-vis (DRUV-vis) edge energy of WO_x-ZrO_2 of 2.95 eV (Figure 4.4) is consistent with the presence of WO_x clusters.[125] DRUV-vis is unfortunately not diagnostic for NU-1000 supported catalysts due to the strongly-absorbing organic linkers that overlap the WO_x edge.

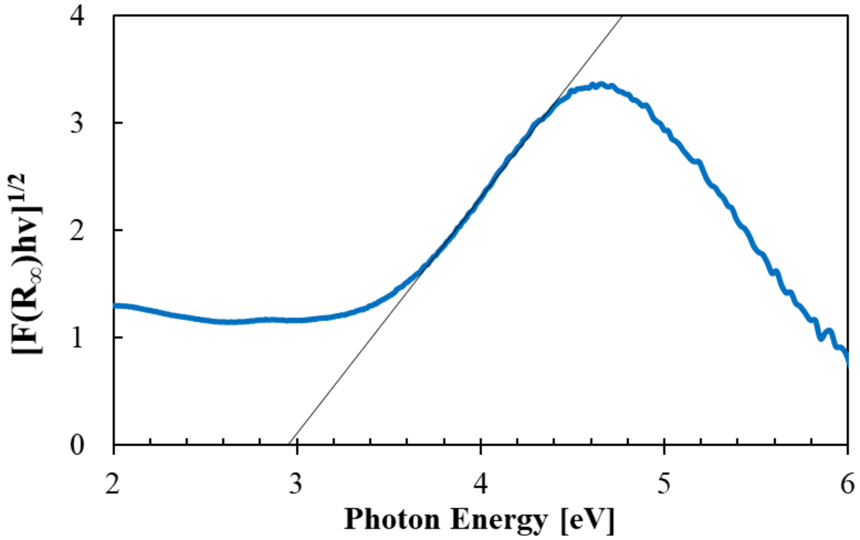

Figure 4.4. DRUV-vis of WO_x-ZrO_2

PXRD patterns (Figure 4.5 (a)) show that the long-range order of the MOF framework in W-SIM and 0.9 PW_{12}@NU-1000 are maintained upon W deposition and after *o*-xylene isomerization reaction conditions. Peak broadening observed in the case of W-SIM after catalysis might indicate partial loss of structural integrity. For the as-synthesized PW_{12}@NU-1000 catalysts, these patterns have been previously assigned to the presence of POM clusters located in the small triangular channels of NU-1000.[146]

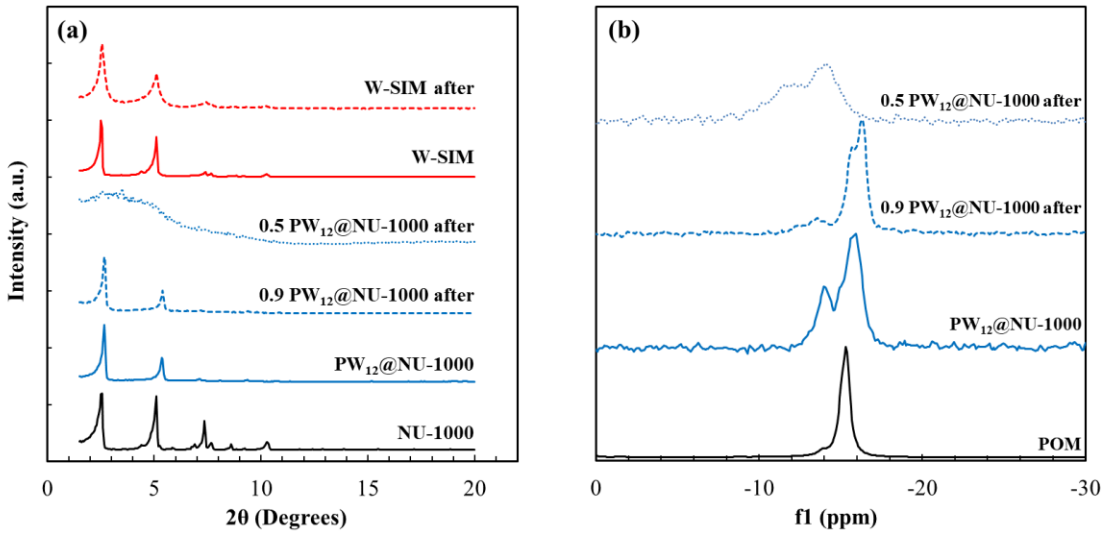

Figure 4.5. Bulk structure characterizations of catalysts (a) PXRD patterns, and (b) Solid-state ^{31}P CP MAS NMR

NMR and EXAFS help indicate the possible structures of the WO_x species present in these materials. Solid-state ^{31}P cross polarization magic angle spinning (CP MAS) NMR spectra (Figure 4.5 (b)) confirm that the POM structure is intact upon synthesis and after the reaction. Pure (solid) POM presents a sharp peak at -15 ppm that is attributed to the symmetric central P atom,[147] and very small feature at -14 ppm. Kozhevnikov et. al. reported a feature at -14 ppm that increased with decreasing POM loading on silica.[148] In our case, this feature is intense in the as-synthesized catalyst and diminishes significantly after the reaction. Given that the material will dehydrate during reaction, we suggest that this feature is related to POM in a hydrated or hydroxyl-rich environment. We attribute the feature at -16 ppm in both fresh and used catalysts to the direct interaction of POM and the Zr_6 nodes of NU-1000.

EXAFS results support the presence of WO_x clusters in PW_{12}@NU-1000 and isolated W atoms in W-SIM. A strong feature centered around 3.2 Å in Figure 4.6 (a) has been assigned to W-O-W scattering in WO_x clusters.[149] On the other hand, W-SIM does not present strong features in this regime, indicating negligible WO_x cluster formation (Table 4.1). Furthermore, the two peaks at 1.2 and 1.5 Å in Figure 4.6 (b) are assigned to W=O and W–O, respectively. The stronger relative intensity of W=O to W–O in W-SIM compared to 0.9 PW_{12}@NU-1000 is further consistent with isolated WO_x sites in W-SIM and extended WO_x domains in 0.9 PW_{12}@NU-1000.

The low surface density and the EXAFS are both indicative of isolated WO_x groups in W-SIM, which in turn predicts that W-SIM would have negligible reactivity toward *o*-xylene isomerization. Isolated metal oxides cannot readily delocalize charge,[125] resulting in weak or absent Brønsted acid behavior.

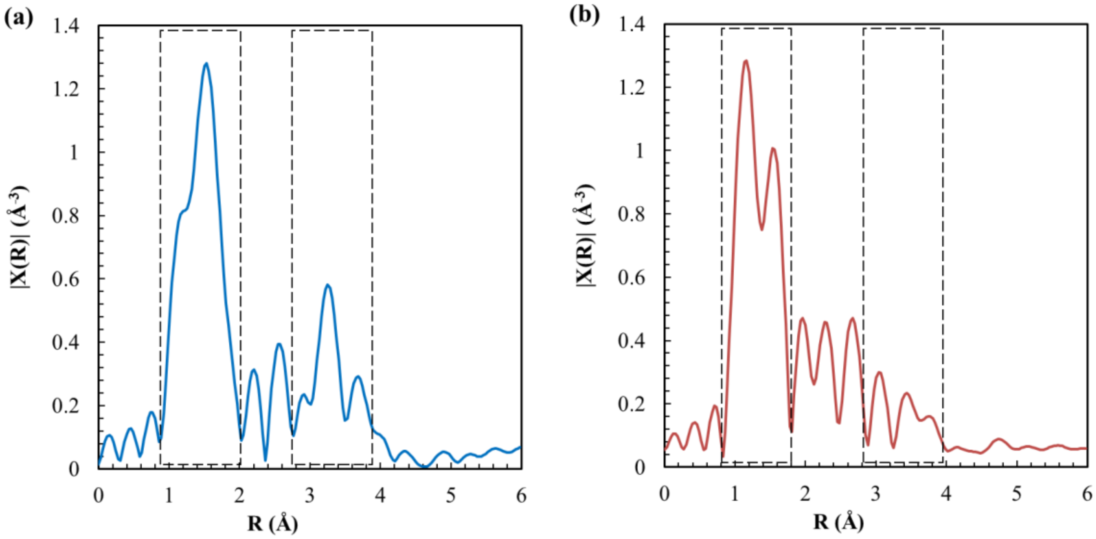

Figure 4.6. R- space EXAFS spectra of (a) 0.9 PW_{12}@NU-1000, and (b) W-SIM

4.3.2 Catalysis

Previous reports state that *o*-xylene catalysis rates and selectivities are strongly dependent on the local WO_x structure.[125-126] Rates per W atom increase up to monolayer capacity for WO_x-ZrO_2 and then fall at higher loadings as WO_x becomes sterically inaccessible. Similarly, it has been reported that moderate POM loadings on TiO_2 surfaces are more favorable than either well-dispersed POMs or large aggregates of POMs. In the former, strong interactions with the support limit the acidity, while in the latter, extended clusters of POMs limit acid site accessibility.[150]

Table 4.2. Summary of catalysis.

Catalyst[a]	**Initial TOF [mol mol_W^{-1} hr^{-1}] [b]**	**Selectivity [%][c]**	
		Isomerization	**Disproportionation**
WO_x-ZrO_2	0.11	100	0
NU-1000	< 0.01[d]	-	-
W-SIM	< 0.01[d]	-	-
0.5 PW_{12}@NU-1000[e]	< 0.01[d]	-	-
0.9 PW_{12}@NU-1000	0.16	17	83

[a] 50-100 mg catalyst (to match amount of W) to reach <10% conversion, 523 K in 10 sccm *o*-xylene/Ar and 10 sccm H_2 at nominal 1 bar pressure. NU-1000 supported catalysts (including 0.9 PW_{12}@NU-1000) were inactive at 423 K and 473 K. Catalysis data were collected from triplicate runs of three different catalyst synthesis batches. See experimental methods for full details.

[b] Extrapolated to 0 min from the trend of *o*-xylene conversion between 80 and 240 min.

[c] Isomerization (*m*- and *p*-xylene) or disproportionation (toluene and trimethylbenzene) products divided by total products at 240 min time-on-stream (TOS).

[d] TOF of 0.01 reflects the detection limit of FID.

[e] Catalysts 0.3, 0.4, and 0.7 PW_{12}@NU-1000 catalysts are similarly unreactive.

Table 2 compares reactivities and selectivities of the four catalysts. At one extreme, W-SIM is inactive for *o*-xylene catalysis, as predicted by its site isolation. At the other extreme, WO_x-

ZrO_2 is active and stable with time-on-stream (Figure 4.7), consistent with its well-established use in this reaction. The 0.5 PW_{12}@NU-1000 catalyst also showed no activity at any time, indicating that the POM and/or MOF structure collapsed (Figure 4.5) during the catalyst pre-heating to 523 K or immediately upon the start of the reaction. In contrast, 0.9 PW_{12}@NU-1000 shows initial reactivity (per W atom basis) even higher than WO_x-ZrO_2. To understand the difference in the two catalysts, we note that with the absence of activity, 0.5 PW_{12}@NU-1000 lost most of its surface area (70 m^2/g) and porosity (Figure 4.2). Likewise, the long-range NU-1000 crystal structure of 0.5 PW_{12}@NU-1000 collapsed during catalysis (Figure 4.5 (a) and Figure 4.8 (a)). Lastly, 0.5 PW_{12}@NU-1000 lost integrity of the POM cluster, as shown by the loss of the features at -15 and -16 ppm, and their replacement by broad features between -10 and -14 ppm (Figure 4.5 (b)). Instability of POM in harsh catalytic conditions as well as deactivation has been reported for many other POM systems.[151-152] Although not listed in Table 4.2, similarly-synthesized catalysts with POM loadings from 0.3 to 0.7 POM per Zr_6 node also showed no activity at any time, and for none of these was the long-range order maintained after the catalytic test (Figure 4.8 (b)). In contrast, the crystal structure of the bare NU-1000 support was retained after catalytic conditions (Figure 4.8 (c)), and likewise, long-range crystal (Figure 4.5 (a)) and POM structure (Figure 4.5 (b)) of the catalytically active 0.9 PW_{12}@NU-1000. Maximal loading of POM within the NU-1000 framework appears to synergistically stabilize both the POM and the MOF structure.

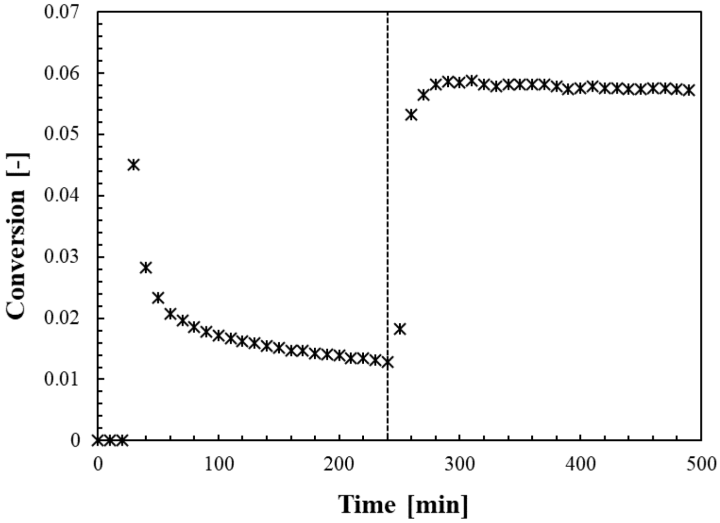

Figure 4.7. Time-on-stream: *o*-xylene conversion over WO_x-ZrO_2 at 523 K (before 240 min) and 573 K (after 240 min). Under flow of H_2 (10 mL/min, 99.999%) and *o*-xylene (≥ 99.0%) was introduced by Ar (10 mL/min, 99.999%) bubbler with a total pressure of 1 bar at 298 K (0.87 kPa of reactant).

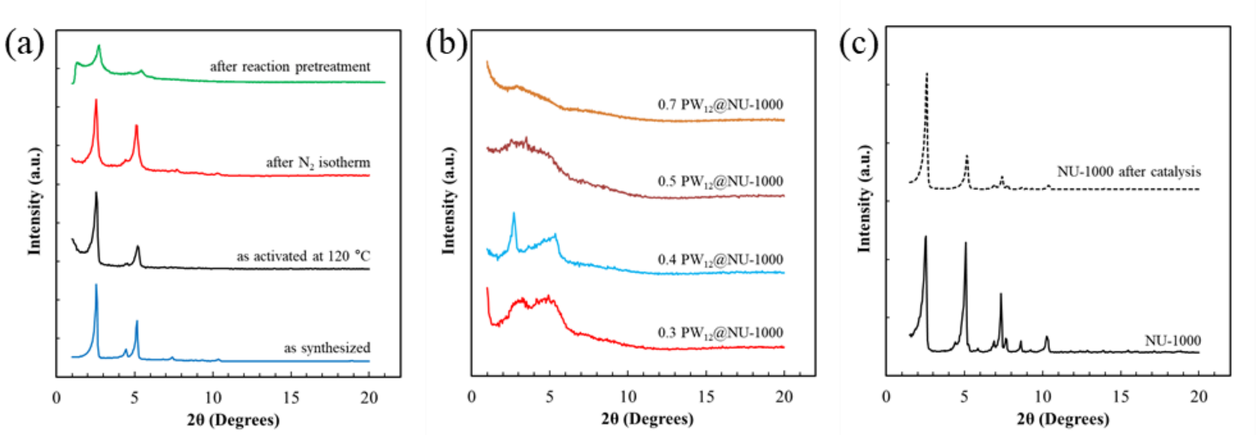

Figure 4.8. PXRD patterns of (a) 0.5 PW_{12}@NU-1000, (b) lower POM loadings after catalysis, and (c) NU-1000.

The absence of reactivity for low loadings may have analogies to other studies in which, for example, catalysts of low POM loadings on silica support show less activity for alkane isomerization. In such cases, isolated POM clusters coordinate with three surface silanols, leaving no available protons for acid catalysis.[153-154] Since POM clusters are appeared to be uniformly distributed within the NU-1000 (Figure 4.9), intra-particle inhomogeneity is a less plausible explanation for no reactivity. At the same time, however, we also observe pore collapse under pretreatment condition which obscures understanding the activity and stability of these catalysts. In contrast, completely filling the MOF with POMs appears to physically prop open the catalyst structure in much the same way that one would pillar a clay material,[155-157] preventing loss of long-range order and catalytic reactivity. PTA is known to have a particularly strong interaction with ZrO_2,[158] which may cause the MOF to collapse around the POM if physically able.

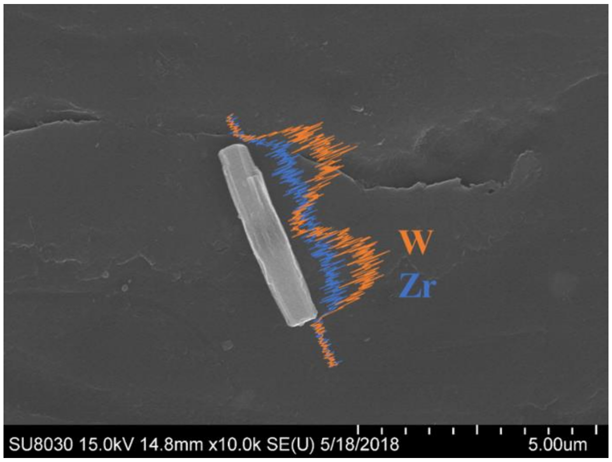

Figure 4.9. SEM image and EDX line scans of 0.5 PW_{12}@ NU-1000

Although having good initial reactivity, 0.9 PW_{12}@NU-1000 deactivates gradually over time at 523 K, as shown in Figure 4.10 (a). Some activity is regained upon moving to a higher temperature, but the catalyst resumes deactivating immediately. This is similar behavior to many other microporous solid acid catalysts for C-C isomerization. For example, van Donk et. al. reported deactivation of solid acid catalysts under butene skeletal isomerization.[159] Also, Srivastava et. al. reported deactivation of MFI and MCM under 1,2,4-trimethylbenzene isomerization.[160] Moreover, Wang et al reported deactivation of ZSM-5 under n-butane isomerization.[161] Further optimization of reaction conditions may be able to minimize its impact. As already noted, Figure 4.5 (a) shows that this deactivation is not due to wholesale loss of the MOF long-range order, and Figure 4.5 (b) confirms that the POMs remain intact, although there may be some reorganization of POMs within the pores of the support. Also, Figure 4.2 (a) and (b) indicate that meso- and micropores of NU-1000 are still present, and that the mesopores in particular have not changed in dimensions. Mass balance for this reaction is good (higher than 95%), excluding excessive coking, and there is no change to the physical appearance of the catalysts after the reactions.

While the organic ligands of the MOF prevent regenerating the catalyst by calcination, as well as precluding analysis of coke by TGA, no species were detected upon purge under inert flow at 573 K. This observation rules out the possibility of deactivation due to simple condensation of species within the pores.

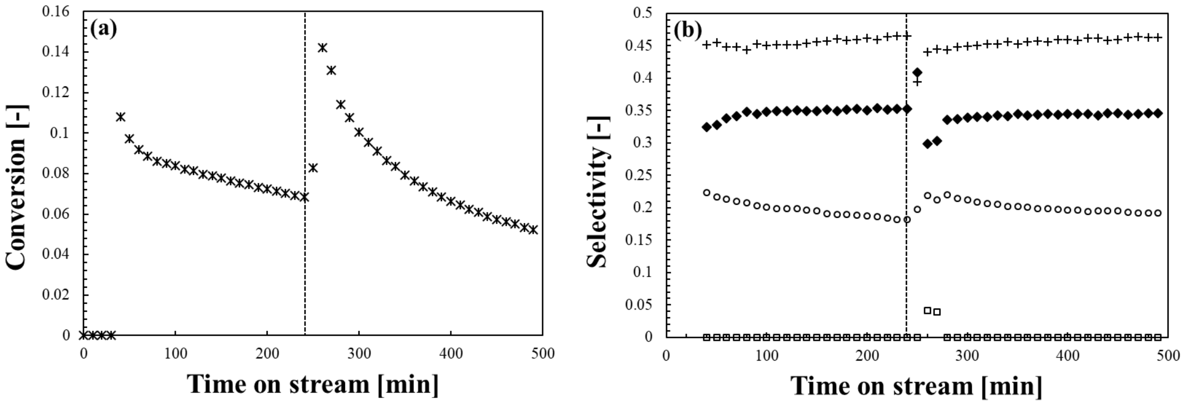

Figure 4.10. Representative time-on-stream: (a) conversion of *o*-xylene and (b) selectivities of products (♦: toluene, □: *p*-xylene, ○: *m*-xylene, +: 1,2,4-trimethylbenzene) over 0.9 PW_{12}@NU-1000 at 523 K (before 240 min) and 573 K (after 240 min).

Solid-state ^{13}C CP MAS NMR spectrum (Figure 4.11) of the used catalyst after inert purge 573 K shows a resonance at 17.8 ppm consistent with a mobile Ar-$\underline{C}H_3$ remaining within the catalyst. This species was successfully extracted with CD_2Cl_2, identified, and quantified by solution ^1H NMR as approximately two *o*-xylene molecules per POM cluster (Figure 4.12). Thus, the decrease in rates may be due to a slow approach to a steady state when the POMs become saturated with strongly bound reactants. Rate laws will be fully developed in future investigations over these materials.

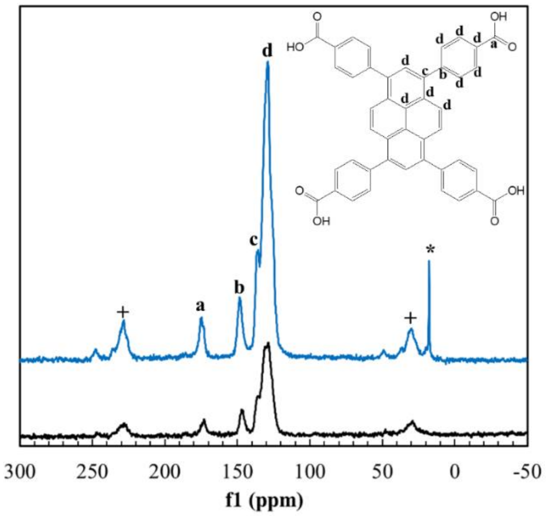

Figure 4.11. Solid-state ^{13}C CP MAS NMR spectra of 0.9 PW_{12}@NU-1000 as synthesized (black) and after catalysis (blue). + indicates spinning sidebands, * indicates new feature assigned as adsorbed $(C_6H_4)(CH_3)_2$.

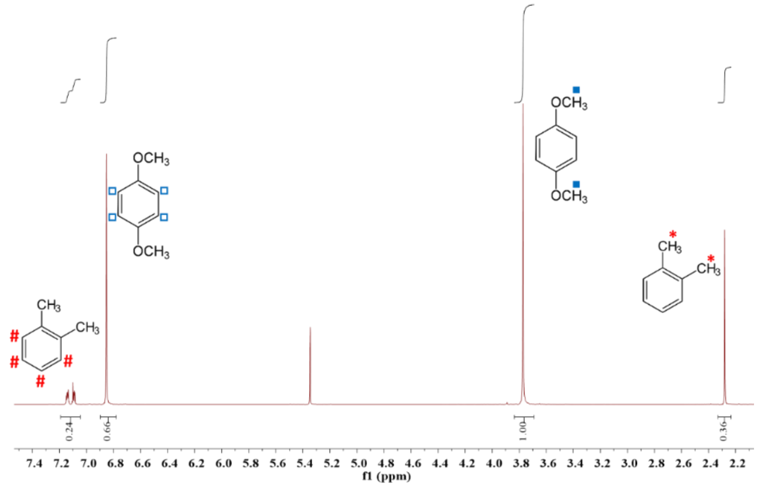

Figure 4.12. ^{1}H NMR spectrum of extract from used 0.9 PW_{12}@NU-1000. Deuterated dichloromethane and dimethoxybenzene were used as an extracting solvent and an internal standard, respectively. Extraction was performed at ambient temperature, and spectrum was taken after 24 h of extraction.

In addition to differences in rates, the catalysts promote different reaction pathways. Scheme 4.1 shows two representative *o*-xylene reaction pathways that different materials can promote. In the intramolecular isomerization pathway,[119] *o*-xylene is protonated at a Brønsted acid site. Then, a methyl group can shift from *ortho* to *meta* and further to *para*. At the low conversions used in these experiments, the selectivity to *p*-xylene is expected to be low, since two methyl shifts would be required before desorption from the active site. The experimental absence of *p*-xylene in these experiments also rules out direct *ortho* to *para* transitions that have been proposed for an intermolecular pathway[162] or from an extremely active catalyst.[163] In the intermolecular mechanism, two reactant molecules disproportionate to yield toluene and trimethylbenzene. The experiments strongly favor 1,2,4-trimethylbenzene over formation of 1,2,3-trimethylbenzene, as consistent with previous studies.[120, 164] Given the low conversion, the essentially zero yield of 1,3,5-trimethylbenzene is also expected. The disproportionation reaction is favored in materials with two adjacent active sites to accommodate migration of the proton from one ring to another. This mechanism has been reported to occur primarily in highly porous materials such as zeolites with relatively large channels (FAU, MOR, ZSM-12), where the xylene species are present in high local concentration.[118-119] Min et al. experimentally verified the formation of the diphenylmethane-based intermediate in zeolites that have large cavities or channels, and showed up to 99% disproportionation selectivity in such materials.[165]

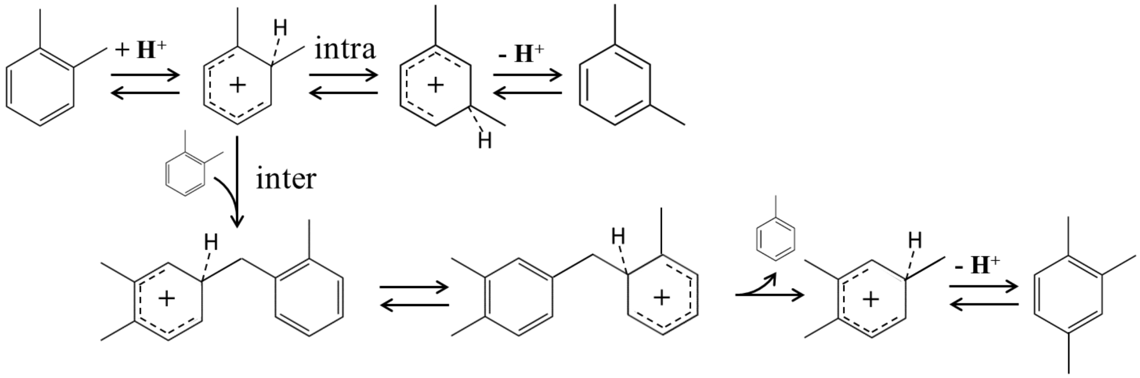

Scheme 4.1. *o*-xylene reaction pathways: intramolecular isomerization and intermolecular disproportionation.

The WO_x-ZrO_2 reference exhibits the typical behavior for this catalyst,[126] with 100 % selectivity toward the isomerization pathway in differential conversion regime. In contrast, the product selectivity over 0.9 PW_{12}@NU1000 shows primarily *o*-xylene disproportionation, where 83% of the product consists of a near equimolar mixture of toluene and trimethylbenzene, with the remaining minority product being *m*-xylene. The high selectivity to the disproportionation products and the apparent strong chemisorption of *o*-xylene leads to the proposed catalyst structure of Figure 4.13. In this hypothesized structure for the working state of the catalyst, the POM is electrostatically bound to the node[148, 166-167] *via* one of the three H^+ of the POM. Recently, our team demonstrated via a crystallographic method that HPA and Zr_6 node are close in proximity[168] to be able to form a hydrogen bond. Here, we hypothesize the hydrogen bond between one hydrogen of POM and oxygen of Zr_6 node as activated. In addition, we propose structure as right part of Figure 4.13 at reaction temperature, weakened hydrogen bond due to thermal energy. The remaining two H^+ lead to two chemisorbed *o*-xylene per POM, as seen in the extracted solution after catalysis

(Figure 4.12). The chemisorption of *o*-xylene may be unusually strong because of the additional stabilizing influence of the MOF aromatic ligands, especially given the PXRD pattern evidence that the POM is likely found within the small triangular channels. We hypothesize that the location of the POM within the MOF structure provides unique environments for the two reaction pathways. The space between the POM and an adjacent linker (in the ab plane) only provides room for a single *o*-xylene (marked in orange in Figure 4.13), which could promote the isomerization pathway. In contrast, the triangular channels (above and below POMs along the c-axis) and the lateral cavities (between the two adjacent Zr_6 nodes along the c-axis) appear to be appropriately sized for the intermediate of the disproportionation pathway (trimethylated diphenylmethane, marked with purple in Figure 4.13). These triangular channels are 1.2 nm, comparable to those of a large-pore acid zeolite, in which disproportionation is known to occur.[165]

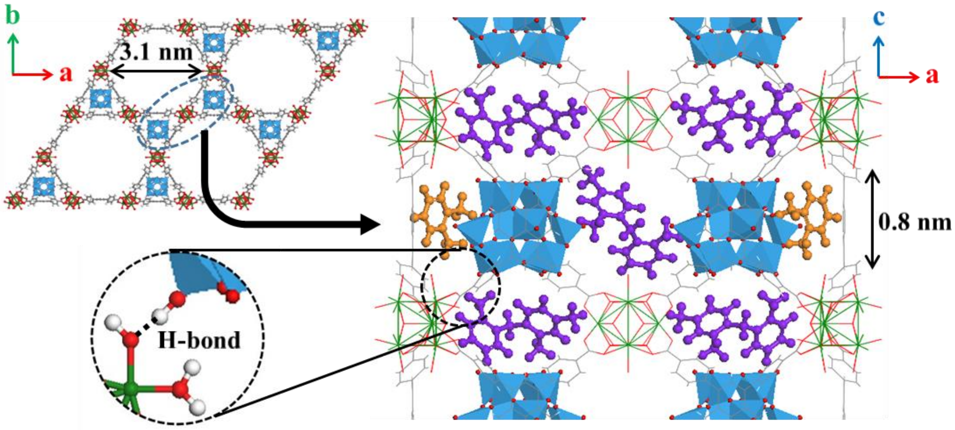

Figure 4.13. Proposed structure of PW_{12}@NU-1000. Color coded for potential reaction sites for isomerization (orange) and disproportionation (purple) under reaction conditions (right) and proposed hydrogen bond interaction under ambient condition (left bottom dotted circle). Dark green=Zr, Blue prisms=WO_5, red=O, gray=C, white=H

4.4 Conclusions

The Keggin POM of phosphotungstic acid was encapsulated in NU-1000 (PW_{12}@NU-1000), and this catalyst was shown to be active for the benchmark strong acid-catalyzed reaction of *o*-xylene isomerization/disproportionation at 523K. While MOFs display stable activities for many reactions, researchers have predominantly used MOFs as precursor, i.e. with deliberate decomposition of the framework,[139, 169-171] for use under aggressive conditions. This work demonstrates that MOF-supported catalysts can be structurally-stable during C-C skeletal rearrangement reactions that have been widely used in industrial and academic investigations of porous solid acids, but never previously in MOFs. Indeed, maximal loading of ~1 Keggin unit per unit cell of NU-1000 appears to stabilize structures of both the PTA and NU-1000; lower loadings of PTA immediately lost all structural integrity under reaction conditions. Furthermore, WO_x installed by other methods, such as impregnation of tungsten amido complexes, gives isolated WO_x sites that are unreactive for this reaction. Finally, the structurally-stable PW_{12}@NU-1000 catalyst shows strongly atypical selectivity toward disproportionation, which likely results from the particular pore structure of MOF support in which two Keggin units are stabilized in close proximity in the smaller (but still large relative to an aluminosilicate zeolite) side channels of the MOF. In the future, we expect that the tunable pore structure of MOFs via synthesis with different linkers will lead to new opportunities for controlling reaction pathway selectivity by placing the PTA in different pore environments or at different local densities. This control might enable a level of reaction network tuning which is not readily accessible with conventional oxide materials.

Chapter 5. Conclusions

This dissertation seekd to develop synthesis-structure-activity relationships for NU-1000-supported metal oxide catalysts as well-defined analogs to conventional supported catalysts. To this end, I presented three aims as follow:

I. Explore synthesis-structure-activity relationships for Nb-NU-1000 catalysts in the condensed-phase cyclohexene epoxidation.
II. Expand relationships developed in I in the vapor-phase cyclohexene epoxidation.
III. Study synthesis-structure-activity relationships for W-NU-1000 catalysts in *o*-xylene isomerization and disproportionation.

The first objective was met in Chapter 2. We presented the grafting of Nb oxide sites onto the nodes of the Zr-based metal–organic framework (MOF) NU-1000 as a stable, well-defined catalyst support. Nb oxide was deposited with loadings up to 1.6 mmol/g via two post-synthetic methods: atomic layer deposition in a MOF (AIM), and solution-phase grafting in a MOF (SIM). Difference envelope density (DED) measurements indicated that the two synthetic methods result in different local structures of the Nb ions within NU-1000. Despite their high Nb loadings, which are equivalent to > 60 % surface coverage, nearly all the Nb oxide sites of the MOF-supported catalysts are active for alkene epoxidation, as confirmed by phenylphosphonic acid (PPA) titration. The NU-1000-supported catalysts are more selective than the control Nb-ZrO_2 catalyst for cyclohexene epoxidation with aqueous H_2O_2, and they are far more active on a gravimetric basis.

The second objective was almost completely addressed in Chapter 3. In pursuit of studying H_2O_2 activation in the vapor phase, we built a vapor-phase hydrogen peroxide reactor. We studied epoxidation of cyclohexene with low-water H_2O_2 and in the absence of external solvent as a model system to understand direct/radical activation of H_2O_2 in the vapor-phase. We compared the behavior of Lewis acid catalysts, which are Ti and Nb grafted on a conventional support (SiO_2) and on an unconventional support (NU-1000). M-SiO_2 catalysts do not yield any conceivable radical derived products but only yield direct products (epoxide and diol), whereas M-NU-1000 catalysts produce radical species (cyclohexenol, cyclohexenone, and CO_2). In particular, Nb-NU-1000 shows similar direct pathway selectivity with our observation in condensed-phase study. Based upon the results of cyclohexene vapor adsorption, the presence of radical products over M-NU-1000 may be attributed to higher reactant population than over M-SiO_2. Such population could result in more chances for radicals to react further with neighboring reactants. Moreover, the absence of an external solvent could potentially lead to difference of intrinsic barriers between vapor- and condensed-phases.

The third objective was successfully addressed in Chapter 4. We investigated the use of phosphotungstic acid (PTA) encapsulated within NU-1000 as a catalyst for *o*-xylene isomerization and disproportionation at 523 and 573 K. Extended X-ray absorption fine structure (EXAFS), ^{31}P NMR, N_2 physisorption, and XRD showed that the catalyst is structurally-stable with time-on-stream, and that WO_x clusters are necessary for detectable rates, consistent with conventional catalysts for the reaction. PTA and framework stability under these aggressive conditions requires maximal loading of PTA within the NU-1000 framework; materials with lower PTA loading lost structural integrity under the reaction conditions. Initial reaction rates over the NU-1000-supported catalyst are comparable to a control WO_x-ZrO_2, but the NU-1000 composite material is unusually active towards the transmethylation pathway that requires two adjacent active sites in a confined pore, as created when PTA is confined in NU-1000.

In conclusion, all objectives are met to achieve the goal of this dissertation, which is the better understanding of NU-1000-supported metal oxide catalysts as well-defined analogs to conventional supported catalysts. The key findings of this work are expected to be broadly useful in understanding NU-1000-supported Lewis acid catalysts as well as to enable a level of reaction network tuning which is not readily accessible with conventional oxide materials.

Appendix A. Behavior of Iron-based MIL-100 in Cyclohexane Oxidation

This appendix presents a modified version of the following manuscript which I contributed equally:

Ah-Reum Kim,[+] Sol Ahn,[+] Tae-Ung Yoon, Justin M. Notestein, Omar K. Farha, and Youn-Sang Bae, *Manuscript in Preparation*, **2019**.

A.1. Introduction

Selective oxidation of sp^3 C-H bonds in saturated hydrocarbons under mild conditions is a challenging, yet promising area of inquiry.[172-174] Among many reactions, the oxidation of cyclohexane to mixtures of cyclohexanone and cyclohexanol (so-called KA-oil) is of great importance because it is an intermediate in the production of nylon-6 and nylon-66.[175-176] Generally, cyclohexane oxidation operates at O_2 pressures of 1-2 MPa and temperatures of 413-433 K to activate relatively inert C-H bonds.[177] However, under such conditions, it is generally difficult to achieve high conversion, high selectivity, and low side product yield at the same time due to higher reactivity of the product alcohols and ketones than that of the reactant.[178] Therefore, it is a grand challenge to design materials effective for selective oxidation under mild reaction conditions that could be mated with other processes to achieve high conversion and selectivity.

Over recent decades, all manner of catalysts have been reported for cyclohexane oxidation; carbon materials,[179-180] polymers,[181] silica,[182] and zeolites.[183] Metal-incorporated zeolites[173] and silica[176, 184] are some of the most promising catalysts. For example, Co-ZSM-5 and V-MCM-48, are active for cyclohexane oxidation with O_2 and H_2O_2, respectively.[173, 184] However, both these reports demonstrated a common problem, which is active metal leaching from the support under reaction conditions. Here, we hypothesize that single metal sites fully incorporated into the support can circumvent this leaching issue.

Metal-organic frameworks (MOFs) have attracted considerable attention as an intriguing type of inorganic-organic hybrid functional materials that are self-assembled from metal clusters and organic linkers.[185-187] Owing to their characteristic properties of large surface area, exceptional porosity and tunable pore structure, MOFs have shown potential applications for gas separation,[188-190] gas and vapor storage,[191-193] catalysis,[53, 194] and so on. Among these, MIL-100(Fe) is a promising material due to its hydrothermal stability, high surface area and two sets of mesoporous cages (29 and 25 Å) which have accessible microporous windows (9 and 5 Å, respectively).[195] Moreover, MIL-100(Fe) is based on reducible μ_3–oxo-centered trimers of Fe(III) octahedra, which can generate open Fe(II/III) sites through removing terminal solvent molecules (Scheme A.1).[196] Recently, iron-based MOFs have been studied in various catalysis applications,[197] but have been very few reports on Fe-based MOFs for cyclohexane oxidation reaction with organic peroxide as an oxidant.[198-199]

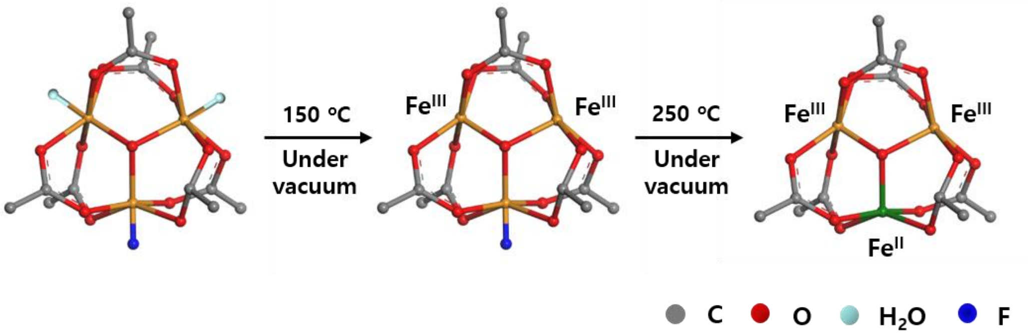

Scheme A.1. The formation of Fe CUSs in MIL-100(Fe).

In this study, we examine the oxidation of cyclohexane over Fe species in the mesoporous, metal-organic framework MIL-100(Fe). The performance of Fe-based MIL-100 was evaluated with hydrogen peroxide as an oxidant under mild conditions. We specifically investigated the influence of the oxidation state of Fe, which can be tuned by the aggressiveness of the pre-treatment.

A.2 Experimental Methods

A.2.1 Materials

1,3,5-Benzenetricarboxylic acid (≥ 98 %), iron powder (≥ 99 %), silver powder (-120 mesh, 99.999 %) and triphenylphosphine (99 %) were obtained from Alfa Aesar. Ammonium fluoride (≥ 98 %), cyclohexane (≥ 99.7 %), hydrogen peroxide (30 wt.%), 1,2-dichlorobenzene (≥ 99 %) and iron (II,III) oxide (Fe_3O_4, 99.99 %) were provided by Sigma-Aldrich. Nitric acid (≥ 60 %), ethanol (≥ 99.5 %) and acetonitrile (≥ 99.5 %) were obtained from Daejung chemical CO., Korea. Hydrofluoric acid (48-51 %) was purchased from JT Baker, Avantor Materials, PA, USA. Iron (III) oxide (Fe_2O_3, 99.999 %) was obtained from Strem Chemicals Inc.

A.2.2 Preparation of MIL-100(Fe)

MIL-100(Fe) was prepared by a hydrothermal synthesis according to previous protocols in the literature.[195, 200] The molar composition was 1.0 Fe^0, 0.67 1,3,5-BTC (1,3,5-benzene tricarboxylic acid), 0.6 HNO_3, 2.0 HF, and 277 H_2O. The reaction mixture was stirred at room temperature for 30 min, and then the solution was heated up to 160 °C for 12 h. The resulting orange solid was filtered and washed with hot water (80 °C) and hot ethanol (60 °C) until no colored impurities were detected in the mother liquor solution. To purify further, the powder was immersed in 38 mM aqueous NH_4F solution at 75 °C for 3h. The purified as-synthesized MIL-100(Fe) was dried at 60 °C for 12 h in a convection oven.

A.2.3 Activity Studies

Cyclohexane (11 mmol, 1.2 mL), 1,2-dichlorobenzene (215 μL, internal standard), and acetonitrile (9 mL, solvent) were introduced into a 20 mL screw cap vial. Subsequently, 80 mg activated MIL-100(Fe) (0.3 mmol with respect to Fe atom) was added to the solution, and the mixture was heated at 65 °C with stirring for 30 min. 4.0 M hydrogen peroxide in acetonitrile (1.1 mmol, 270 μL) was then added to initiate the reaction. This hydrogen peroxide solution was made by diluting aqueous hydrogen peroxide (5 mL, 30 wt.%) in 10 mL acetonitrile, followed by drying with anhydrous $MgSO_4$ [194] and the slurry was separated by centrifugation. The amount of MIL-100(Fe) was adjusted to the following molar ratio, Fe atom : H_2O_2 : cyclohexane = 1 : 3.6 : 36.

Two aliquots (0.2 mL) were removed at each time point by syringe filter and collected in gas chromatography (GC) sampling vials containing silver powder to decompose residual H_2O_2 and prevent further oxidation. Following a method developed by Shul'pin [201-202], excess triphenylphosphine (PPh_3) was added into one vial prior to GC analysis to convert any cyclohexyl hydroperoxide to the corresponding alcohol (cyclohexanol). Comparison of the product distributions with and without added PPh_3 gives the true composition of the reaction solution at that time point. Blank experiments without either material showed no cyclohexane oxidation products. Products were identified using GC (Agilent, HP 6890 equipped with a HP-INNOWAX capillary column and flame ionization detector; FID).

A.2.4 Characterization Methods

Scanning electron microscopy (SEM) was performed on an S-4800 FE-SEM (Hitachi, Japan). Powder X-ray diffraction (PXRD) patterns were recorded with a STOE-STADI MP with Cu Kα X-ray radiation at 40 kV and 40 mA. Diffraction patterns were measured with a scan step size of 0.02° per step. X-ray photoelectron spectroscopy (XPS) data were measured using a K-Alpha XPS spectrometer (Thermo, U.K.) equipped with a monochromated Al X-ray source (Al Kα line: 1486.6 eV). Inductively coupled plasma-optical emission spectroscopy (ICP-OES) was performed on an iCAP 7600 (Thermo Scientific, USA).

Adsorption and desorption isotherms of N_2 were obtained at 77 K by a 3Flex analyzer (Micromeritics Instruments, USA). Pore size distributions were determined by the DFT calculation method. Before the N_2 isotherm experiments, MIL-100(Fe) samples were evacuated to remove water and remaining organic molecules for 12 h at 150 ºC and at 250 ºC separately with the intent to yield different Fe CUS. Iron oxide samples (Fe_2O_3, Fe_3O_4) were degassed for 6 h at 100 ºC. Specific surface areas were calculated using the Brunauer-Emmett-Teller (BET) method in the linear range (0.03-0.2 P/P_0), as determined using the consistency criteria [203]. The total pore volume was determined from the amount of N_2 adsorption at $P/P_0=0.99$. Adsorption isotherms of CO at 25 ºC were measured using a Tristar 3020 instrument (Micromeritics Instruments, USA) augmented with a specially designed air circulation system (Protech Korea Instruments, Korea) for maintaining constant temperature.

A.3. Results and Discussion

A.3.1. Characterization

MIL-100(Fe) was synthesized using a hydrothermal method at 160 ºC for 12 h and subsequently purified by water, ethanol and an NH_4F solution. According to SEM images (Figure A.1), the synthesized material consists of uniform octahedral crystals without any other amorphous phases. The MIL-100(Fe) was activated at 150 ºC and at 250 ºC separately for 12 h and denoted MIL-100(Fe)-1 and MIL-100(Fe)-2, respectively. As shown in Figure A.2, all diffraction peaks of the as-prepared materials correspond to those of simulated MIL-100(Fe), and no other crystalline phases were detected. The textural properties of the MIL-100(Fe) were explored by N_2 adsorption-desorption and ICP-OES; the results are summarized in Table A.1. Both samples have typical type-IV isotherms with two steps, (Figure A.3) indicating that the materials retained their mesoporous structure after degassing. MIL-100(Fe)-1 exhibits a high surface area (2,010 m^2/g), large pore volume (0.83 cc/g), and corresponding pore size distribution (Figure A.4) in agreement with previous reports [196, 204]. MIL-100(Fe)-2 had increased surface area (2,260 m^2/g) and pore volume (0.99 cc/g), consistent with removal of the F^- anion from the terminal position of the Fe octahedra while retaining the long-range order of the material.

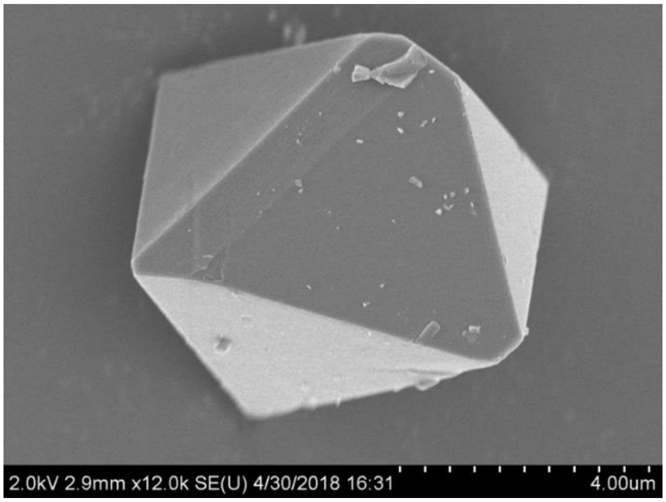

Figure A.1. SEM image of as-synthesized MIL-100(Fe).

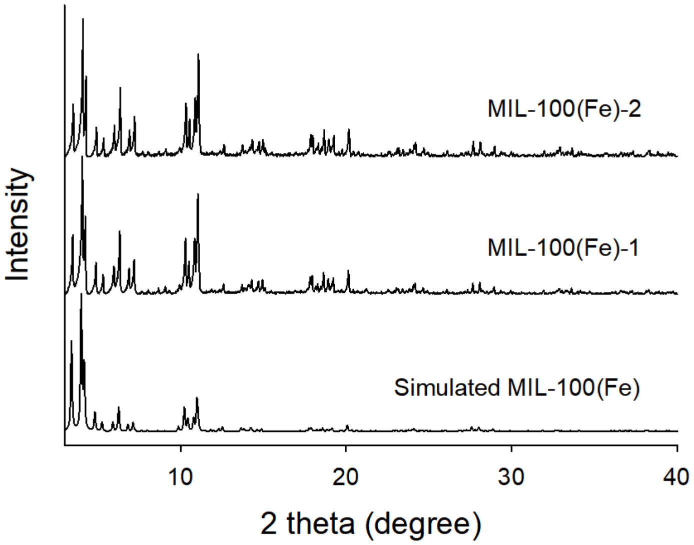

Figure A.2. Powder XRD patterns of the MIL-100(Fe) materials.

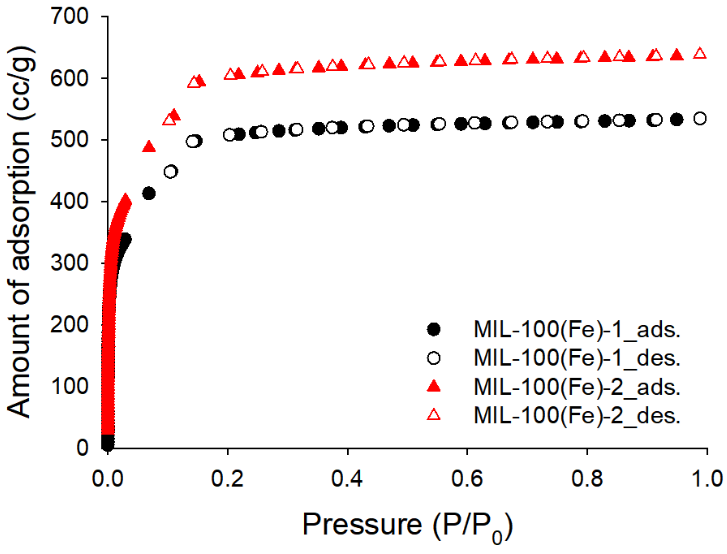

Figure A.3. N_2 adsorption-desorption isotherms following activation at 150 °C (MIL-100(Fe)-1) and 250 °C (MIL-100(Fe)-2).

Table A.1. Textural properties of MIL-100(Fe)-1 and MIL-100(Fe)-2.

	BET Surface area (m^2/g)	Total pore volume (cm^3/g)
MIL-100(Fe)-1	2,010	0.83
MIL-100(Fe)-2	2,260	0.99

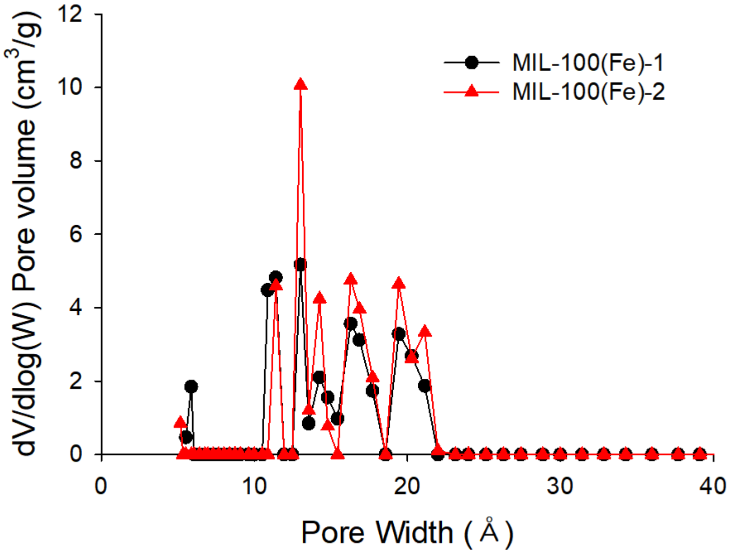

Figure A.4. Pore size distributions of MIL-100(Fe)-1 and MIL-100(Fe)-2 calculated by the DFT method.

The surface chemical states of MIL-100(Fe) were examined by XPS analysis. The survey spectra (Table A.2) show the expected existence of C, F, Fe and O in the MIL-100(Fe). MIL-100(Fe)-1 has a surface atomic composition of C, F, Fe and O = 63.2/4.2/9.9/22.7, while MIL-100(Fe)-2 has a composition of C, F, Fe and O = 64.4/0.7/10.8/24.1, demonstrating the significant removal of F^- anions from the Fe octahedra by the 250 °C treatment under vacuum. The dependence of iron oxidation state on activation temperature was also analyzed by XPS. The Fe 2p spectrum of MIL-100(Fe)-1 (Figure A.5) shows a binding energy of 711.9 eV characteristic of Fe(III). MIL-100(Fe)-2 shows an additional small peak at 710.4 eV assignable to Fe(II) [205-206]. These results demonstrated that iron-based, mesoporous, MIL-100 can generate CUS of mixed valence Fe(II)/Fe(III) by activation at 250 °C. The ratio of Fe(II):Fe(III) obtained from XPS spectra in MIL-100(Fe)-2 was 22:78, similar to the previously reported result [195]. Combining these results with ICP gives quantities of Fe(II) and Fe(III) sites in MIL-100(Fe)-2 at 0.8 and 3.0 mmol/g, respectively. We further measured pure isotherms of carbon monoxide (CO) at 25 ºC to confirm the presence of Fe(II) metal sites (Figure A.6). The adsorption capacity clearly increases when moving from MIL-100(Fe)-1 to MIL-100(Fe)-2, in accordance with the strong binding of CO to Fe(II) sties. The excess CO uptake from binding to Fe(II) sites is given by the x-intercept of the trend line from the MIL-100(Fe)-2 isotherm (Figure A.6). The value of ~0.8 mmol/g determined from this measurement is consistent with the result from XPS.

Table A.2. XPS analysis of MIL-100(Fe)-1 and MIL-100(Fe)-2.

Atomic %	C	F	Fe	O
MIL-100(Fe)-1	63.2	4.2	9.9	22.7
MIL-100(Fe)-2	64.4	0.7	10.8	24.1

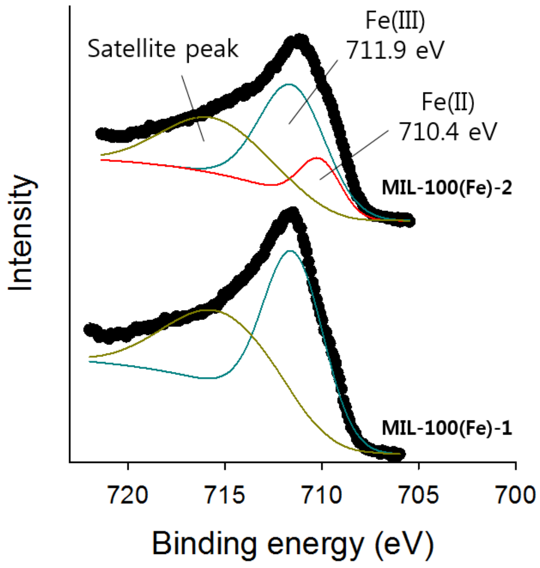

Figure A.5. Fe 2p XPS spectra of MIL-100(Fe)-1 and MIL-100(Fe)-2.

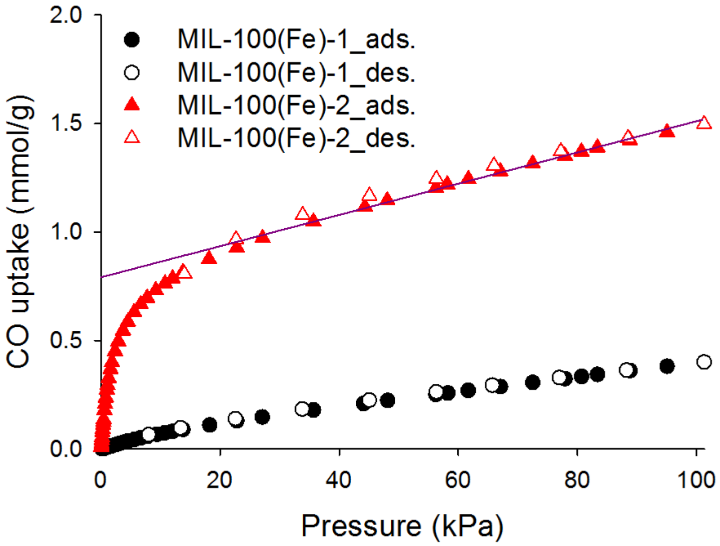

Figure A.6. Adsorption isotherms for carbon monoxide for MIL-100(Fe)-1 and MIL-100(Fe)-2 at 25 °C.

A.3.2. Activity

MIL-100 (Fe)-1 and MIL-100 (Fe)-2 were investigated for cyclohexane oxidation in liquid phase to compare their activities and identify potential reaction networks. The reaction was performed at 65 ºC, and acetonitrile was used as the reaction solvent, and hydrogen peroxide (H_2O_2) was used as the oxidizing agent. In cyclohexane oxidation, the main stable products are cyclohexanol (CyOH) and cyclohexanone (Cy=O). In many reaction networks, cyclohexyl hydroperoxide (CyOOH) is an unstable precursor to these two products. CyOOH thermally converts to CyOH and Cy=O in approximately equal amounts, and is thus not detected by GC instruments due to the high temperature injection step. To estimate the amount of CyOOH present in the reactor, PPh_3 was added into one reaction aliquot at each time point. PPh_3 decomposes CyOOH selectively to CyOH, so the amounts of CyOH, Cy=O and CyOOH actually present in the reaction system (Figure A.7) are calculated by following equations. Figure A.8 shows yields of oxidations over MIL-100(Fe)-1 and MIL-100(Fe)-2 both with and without PPh_3 to derive CyOOH yields.

$$[\mathrm{CyOOH}] = 2([\mathrm{CyOH}]_{\mathrm{PPh3}} - [\mathrm{CyOH}]_{\mathrm{no\ PPh3}})$$

$$[\mathrm{CyOH}] = [\mathrm{CyOH}]_{\mathrm{PPh3}} - [\mathrm{CyOOH}]$$

$$[\mathrm{Cy{=}O}] = [\mathrm{Cy{=}O}]_{\mathrm{PPh3}}$$

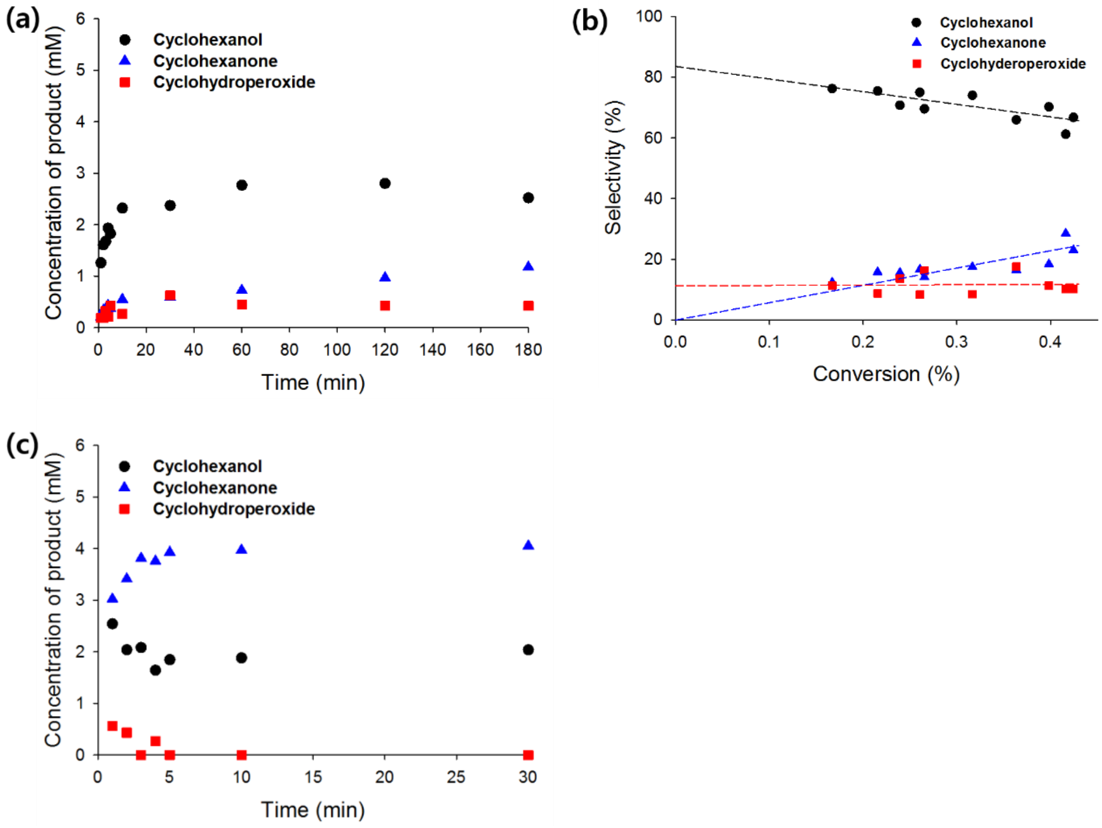

Figure A.7. Product yields vs. time for (a) MIL-100(Fe)-1 and (c) MIL-100(Fe)-2. Also, the selectivity vs conversion for (b) MIL-100(Fe)-1.

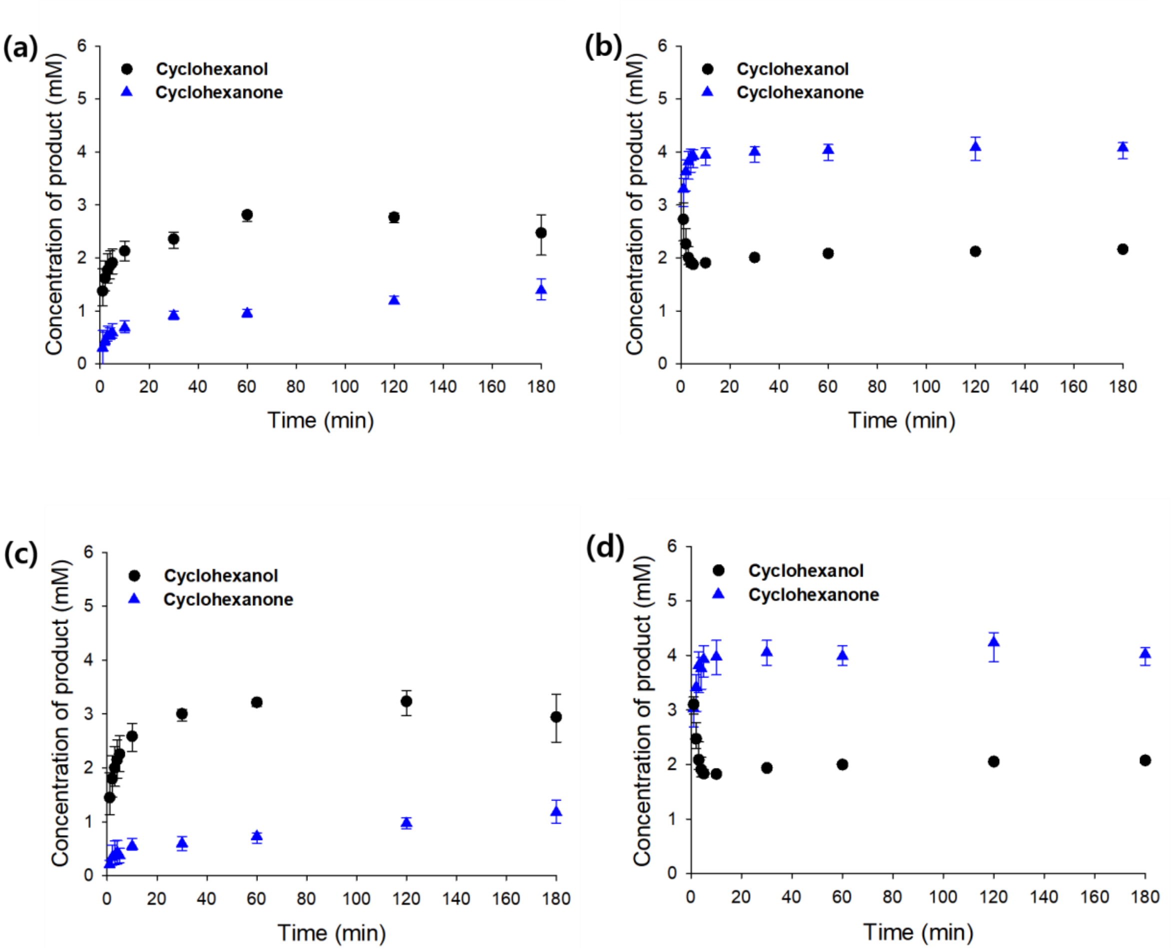

Figure A.8. Product yields vs. time without PPh_3 added for (a) MIL-100(Fe)-1 and (b) MIL-100(Fe)-2, and with PPh_3 added for (c) MIL-100(Fe)-1 and (d) MIL-100(Fe)-2.

In case of MIL-100(Fe)-1, CyOH, Cy=O, and CyOOH all form steadily over the first 10 minutes (Figure A.7 (a)), corresponding to an initial reaction rate (calculated between 1 to 3 min) of 0.006 $mol_{C6}.mol_{Fe}^{-1}.min^{-1}$ followed by a longer period of slow, continued oxidation. Over 3 h, 0.14 mol C_6 products are formed per mol of total Fe in MIL-100(Fe)-1. To shed further light on the possible reaction network, Figure A.7 (b) plots product selectivity against conversion. Figure A.7 (b) implies that CyOH and CyOOH are primary products (non-zero selectivity at zero conversion), while Cy=O is a secondary product (zero selectivity at zero conversion) for this catalyst. In contrast, MIL-100(Fe)-2 reaches its maximal conversion within 1 minute under these conditions (Figure A.7 (c)), corresponding to an initial reaction rate of at least 0.22 mol_{C6} mol_{Fe}^{-1} min^{-1}. Over the next 3 minutes, CyOOH and CyOH decrease while Cy=O increases to compensate. There is no further significant reaction after 3 minutes, but a total of 0.21 mol C_6 products are formed per mol of total Fe in MIL-100(Fe)-2. This corresponds well with the number of Fe(II) sites in this material. The rapid reaction precludes the same type of selectivity-conversion plot as for MIL-100(Fe)-1, but the selectivity change over the first 3 minutes also suggests that CyOOH and CyOH are primary products, whereas at least some of the Cy=O is formed as a secondary product.

The reaction mixture and used catalysts were examined for evidence of leaching of iron ions under reaction conditions. There was no significant Fe detected by ICP-OES in the reaction filtrate, and the crystallinity of MIL-100(Fe) was not significantly changed after cyclohexane oxidation reaction (Figure A.9).

The MIL-100(Fe) catalysts were also compared with bulk, crystalline Fe_2O_3 and Fe_3O_4. See Figure A.10, Figure A.11, and Table A.3 for characterization by PXRD and N_2 physisorption. Fe_2O_3 gave small amounts of product consistent with formation only of CyOOH in the reactor (Figure A.12). The mixed oxidation state Fe_3O_4 exhibits no catalytic activity for cyclohexane oxidation. The low relative reactivity of both these materials is presumably related to their much lower specific surface area – and the correspondingly low number of CUS available for reaction with H_2O_2 and CyOOH – as compared to that of the MIL-100(Fe) materials.

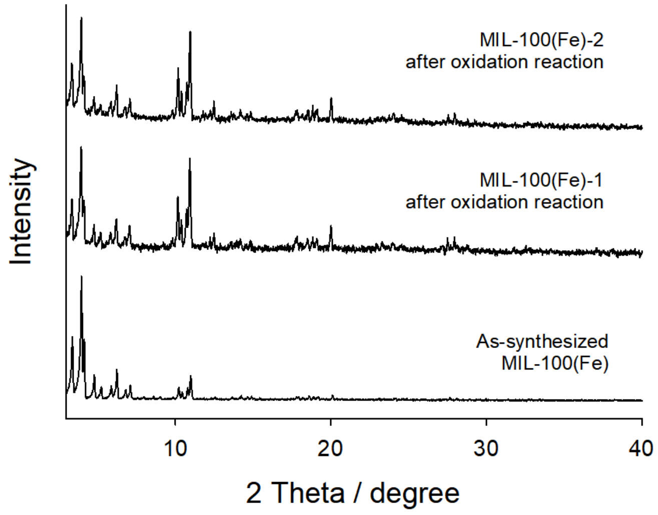

Figure A.9. Powder XRD patterns of the MIL-100(Fe) catalysts after cyclohexane oxidation. After oxidation, the solids were washed using hot acetonitrile solvent (65 °C) for 1 h and the powders were separated by centrifuge. The collected materials were dried in an oven (60 °C).

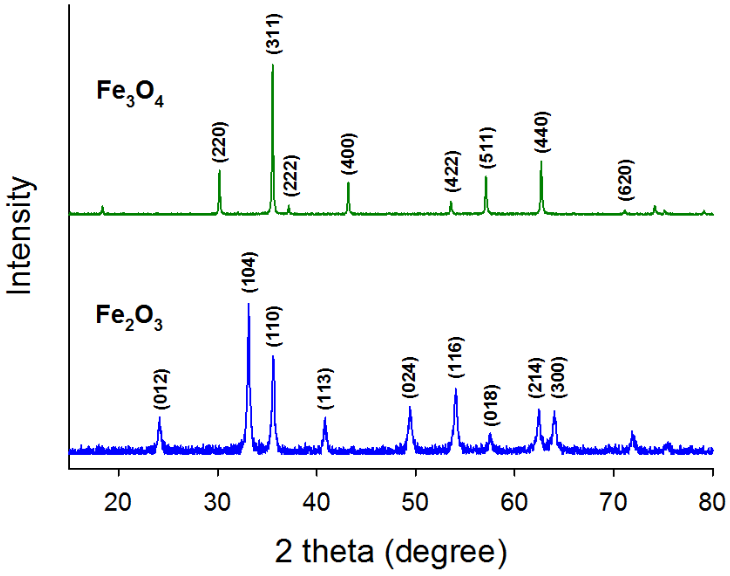

Figure A.10. Powder XRD patterns of Fe_2O_3 and Fe_3O_4.

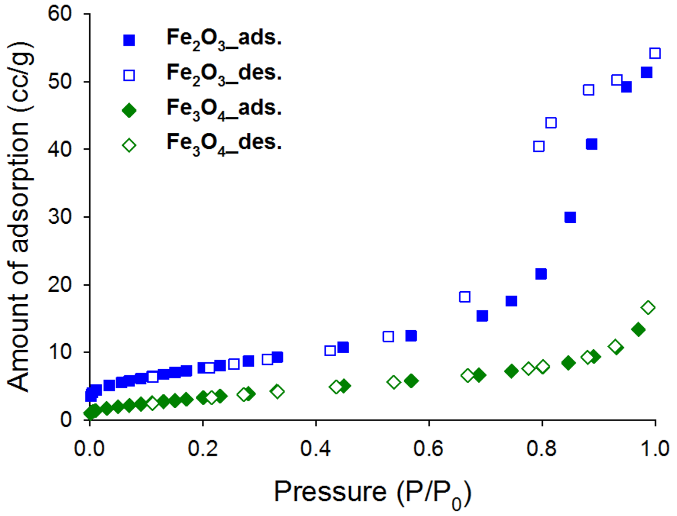

Figure A.11. N_2 adsorption-desorption isotherms of Fe_2O_3 and Fe_3O_4.

Table A.3. Textural properties of Fe_2O_3 and Fe_3O_4.

	BET Surface area (m^2/g)	Total pore volume (cm^3/g)	Fe content
Fe_2O_3	30 (27)	0.08	12.5 mmol/g
Fe_3O_4	10 (13)	0.03	13.0 mmol/g

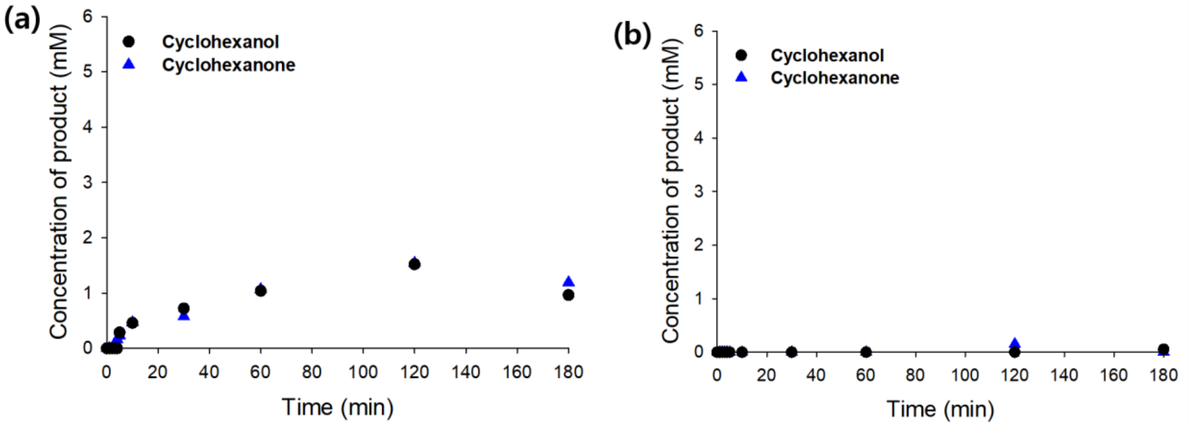

Figure A.12. The product yields vs time for cyclohexane oxidation at 65 ºC with (a) Fe_2O_3 and (b) Fe_3O_4. Reactions were run over the same Fe mol (0.304 mmol) as for the MIL-100(Fe) runs.

We propose a reasonable radical reaction network for cyclohexane oxidation (

Scheme A.2).[207] We reason that extremely rapid initial reaction of MIL-100(Fe)-2 is due to role of the Fe(II) coordinatively unsaturated sites initiating a radical oxidation cascade. First, H_2O_2 reacts with the Fe(II) sites in MIL-100(Fe)-2 to produce hydroxyl radicals[208] and oxidize the Fe(II) site to Fe(III) (Eq. (1)). H_2O_2 can also react with Fe(III) active sites in MIL-100(Fe) to ultimately generate HO· radicals, O_2, H_2O, and new Fe(II) sites, in accordance with the Haber-Weiss route (Eq. (2) and (3)). Importantly, Yang et al. reported that Eq. (1) proceeds faster than Eq. (2) by 3-4 orders of magnitude, which emphasize the importance of Fe(II) over Fe(III) in terms of radical generation.[209]

OH radicals react with cyclohexane, O_2, and additional H_2O_2 to generate the intermediate species CyOOH and more radicals that can continue to propagate (Eq. (4), (5), (6)). Over Fe(II) sites, the CyOOH will decompose rapidly to radicals that give CyOH and a Fe(III) site (Eq. (7)

and (8)). As for Eq. (1), Eq (7) is expected to be very rapid. In slower reactions, CyOH can be oxidized by OH radicals to give Cy=O (Eq. (9) and (10)). CyOOH is decomposed in several steps into approximately equal amounts of CyOH and Cy=O (Eq. (11)). This latter process can occur thermally, as in GC injectors, or over Fe(III) sites. Overall, the key difference between the two catalysts resides in the expected rapid production of OH radicals and decomposition of CyOOH over Fe(II) sites in MIL-100 (Fe)-2. This results in little CyOOH accumulating in the reaction system and rapid progression all the way to Cy=O (Eq. (7) and (10)). Otherwise, the oxidation reactions are initiated much slower over Fe(III) sites, and CyOOH and CyOH are able to accumulate.

$[Fe^{II}] + H_2O_2 \rightarrow HO\cdot + [Fe^{III}] + HO^-$ (1)

$[Fe^{III}] + H_2O_2 \rightarrow HOO\cdot + H^+ + [Fe^{II}]$ (2)

$HOO\cdot + H_2O_2 \rightarrow H_2O + HO\cdot + O_2$ (3)

$HO\cdot + CyH \rightarrow H_2O + Cy\cdot$ (4)

$Cy\cdot + O_2 \rightarrow CyOO\cdot$ (5)

$CyOO\cdot + H_2O_2 \rightarrow \mathbf{CyOOH} + HOO\cdot$ (6)

$\mathbf{CyOOH} + [Fe^{II}] \rightarrow CyO\cdot + HO^- + [Fe^{III}]$ (7)

$CyO\cdot + CyH \rightarrow \mathbf{CyOH} + Cy\cdot$ (8)

$\mathbf{CyOH} + HO\cdot \rightarrow CyO\cdot + H_2O$ (9)

$CyO\cdot + HO\cdot \rightarrow \mathbf{Cy{=}O} + H_2O$ (10)

$2\mathbf{CyOOH} \rightarrow \mathbf{CyOH} + \mathbf{Cy{=}O} + \frac{1}{2} O_2 + H_2O$ (11)

Scheme A.2. Proposed cyclohexane oxidation network. Adapted from Van-Dunem et. al.[210]

A.4. Conclusions

The Fe-based, mesoporous metal-organic framework, MIL-100(Fe), was synthesized by a one-pot solvothermal method. MIL-100(Fe) presents redox-active Fe(II)/Fe(III) sites whose composition and fraction of coordinatively-unsaturated sites depends on the activation temperature, without changing the long-range structure of the MOF. This work demonstrates that MIL-100(Fe) can oxidize cyclohexane in the presence of H_2O_2 under mild condition. MIL-100(Fe)-2 possesses Fe(II) sites and gives correspondingly much faster activity for cyclohexane oxidation than does MIL-100(Fe)-1 that only has Fe(III) sites. This is consistent with Haber-Weiss type of reaction networks where peroxide decomposition is very rapid in the presence of Fe(II). The large fraction of CUS in these materials also gives rise to much higher reactions rates than seen for the bulk iron oxides. Future work will focus on regenerating these materials and applying these concepts to other similar MOFs.

Appendix B. Comparison of Gas-phase and Liquid-phase Catalytic Epoxidation of Cyclohexene with Hydrogen Peroxide using Vanadium MIL-47

This appendix presents a modified version of the following manuscript which I contributed equally:

Tae-Ung Yoon+ Sol Ahn,+ Ah-Reum Kim, Justin M. Notestein, Omar K. Farha, and Youn-Sang Bae, *Manuscript in Preparation*, **2019**.

B.1 Introduction

Metal-organic frameworks (MOFs) are a class of crystalline porous solids that are promising new materials for many applications, especially those MOFs with good chemical and thermal stability.[211-212] The high, and often selective, sorption capacities of these materials make them candidate materials for various applications in gas separation, storage, sensing, capture and catalysis.[211, 213-215] Separately, alkene epoxidation is a challenging and important class of chemical reactions. For example, propylene oxide is one of the highest produced organic chemicals, at 3 million tons per year.[216-219] Catalytic liquid-phase epoxidation of cyclohexene is commercially important for the production of cyclohexene oxide, an essential intermediate in fine chemicals manufacture.[220-222] It is also a widely-used probe reaction. Although not generally practiced, gas-phase epoxidation would be highly desirable, as it would avoid common problems in condensed phase catalysis, such as large reactor volumes, leaching of the catalytic metal sites, or competition for the active site by coordinating solvents. Vapor phase operation also allows higher reaction temperatures, and thus higher reaction rates, without high-pressure operation.[223-225]

In this study, we have compared the catalytic activity of a V-containing MOF MIL-47(V) in the condensed and gas phase oxidation of cyclohexene. MIL-47(V) consists of corner-sharing vanadium (III) oxide octahedral chains connected by terephthalate linkers (Figure B.1). Catalytic studies on cyclohexene oxidation in MOFs have been published by several groups.[226-229] However, these studies have seen low reaction rates or problems with active site leaching, which motivates both the study of catalytic node MOFs like MIL-47(V), and the study of epoxidation in the gas phase. This research discusses the effect of temperature and reaction phase in cyclohexene epoxidation over this catalyst. Different mechanisms appear to dominate in the gas and condensed phases, which contributes to the different selectivities and rates that are observed.

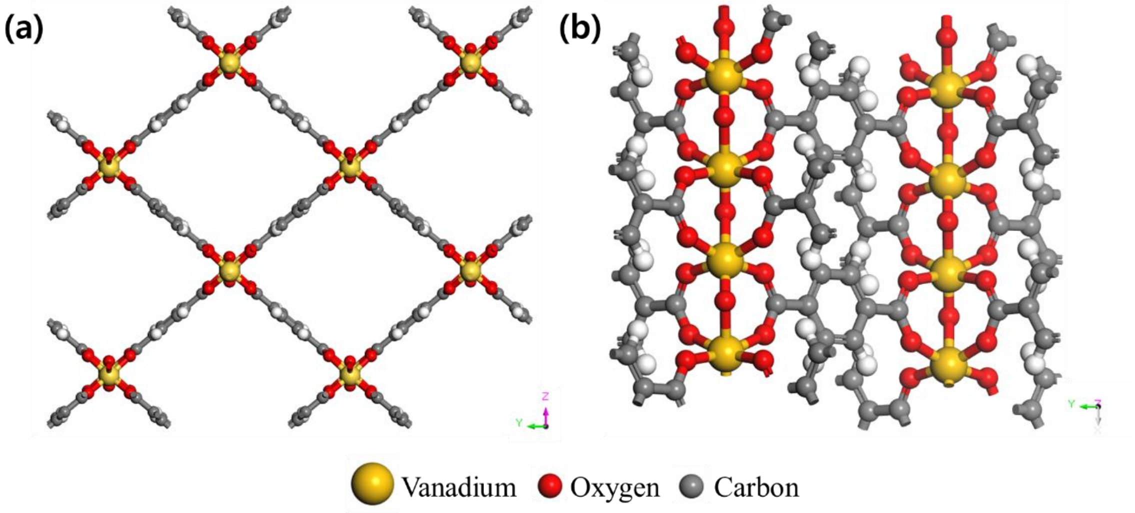

Figure B.1. Ball-and-stick representations of MIL-47(V) viewed along the crystallographic (a) x-axis and (b) z-axis, respectively. The former shows the V=O sites available for reaction, while the latter shows chains of V^{5+} cations that would be expected to be resistant to leaching.

B.2 Experimental Methods

B.2.1 Synthesis of Catalysts

The preparation of MIL-47(V) was carried out as previously reported.[230] Briefly, vanadium

(III) chloride (VCl_3; Sigma Aldrich, 97 %), terephthalic acid (TPA, C_6H_4-1,4-$(CO_2H)_2$; Sigma Aldrich, 98 %) and deionized water were mixed in the molar ratio of 1 V : 0.25 TPA : 100 H_2O. The reactants were introduced to a Teflon-lined steel autoclave, sealed and placed in a convection oven at 200 °C for 4 days. After that, excess TPA was removed by dispersing the powder in excess DMF for 10 min with stirring. Then, filtration was performed to recover the powder. After that, the resulting powder was placed in a Teflon-lined steel autoclave with DMF. This autoclave was placed in an oven at 150 °C for overnight to further purify the powder with hot DMF. Finally, the MOF suspension was cooled and filtered, and the MOF samples were heated overnight at 250 °C under an air atmosphere to remove DMF.

B.2.2 Characterization

Powder X-ray diffraction (PXRD) was performed using a STOE-STADI MP powder diffractometer operating at 40 kV voltage and 40 mA current with Cu-Kα X-ray radiation ($\lambda = 0.154056$ nm) in transmission geometry. Diffraction patterns were collected on the $3° < 2\theta < 50°$ in 0.02° steps at 5°/min scan speed.

Brunauer-Emmett-Teller (BET) surface areas were obtained from N_2 adsorption-desorption isotherms at 77 K, which were carried out on a Tristar II surface area and porosity analyzer (Micromeritics Instruments, USA). Before each N_2 isotherm experiments, the samples were activated at 150 °C for 15 h under vacuum. BET surface areas were calculated within the linear range determined by consistency criteria ($0.00079 < P/P_0 < 0.00512$).[231-232] Total pore volumes were estimated at $P/P_0 = 0.99$.

Inductively coupled plasma optical emission spectrometry (ICP-OES) was carried out using an iCAP 7600 (Thermo Scientific, USA). Vanadium (292.402, 309.311, 310.23, and 311.071 nm) contents were compared to the ICP standard solutions.

B.2.3 Liquid-phase Cyclohexene Epoxidation

Liquid-phase catalytic epoxidation was performed in 20 mL septum-cap glass vials vented with a needle. Cyclohexene (11 mmol, 1.1 mL, > 99 %, Sigma-Aldrich), and 1,2-dichlorobenzene as an internal standard (1.3 mmol, 150 μL, Sigma-Aldrich), were dissolved in acetonitrile (9 mL, Sigma-Aldrich), to which MIL-47(V) (6.7 mg, 29 μmol of vanadium) was added. After heating to 50 or 65 °C and shaking at 300 rpm for 1 h, the reaction was initiated with the addition of 4.0 M H_2O_2 in an acetonitrile solution (1.1 mmol, 270 μL). This H_2O_2 solution was prepared by diluting aqueous H_2O_2 (10 mL, 30 wt %, Sigma-Aldrich) in acetonitrile (20 mL), followed by drying over anhydrous $MgSO_4$ (7g, > 99 %, Sigma-Aldrich), which was then centrifuged and decanted. The initial molar ratio was cyclohexene : H_2O_2 : V = 400 : 40 : 1

Reaction aliquots were collected into gas chromatography (GC) sampling vials with silver powder (ca. 0.5 mg, > 99 %, Sigma-Aldrich) to quench unreacted H_2O_2. This prevents further oxidation of the reactant. Products from cyclohexene oxidation were identified and quantified using GC-FID (Shimadzu 2010 GC-FID, TR-1 capillary column) against calibrated standards. Carbon products observed in this reaction were cyclohexene oxide (epoxide), trans-1,2-cyclohexane diol (diol), 2-cyclohexen-1-one (cyclohexenone), and 2-cyclohexen-1-ol (cyclohexenol). For catalytic reactions, mass balances (products detected / reactant consumed) were ≥ 90 %.

A hot filtration was performed to test for catalyst leaching. Cyclohexene epoxidation was run for 15 min, then the reaction mixture was transferred using a syringe filter while the mixture remained stirring at temperature. The transferred sample was placed in a clean, heated 20 mL septum-cap vial, where the reaction continued as usual.

B.2.4 Gas-phase Cyclohexene Epoxidation

The gas-phase epoxidation kinetic studies were carried out in a custom-built catalytic reaction system. This system used a thermostatted quartz tube reactor, operated in a down-flow configuration. The fixed catalyst bed (47 mg, 0.078 mmol) was partially filled by a quartz wool plug. Hydrogen peroxide vapor was generated by feeding liquid H_2O_2 (same 4M H_2O_2 solution as mentioned above) with a syringe pump (0.1 mL/h, KDS 100, KD Scientific) equipped with a plastic syringe through a FEP (fluorinated ethylene propylene) capillary tube to the top of the reactor, where the liquid evaporated at the temperature (110 °C) of the upper reactor furnace. Cyclohexene vapor was delivered using He (7.5 mL/min, 99.999%, Airgas) as a reactant through a quartz bubbler with additional dilution by He (20 mL/min) at 25 °C and nominal ambient pressure (vapor pressure: 11.9 kPa). We adjusted the flowrates with mass flow controllers (Brooks Instruments). Cyclohexene (4 kPa) and H_2O_2 (1.3 kPa) were fed at a ratio of 3:1. Reaction products were separated by a HP-INNOWAX (50 m length, 0.2 mm diameter, 0.4 µm film) column and were identified and quantitated with a flame ionization detector (FID) mounted on a 7890 A GC (Agilent Technologies). Carbon products observed in this reaction were diol, cyclohexenone, cyclohexenol, and cyclohexanone.

B.3 Result and discussion

B.3.1 Catalyst Characterization

PXRD patterns of the as-synthesized samples (Figure B.2 (a)) match well with the simulated pattern,[230] and the material maintains its crystallinity after liquid-phase and gas-phase reactions. However, after gas-phase reaction, there is formation of a small amount of V_2O_5 as indicated by an asterisk (*). The BET surface area calculated from the nitrogen isotherm (1110 m^2/g, Figure B.2 (b)) agrees reasonably with the reported values (1050 m^2/g).[230, 233]

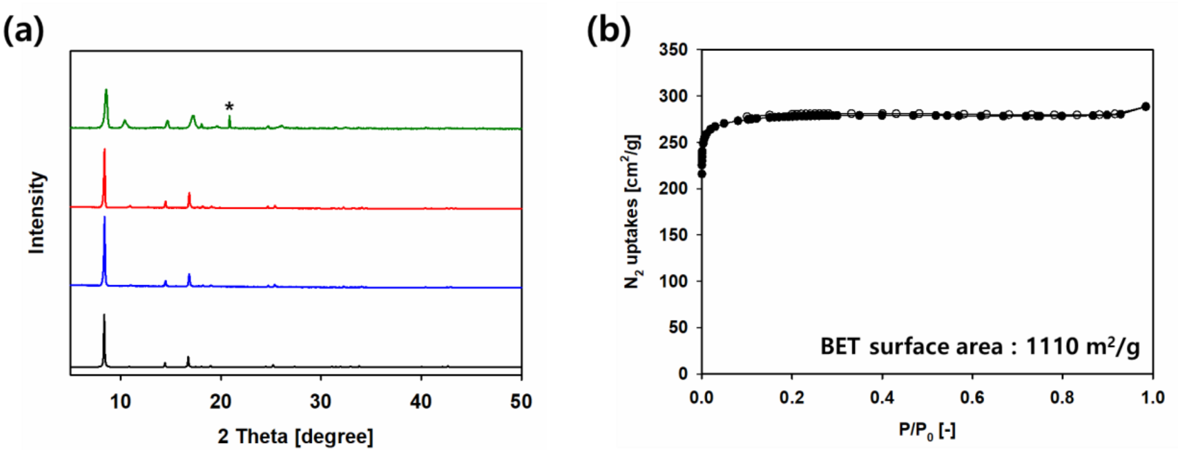

Figure B.2. (a) X-ray powder diffraction patterns of MIL-47(V) after being degassed at 150 °C, 15 h. (*: feature of V_2O_5) (b) N_2 adsorption-desorption isotherm at 77 K on MIL-47(V).

B.3.2 Liquid-phase epoxidation

Figure B.3 presents the detailed product distributions for MIL-47(V) catalyst as a function of reaction time at 65 ºC. Data at 50 ºC are found in Figure B.4 and are qualitatively similar. The liquid-phase reaction products formed are epoxide, diol, cyclohexenone, and cyclohexenol. Scheme B.1 illustrates the proposed reaction network for liquid-phase cyclohexene epoxidation, based on prior studies of cyclohexene epoxidation.[94-96]

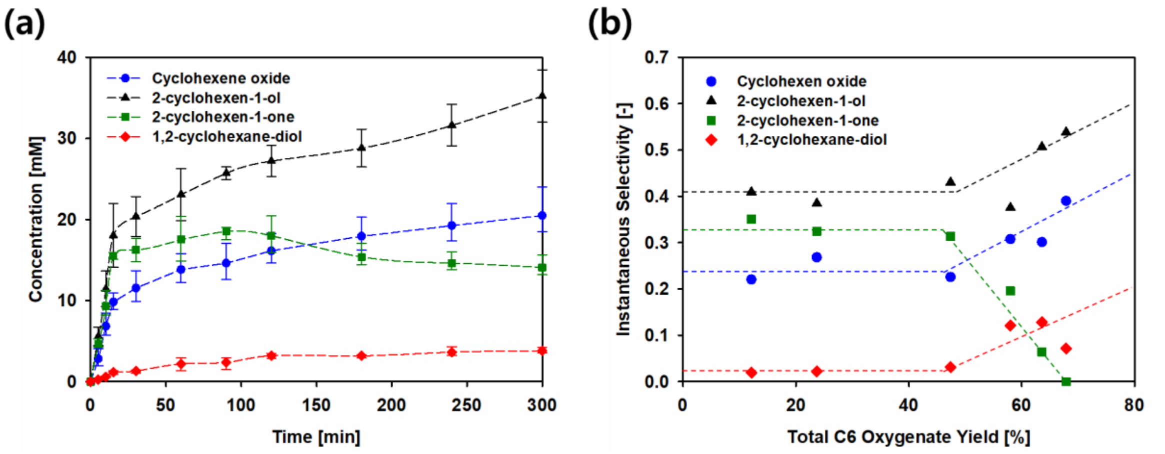

Figure B.3. (a) Product yields vs. time. (b) product instantaneous selectivity vs. conversion for liquid-phase cyclohexene epoxidation with MIL-47(V) at 65 °C. Instantaneous selectivity considers only the additional products formed between the prior time point and the current one. Lines are intended only as guides to the eye.

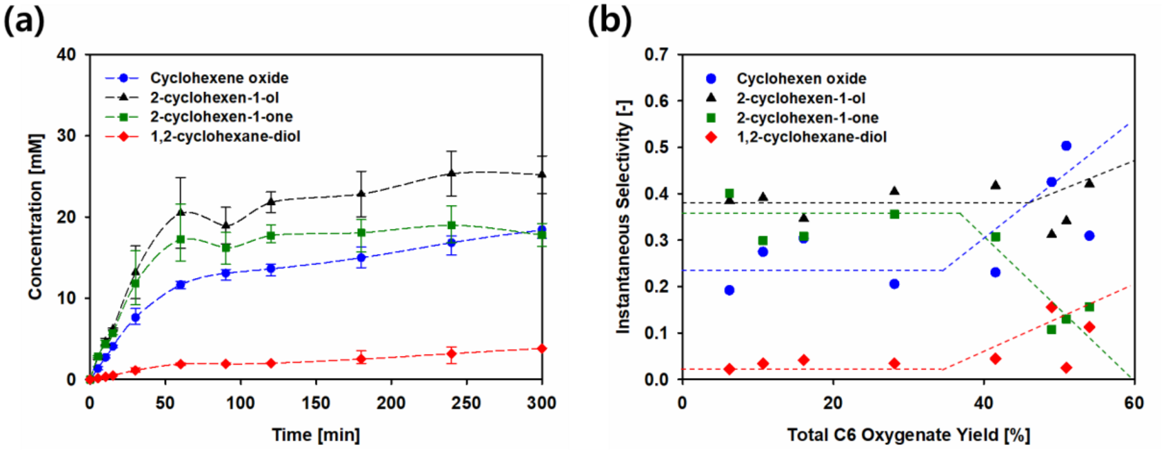

Figure B.4. (a) Product yields vs. time. (b) product instantaneous selectivity vs. conversion for liquid-phase cyclohexene epoxidation with MIL-47(V) at 50 °C.

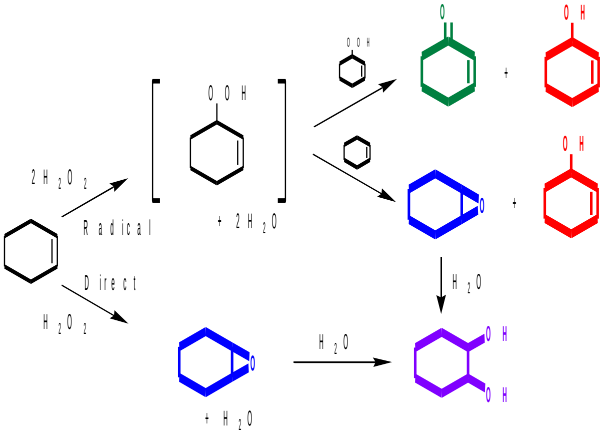

Scheme B.1. Proposed reaction network for liquid-phase cyclohexene oxidation. Cyclohexenyl hydroperoxide is not detected directly.

The initial turnover frequency (up to 15 min or ~ 50 % yield of C_6 oxygenates with respect to limiting H_2O_2) is 1.15 $mol_{C6}\ mol_V^{-1}min^{-1}$, Diol was observed initially at < 5 % selectivity. The low selectivity and the exclusive formation of the trans isomer is consistent with the diol being formed from the epoxide by hydrolysis. Figure B.3 (b) plots instantaneous selectivity against conversion. During this initial period, the production of cyclohexenol and cyclohexanone are high and similar. For this to be consistent with the reaction network in Scheme B.1, most of the radical-derived hydroperoxyl species must be undergoing bimolecular decomposition (top route) and not contributing to further formation of epoxide via the middle route of Scheme B.1. The ~ 25 % selectivity to epoxide must therefore be formed via the direct activation of H_2O_2 over the V sites.

In previous reports, the initial cyclohexene TOF of a highly dispersed V-SiO_2 was 0.94 $mol_{C6}\ mol_V^{-1}min^{-1}$ and cyclohexenol and cyclohexenone were dominant products, under similar conditions.[216] Therefore, MIL-47(V) shows comparable performance to a benchmark material, even though the structures of the two catalysts are quite dissimilar (e.g. isolated VO_x on silica vs.

extended V-O-V chains coordinated to carboxylates). .

For the data in Figure B.3 (a), rates decrease by more than 10-fold after the first 15 min (~ 50 % yield of C_6 oxygenates with respect to limiting H_2O_2) to a TOF of 0.04 mol_{c6} mol_v^{-1} min^{-1}. In addition, the selectivity to cyclohexenone drops rapidly, while the selectivity to cyclohexenol rises and becomes comparable to the sum of epoxide and diol. Therefore, at later times or conversion, it appears that the primary route of C_6 oxygenate formation is through the middle cyclohexenyl hydroperoxide radical route of Scheme B.1. Some of cyclohexenyl hydroperoxide species may be selectively decomposing to cyclohexenol as well. This is consistent with little to no H_2O_2 remaining in solution, and O_2 becoming the terminal oxidant.

To verify the heterogeneity of the catalytic reaction, a hot filtration experiment was performed. Leaching of active species during reaction is commonly observed for vanadium oxide-based catalysts.[216, 229, 234-238] However, our study found no evidence for leaching of an active species. As shown in Figure B.5, the reaction mixture containing MIL-47(V) was filtered at 15 min at 65 °C using a syringe filter, and no further product formation is detected over the next 3 h. Moreover, the ICP-OES measurements of the catalyst before and after reaction remains constant as 0.9 ± 0.1 vanadium ions per organic linker.

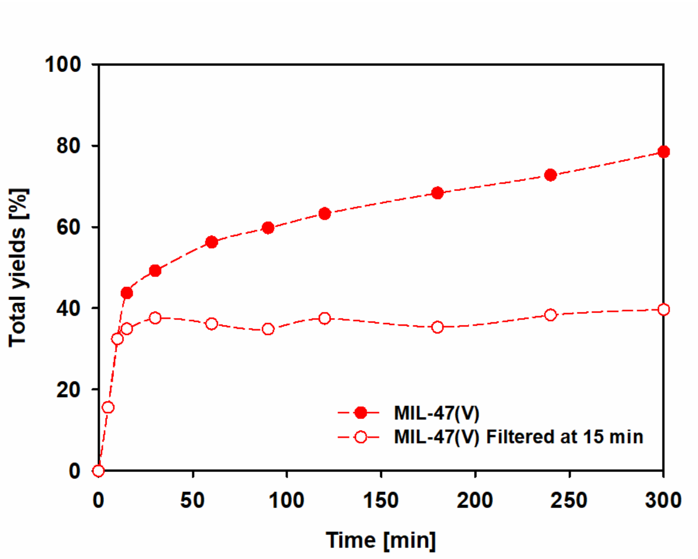

Figure B.5. Leaching test of MIL-47(V) of cyclohexene epoxidation at 65 °C.

B.3.3 Gas-phase epoxidation

Gas-phase epoxidation was performed at higher temperatures (120 and 150 °C), than the corresponding condensed-phase reaction. Figure B.6 shows the detailed product distributions for MIL-47(V) catalyst at 120 ºC. Data at 150 ºC are found in Figure B.7 and shows more selectivity toward cyclohexanone. However, the C_6 oxygenate production rates at 120 °C are 36 % higher than at 150 °C. This arises from increasing rates of unselective H_2O_2 decomposition in the framework at higher temperatures, which decreases the H_2O_2 concentration available for oxygenate formation. This has been observed in prior work.[239-240] At both temperatures, there is a relatively slow approach to steady reactor operation. Products take as much as 2 h time on stream (TOS) to become detectable in the reactor outlet. This is presumably due to the relatively low amounts of production and the strong affinity for some of the products (e.g. diol) to the catalyst surface in the absence of solvent. The yield of C_6 oxygenates (0.6 % with respect to limiting H_2O_2)

at steady conversion regime (> 800 min) is much lower than the yields achieved in condensed phase batch reactors, but this is expected from the much lower contact time in the flow reactor (1.1 s). Cyclohexenone and cyclohexenol formation rates reach a steady state in those first 3 hours TOS, but it takes nearly 800 min for the total production of C_6 oxygenates to stabilize.

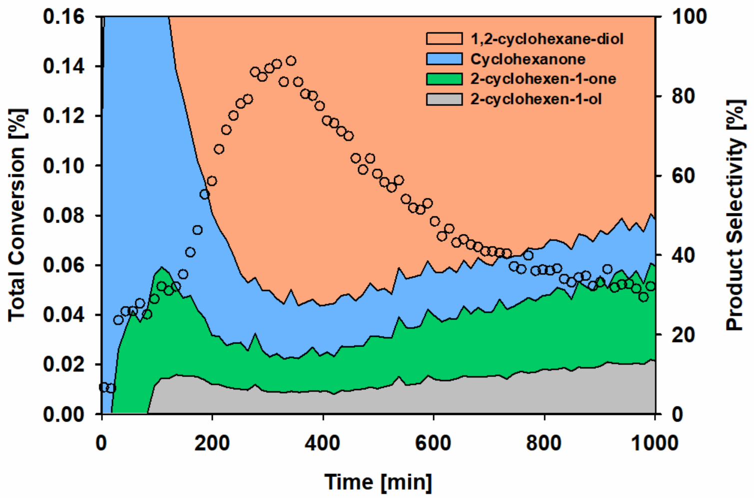

Figure B.6. Time-on-stream conversion and C_6 oxygenate selectivity profile of gas-phase cyclohexene epoxidation at 120 °C over MIL-47(V). The time required for product breakthrough is likely related to the affinity of the species for the MOF pore, with ketones being adsorbed less strongly than alcohols, which are absorbed less strongly than the diol.

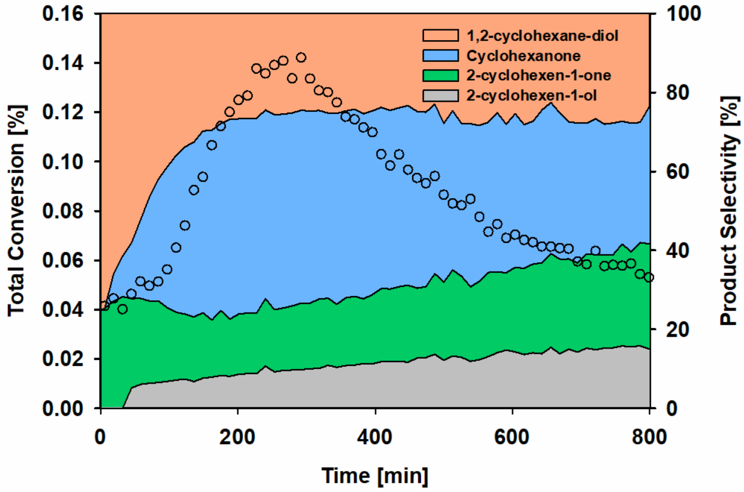

Figure B.7. Time-on- stream conversion and C_6 oxygenate selectivity profile of gas-phase cyclohexene epoxidation at 150 °C over MIL-47(V).

More significantly, the product distribution is also different in the two modes of operation. In the gas-phase flow reactor, no epoxide was observed, and at steady state (TOS > 800 min), diol is the dominant product at ~ 50% selectivity. As in the liquid phase, only the trans-diol product is observed, indicating that the diol is derived from the hydrolysis of cyclohexene epoxide. In control experiments, added epoxide and water are only partially hydrolyzed by an empty reactor, so over this catalyst, hydrolysis appears to be rapid compared to the initial epoxidation. This is specifically in contrast with previous gas-phase epoxidation over Ti/Nb-SiO_2 and Ti/Nb-NU-1000, where epoxide was observed. Cyclohexenone and cyclohexenol formed with ~ 20-25 % and ~ 10-15 % selectivity at reactor steady state. Unlike in the condensed phase, gas-phase oxidation also yields 10-15 % of the saturated product cyclohexanone. The selectivity to these three products increase with time, but stay in parallel.

Cyclohexenone and cyclohexenol are formed from radical oxidation at the allylic C-H bond via an intermediate cyclohexenyl hydroperoxide. Cyclohexanone could arise either from isomerization of epoxide or from direct radical attack at the C=C bond. Because cyclohexenone, cyclohexenol, and cyclohxanone all increase in selectivity in parallel – and in contrast to a drop in diol (derived from epoxide) selectivity – we assume it is more likely that cyclohexanone is also formed from a radical route. We interpret the overall pattern of product selectivity as indicating a slow conversion of a heterolytic H_2O_2 activation site for direct epoxidation, to a site more prone to homolytic activation of H_2O_2 and subsequent radical oxidation of cyclohexene. Scheme B.2 describes the proposed reaction networks toward radical and direct pathways in the gas phase, which is one possible mechanism of many possible routes. We suggest that formation of cyclohexanone occurs as the temperature rises upon hydroxyl radical attack on vinylic carbon.

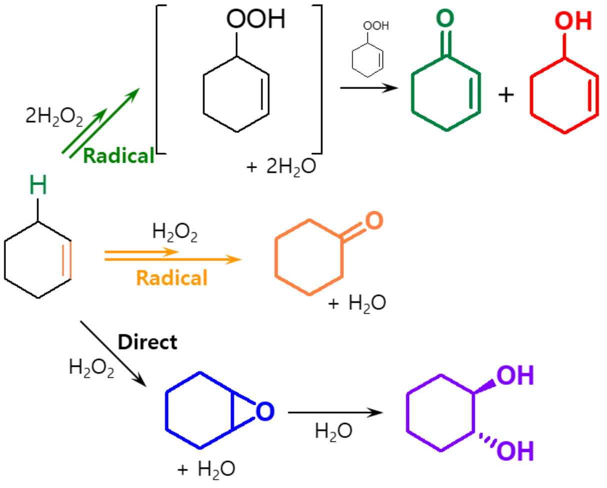

Scheme B.2. Proposed reaction network for gas-phase cyclohexene epoxidation.

B.4 Conclusions

MIL-47(V) is an effective catalyst for the production of C_6 oxygenates from cyclohexene and H_2O_2 in both the liquid and the gas phases at temperatures between 50 and 150 ºC. In all cases, PXRD confirms framework stabilities after reaction, and there was no evidence for leaching of an active species in the liquid-phase oxidation experiment.

Most importantly, we observe significant differences in product selectivity between liquid-phase and gas-phase operation. In the case of liquid-phase epoxidation at 65 °C, epoxide, cyclohexenol, and cyclohexenone are primary products. While there is sufficient H_2O_2, epoxide is formed directly from cyclohexene, and radical-derived cyclohexenyl hydroperoxide species give rise to the enol and enone products in similar amounts. Relatively small amounts of the hydrolysis product (diol) are formed. In the gas-phase catalytic reaction at 120 °C, diol (formed from epoxide) is the dominant product. The catalyst takes a long time to reach steady state conversion, then slowly changes in selectivity from one favoring direct oxidation pathways, to one that favors radical oxidation pathways. In contrast to reaction in the condensed phase, gas-phase radical products also include cyclohexanone.

Overall, these results demonstrate that an MOF with catalytically active VO_x nodes can give activity in liquid phase oxidation of cyclohexene with H_2O_2 that is similar to an oxide-supported VO_x catalyst. However, because the VO_x species are tightly incorporated into the MOF as nodes, these species are resistant to leaching. This work also finds that these catalysts are active in the gas phase oxidation of cyclohexene with H_2O_2 and that the frameworks remain intact even under these conditions. At the higher temperature gas-phase conditions, saturated oxygenates (cyclohexanone and diol) dominate, whereas allylic oxidation products (cyclohexenol and cyclohexenone) dominate at lower temperatures. Further studies in the gas phase will seek to understand the particular roles played by the absence of reaction solvent as well as the higher reaction temperature. This work can potentially help better understanding of alkene epoxidation in the liquid- and gas-phase over unconventional catalysts like catalytic node MOFs.

Appendix C. Cyclohexane Oxidative Dehydrogenation with N_2O over Tri-metallic Nodes as Catalysts

This appendix presents an experimental part from the following manuscript which I contributed as a second author to support computational predictions:

Melissa Barona, Sol Ahn, William Morris, William Hoover, Justin M. Notestein, Omar K. Farha, and Randall Q. Snurr, "Computational Predictions and Experimental Validation on the Activity of PCN-250 for Light Alkane Oxidative Dehydrogenation", *Manuscript in Preparation*, **2019**.

C.1 Experimental Methods

C.1.1 Materials Characterization

All reagents and solvents unless otherwise stated were obtained from commercial sources (Alfa Aesar and Sigma Aldrich) and were used without further purification. The 1.5 mm glass capillary tubes used to load Powder X-ray diffraction (PXRD) samples were purchased from Hampton Research. The MOF synthesis and nitrogen isotherms were performed at NuMat Technologies. PXRD experiments were conducted at the Jerome B. Cohen X-ray Diffraction Facility located at Northwestern University using the 18 kW Rigaku ATX-G Thin-film Diffraction Workstation. The samples were analyzed over a two theta range of 3 to 30 degrees and with a scan rate of 8 degrees/min. All N_2 gas adsorption and desorption measurements, unless stated otherwise, were performed on the Micromeritics Tristar II 3020 system (Micromeritics, Norcross, GA) at 77 K. Between 75-200 mg of samples were employed in each measurement. The specific surface areas for N_2 were calculated using the Brunauer-Emmet Teller (BET) model in the range of $0.005 < P/P_0 < 0.05$.

C.1.2 Reaction Methods

Cyclohexane ODH reaction studies were carried out in a plug-flow quartz tube reactor at 523 K over PCN-250(M). In order to maintain differential conversion regime (conversion less than 10% of cyclohexane), 100−200 mg of catalysts were used. For N_2O activation, the system was heated to 523 K with a ramp rate of 5.0 K/min and kept at 523 K for 8 h under flow of N_2O (5 mL/min, 1 %, Airgas). For reaction, in addition to same N_2O flow at same temperature, cyclohexane (≥ 99.0%, Sigma-Aldrich) was introduced by He (5 mL/min, 99.999 %, Airgas) saturator with a total pressure of 1.4 bar at 298 K (0.13 bar of reactant). Flow rates of reactant and oxidant were controlled by mass flow controllers (Altamira Instruments). Online product identification and quantification were performed by a 7890 A GC (Agilent Technologies) equipped with a flame ionization detector (FID) and a thermal conducvitiy detector (TCD). Hydrocarbons were separated by DB-Wax column (Agilent, 30 m length, 0.32 mm diameter, and 0.25 μm film), and then detected by a FID. Any other species were separated by a combination of HP-Plot/Q column (Agilent, 30 m length, 0.53 mm diameter, and 40 μm film) and HP-Molsieve column (Agilent, 15 m length, 0.53 mm diameter, and 50 μm film), and then detected by a TCD. The catalysis and online product analysis were performed in Clean Cat core facility at Northwestern University.

C.2 Results and Discussion

Samples of M-PCN-250 (M = Mn, Fe, Co, Ni) were synthesized following literature procedures from metal clusters ($Fe_2M(C_2H_3O_2)_6$) and the 3,3′,5,5′-azobenzenetetracarboxylate linker.[241] Powder X-ray diffractograms are in agreement with prior published results and with their calculated patterns (Figure C.1 (a)). Elemental analysis is consistent with ~ 1 M atom per 2 Fe atoms (Table C.1). N_2 physisoprtion gives a Type I isotherm for all materials (Figure C.1 (b)) with BET surface areas of ~1,700 m^2/g. All materials have a sharp pore size distribution near 1.1 nm (Figure C.1 (b) inset), as required from the crystal structures. Overall, the materials are fully consistent with prior published results.

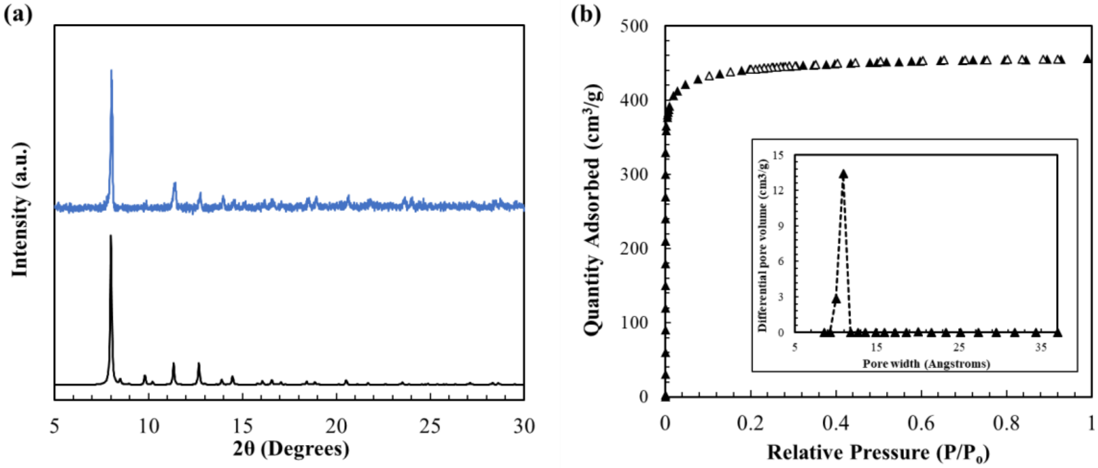

Figure C.1. Bulk characterization of PCN-250: (a) PXRD pattern (— simulated, — synthesized) (b) N_2 physisorption adsorption/desorption isotherm (inset: DFT pore size distribution)

Table C.1. Summary of catalysts.

Catalysts	M/node[a] [-]	Surface area[b] [m^2/g]	Steady rate[c] [$mmol_{product}/mol_{node}min$]
Fe-PCN-250	-	1,760	16.9 (37.9)
Mn-PCN-250	0.8	1,580	15.9 (38.6)
Co-PCN-250	0.9	1,690	11.9 (19.9)
Ni-PCN-250	1.2	1,680	7.2 (15.9)

[a]M/node from ICP. [b]Surface area from N_2 isotherm and BET equation. [c]Rates at 400 min TOS where product distribution approaches 100 % toward cyclohexene, and values in parenthesis are

initial rates that are obtained from extrapolation to 0 min TOS.

These materials were then tested in the vapor-phase oxidation of cyclohexane by N_2O at 250 ºC. Given that the DFT-predicted reactivity trends were predicated on rate-limiting N_2O activation, cyclohexane was used in 10:1 excess so as to help ensure rapid utilization of the oxidized form of the active site. Cyclohexane has a number of advantages for use as a reactant in alkane oxidation studies.[242-245] It has only a single type of C-H bond, faciliting comparison to theory, and its relatively large size makes all products readily detected by gas chromatograph even at low conversions. Most importantly, over-oxidation of cyclohexane leads to additional detectable products, such as benzene, in the case of ODH. This readily provides additional mechanistic information, unlike for molecules such as propane where overoxidation leads to CO_2.

Over 7 hours time-on-stream, cyclohexene and benzene are the only significant products, with trace levels of CO_2 as the overoxidation product. Plotting the reaction selectivity against instantaneous conversion (Figure C.2), the intrinsic reaction selectivity is calculated by extrapolation to zero conversion. Fe-PCN-250 and Mn-PCN-250 have near 100% intrinsic selectivity to cyclohexene while Co-PCN-250 and Ni-PCN-250 have 93-95% intrinsic selectivity to cyclohexene, with the remainder being benzene. The catalysts decrease moderately in selectivity with increasing conversion to form the benzene overoxidation product without significant CO_2 formation. As predicted from the N_2O activation energies, the catalytic turnover frequencies follow the trend Fe-PCN-250 ~ Mn-PCN-250, > Co-PCN-250 > Ni-PCN-250.

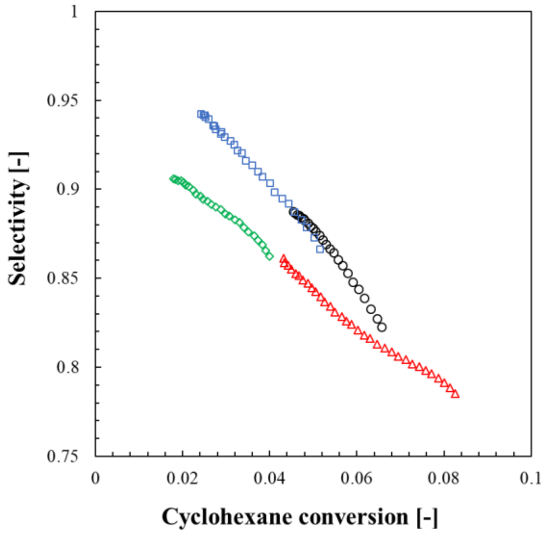

Figure C.2. Cyclohexane conversion vs. selectivity towards cyclohexene. (○ Fe-PCN-250; □Mn-PCN-250; △Co-PCN-250; ◇Ni-PCN-250)

References

(1) Bielanski, A., Haber, J., Oxygen in Catalysis. *Marcel Dekker, Inc.* **1991**.

(2) Centi, G.; Cavani, F.; Trifirò, F., Selective oxidation by heterogeneous catalysis. *Springer Science & Business Media:* **2012**.

(3) Hodnett, B. K., Heterogeneous Catalytic Oxidation: Fundamental and Technological Aspects of the Selective and Total Oxidation of Organic Compounds. *Wiley:* **2000**.

(4) Dever, J. P.; George, K. F.; Hoffman, W. C.; Soo, H., Ethylene Oxide. *John Wiley & Sons, Inc.,* **2000**.

(5) Wegener, S. L.; Marks, T. J.; Stair, P. C., Design Strategies for the Molecular Level Synthesis of Supported Catalysts. *Acc. Chem. Res.* **2012,** *45*, 206-214.

(6) Murray, L. J.; Dinca, M.; Long, J. R., Hydrogen storage in metal-organic frameworks. *Chem. Soc. Rev.* **2009,** *38*, 1294-1314.

(7) Farha, O. K.; Özgür Yazaydın, A.; Eryazici, I.; Malliakas, C. D.; Hauser, B. G.; Kanatzidis, M. G.; Nguyen, S. T.; Snurr, R. Q.; Hupp, J. T., De novo synthesis of a metal–organic framework material featuring ultrahigh surface area and gas storage capacities. *Nat. Chem.* **2010,** *2*, 944-948.

(8) Furukawa, H.; Ko, N.; Go, Y. B.; Aratani, N.; Choi, S. B.; Choi, E.; Yazaydin, A. Ö.; Snurr, R. Q.; O'Keeffe, M.; Kim, J.; Yaghi, O. M., Ultrahigh Porosity in Metal-Organic Frameworks. *Science* **2010,** *329*, 424-428.

(9) Grunker, R.; Bon, V.; Muller, P.; Stoeck, U.; Krause, S.; Mueller, U.; Senkovska, I.; Kaskel, S., A new metal-organic framework with ultra-high surface area. *Chem. Commun.* **2014,** *50*, 3450-3452.

(10) McDonald, T. M.; Mason, J. A.; Kong, X.; Bloch, E. D.; Gygi, D.; Dani, A.; Crocella, V.; Giordanino, F.; Odoh, S. O.; Drisdell, W. S.; Vlaisavljevich, B.; Dzubak, A. L.; Poloni, R.; Schnell, S. K.; Planas, N.; Lee, K.; Pascal, T.; Wan, L. F.; Prendergast, D.; Neaton, J. B.; Smit, B.; Kortright, J. B.; Gagliardi, L.; Bordiga, S.; Reimer, J. A.; Long, J. R., Cooperative insertion of CO2 in diamine-appended metal-organic frameworks. *Nature* **2015,** *519*, 303-308.

(11) Kreno, L. E.; Leong, K.; Farha, O. K.; Allendorf, M.; Van Duyne, R. P.; Hupp, J. T., Metal–Organic Framework Materials as Chemical Sensors. *Chem. Rev.* **2012,** *112*, 1105-1125.

(12) Lee, J.; Farha, O. K.; Roberts, J.; Scheidt, K. A.; Nguyen, S. T.; Hupp, J. T., Metal-organic framework materials as catalysts. *Chem. Soc. Rev.* **2009,** *38*, 1450-1459.

(13) Ma, L.; Abney, C.; Lin, W., Enantioselective catalysis with homochiral metal-organic frameworks. *Chem. Soc. Rev.* **2009,** *38*, 1248-1256.

(14) Miner, E. M.; Fukushima, T.; Sheberla, D.; Sun, L.; Surendranath, Y.; Dinca, M., Electrochemical oxygen reduction catalysed by Ni3(hexaiminotriphenylene)2. *Nat. Commun.* **2016,** *7*.

(15) Jiang, H.-L.; Feng, D.; Wang, K.; Gu, Z.-Y.; Wei, Z.; Chen, Y.-P.; Zhou, H.-C., An Exceptionally Stable, Porphyrinic Zr Metal–Organic Framework Exhibiting pH-Dependent Fluorescence. *J. Am. Chem. Soc.* **2013,** *135*, 13934-13938.

(16) Furukawa, H.; Gándara, F.; Zhang, Y.-B.; Jiang, J.; Queen, W. L.; Hudson, M. R.; Yaghi, O. M., Water Adsorption in Porous Metal–Organic Frameworks and Related Materials. *J. Am. Chem. Soc.* **2014,** *136*, 4369-4381.

(17) Mondloch, J. E.; Katz, M. J.; Planas, N.; Semrouni, D.; Gagliardi, L.; Hupp, J. T.; Farha, O. K., Are Zr6-based MOFs water stable? Linker hydrolysis vs. capillary-force-driven channel collapse. *Chem. Commun.* **2014,** *50*, 8944-8946.

(18) Jakobsen, S.; Gianolio, D.; Wragg, D. S.; Nilsen, M. H.; Emerich, H.; Bordiga, S.; Lamberti, C.; Olsbye, U.; Tilset, M.; Lillerud, K. P., Structural determination of a highly stable metal-organic framework with possible application to interim radioactive waste scavenging: Hf-UiO-66. *Phys. Rev. B* **2012,** *86*, 125429.

(19) Cavka, J. H.; Jakobsen, S.; Olsbye, U.; Guillou, N.; Lamberti, C.; Bordiga, S.; Lillerud, K. P., A New Zirconium Inorganic Building Brick Forming Metal Organic Frameworks with Exceptional Stability. *J. Am. Chem. Soc.* **2008,** *130*, 13850-13851.

(20) Wu, H.; Chua, Y. S.; Krungleviciute, V.; Tyagi, M.; Chen, P.; Yildirim, T.; Zhou, W., Unusual and Highly Tunable Missing-Linker Defects in Zirconium Metal–Organic Framework UiO-66 and Their Important Effects on Gas Adsorption. *J. Am. Chem. Soc.* **2013,** *135*, 10525-10532.

(21) Howarth, A. J.; Liu, Y.; Li, P.; Li, Z.; Wang, T. C.; Hupp, J. T.; Farha, O. K., Chemical, thermal and mechanical stabilities of metal–organic frameworks. *Nat. Rev. Mater.* **2016,** *1*, 15018.

(22) Wang, T. C.; Vermeulen, N. A.; Kim, I. S.; Martinson, A. B. F.; Stoddart, J. F.; Hupp, J. T.; Farha, O. K., Scalable synthesis and post-modification of a mesoporous metal-organic framework called NU-1000. *Nat. Protoc.* **2016,** *11*, 149-162.

(23) Deria, P.; Mondloch, J. E.; Tylianakis, E.; Ghosh, P.; Bury, W.; Snurr, R. Q.; Hupp, J. T.; Farha, O. K., Perfluoroalkane Functionalization of NU-1000 via Solvent-Assisted Ligand Incorporation: Synthesis and CO2 Adsorption Studies. *J. Am. Chem. Soc.* **2013,** *135*, 16801-16804.

(24) Klet, R. C.; Tussupbayev, S.; Borycz, J.; Gallagher, J. R.; Stalzer, M. M.; Miller, J. T.; Gagliardi, L.; Hupp, J. T.; Marks, T. J.; Cramer, C. J.; Delferro, M.; Farha, O. K., Single-Site Organozirconium Catalyst Embedded in a Metal–Organic Framework. *J. Am. Chem. Soc.* **2015,** *137*, 15680-15683.

(25) Rimoldi, M.; Nakamura, A.; Vermeulen, N. A.; Henkelis, J. J.; Blackburn, A. K.; Hupp, J. T.; Stoddart, J. F.; Farha, O. K., A metal-organic framework immobilised iridium pincer complex. *Chem. Sci.* **2016,** *7*, 4980-4984.

(26) Yang, D.; Odoh, S. O.; Wang, T. C.; Farha, O. K.; Hupp, J. T.; Cramer, C. J.; Gagliardi, L.; Gates, B. C., Metal–Organic Framework Nodes as Nearly Ideal Supports for Molecular Catalysts: NU-1000- and UiO-66-Supported Iridium Complexes. *J. Am. Chem. Soc.* **2015,** *137*, 7391-7396.

(27) Planas, N.; Mondloch, J. E.; Tussupbayev, S.; Borycz, J.; Gagliardi, L.; Hupp, J. T.; Farha, O. K.; Cramer, C. J., Defining the Proton Topology of the Zr6-Based Metal–Organic Framework NU-1000. *J. Phys. Chem. Lett.* **2014,** *5*, 3716-3723.

(28) Li, Z.; Schweitzer, N. M.; League, A. B.; Bernales, V.; Peters, A. W.; Getsoian, A. B.; Wang, T. C.; Miller, J. T.; Vjunov, A.; Fulton, J. L.; Lercher, J. A.; Cramer, C. J.; Gagliardi, L.; Hupp, J. T.; Farha, O. K., Sintering-Resistant Single-Site Nickel Catalyst Supported by Metal–Organic Framework. *J. Am. Chem. Soc.* **2016,** *138*, 1977-1982.

(29) Rouquerol, J.; Llewellyn, P.; Rouquerol, F., Is the bet equation applicable to microporous adsorbents? *Elsevier,* **2007,** Vol. 160, 49-56.

(30) Thornburg, N. E.; Thompson, A. B.; Notestein, J. M., Periodic Trends in Highly Dispersed Groups IV and V Supported Metal Oxide Catalysts for Alkene Epoxidation with H2O2. *ACS Catal.* **2015,** *5*, 5077-5088.

(31) Notestein, J. M.; Andrini, L. R.; Requejo, F. G.; Katz, A.; Iglesia, E., The Role of Outer-Sphere Surface Acidity in Alkene Epoxidation Catalyzed by Calixarene−Ti(IV) Complexes. *J. Am. Chem. Soc.* **2007,** *129*, 15585-15595.

(32) Eaton, T. R.; Campos, M. P.; Gray, K. A.; Notestein, J. M., Quantifying accessible sites and reactivity on titania–silica (photo)catalysts: Refining TOF calculations. *J. Catal.* **2014,** *309*, 156-165.

(33) Madrahimov, S. T.; Gallagher, J. R.; Zhang, G.; Meinhart, Z.; Garibay, S. J.; Delferro, M.; Miller, J. T.; Farha, O. K.; Hupp, J. T.; Nguyen, S. T., Gas-Phase Dimerization of Ethylene under Mild Conditions Catalyzed by MOF Materials Containing (bpy)NiII Complexes. *ACS Catal.* **2015,** *5*, 6713-6718.

(34) Yang, D.; Odoh, S. O.; Borycz, J.; Wang, T. C.; Farha, O. K.; Hupp, J. T.; Cramer, C. J.; Gagliardi, L.; Gates, B. C., Tuning Zr6 Metal–Organic Framework (MOF) Nodes as Catalyst Supports: Site Densities and Electron-Donor Properties Influence Molecular Iridium Complexes as Ethylene Conversion Catalysts. *ACS Catal.* **2016,** *6*, 235-247.

(35) Yang, D.; Momeni, M. R.; Demir, H.; Pahls, D. R.; Rimoldi, M.; Wang, T. C.; Farha, O. K.; Hupp, J. T.; Cramer, C. J.; Gates, B. C.; Gagliardi, L., Tuning the properties of metal–organic framework nodes as supports of single-site iridium catalysts: node modification by atomic layer deposition of aluminium. *Faraday Discuss.* **2017,** *201*, 195-206.

(36) Liu, J.; Ye, J.; Li, Z.; Otake, K.-i.; Liao, Y.; Peters, A. W.; Noh, H.; Truhlar, D. G.; Gagliardi, L.; Cramer, C. J.; Farha, O. K.; Hupp, J. T., Beyond the Active Site: Tuning the Activity and Selectivity of a Metal–Organic Framework-Supported Ni Catalyst for Ethylene Dimerization. *J. Am. Chem. Soc.* **2018,** *140*, 11174-11178.

(37) Goetjen, T. A.; Zhang, X.; Liu, J.; Hupp, J. T.; Farha, O. K., Metal–Organic Framework Supported Single Site Chromium(III) Catalyst for Ethylene Oligomerization at Low Pressure and Temperature. *ACS Sustainable Chem. Eng.* **2019,** *7*, 2553-2557.

(38) Rimoldi, M.; Hupp, J. T.; Farha, O. K., Atomic Layer Deposition of Rhenium–Aluminum Oxide Thin Films and ReOx Incorporation in a Metal–Organic Framework. *ACS Appl. Mater. Interfaces* **2017,** *9*, 35067-35074.

(39) Kim, I. S.; Li, Z.; Zheng, J.; Platero-Prats, A. E.; Mavrandonakis, A.; Pellizzeri, S.; Ferrandon, M.; Vjunov, A.; Gallington, L. C.; Webber, T. E.; Vermeulen, N. A.; Penn, R. L.; Getman, R. B.; Cramer, C. J.; Chapman, K. W.; Camaioni, D. M.; Fulton, J. L.; Lercher, J. A.; Farha, O. K.; Hupp, J. T.; Martinson, A. B. F., Sinter-Resistant Platinum Catalyst Supported by Metal–Organic Framework. *Angew. Chem. Int. Ed.* **2018,** *57*, 909-913.

(40) Redfern, L. R.; Li, Z.; Zhang, X.; Farha, O. K., Highly Selective Acetylene Semihydrogenation Catalyzed by Cu Nanoparticles Supported in a Metal–Organic Framework. *ACS Appl. Nano Mater.* **2018,** *1*, 4413-4417.

(41) Desai, S. P.; Ye, J.; Zheng, J.; Ferrandon, M. S.; Webber, T. E.; Platero-Prats, A. E.; Duan, J.; Garcia-Holley, P.; Camaioni, D. M.; Chapman, K. W.; Delferro, M.; Farha, O. K.; Fulton, J. L.; Gagliardi, L.; Lercher, J. A.; Penn, R. L.; Stein, A.; Lu, C. C., Well-Defined Rhodium–Gallium Catalytic Sites in a Metal–Organic Framework: Promoter-Controlled Selectivity in Alkyne Semihydrogenation to E-Alkenes. *J. Am. Chem. Soc.* **2018,** *140*, 15309-15318.

(42) Ikuno, T.; Zheng, J.; Vjunov, A.; Sanchez-Sanchez, M.; Ortuño, M. A.; Pahls, D. R.; Fulton, J. L.; Camaioni, D. M.; Li, Z.; Ray, D.; Mehdi, B. L.; Browning, N. D.; Farha, O. K.; Hupp, J. T.; Cramer, C. J.; Gagliardi, L.; Lercher, J. A., Methane Oxidation to Methanol Catalyzed by Cu-Oxo Clusters Stabilized in NU-1000 Metal–Organic Framework. *J. Am. Chem. Soc.* **2017,** *139*, 10294-

10301.

(43) Ahn, S.; Thornburg, N. E.; Li, Z.; Wang, T. C.; Gallington, L. C.; Chapman, K. W.; Notestein, J. M.; Hupp, J. T.; Farha, O. K., Stable Metal–Organic Framework-Supported Niobium Catalysts. *Inorg. Chem.* **2016,** *55*, 11954-11961.

(44) Noh, H.; Cui, Y.; Peters, A. W.; Pahls, D. R.; Ortuño, M. A.; Vermeulen, N. A.; Cramer, C. J.; Gagliardi, L.; Hupp, J. T.; Farha, O. K., An Exceptionally Stable Metal–Organic Framework Supported Molybdenum(VI) Oxide Catalyst for Cyclohexene Epoxidation. *J. Am. Chem. Soc.* **2016,** *138*, 14720-14726.

(45) Thompson, A. B.; Pahls, D. R.; Bernales, V.; Gallington, L. C.; Malonzo, C. D.; Webber, T.; Tereniak, S. J.; Wang, T. C.; Desai, S. P.; Li, Z.; Kim, I. S.; Gagliardi, L.; Penn, R. L.; Chapman, K. W.; Stein, A.; Farha, O. K.; Hupp, J. T.; Martinson, A. B. F.; Lu, C. C., Installing Heterobimetallic Cobalt–Aluminum Single Sites on a Metal Organic Framework Support. *Chem. Mater.* **2016,** *28*, 6753-6762.

(46) Cui, Y.; Rimoldi, M.; Platero-Prats, A. E.; Chapman, K. W.; Hupp, J. T.; Farha, O. K., Stabilizing a Vanadium Oxide Catalyst via Supporting on Metal-Organic Framework. *ChemCatChem* **2018,** *10*, 1772-1777.

(47) Otake, K.-i.; Cui, Y.; Buru, C. T.; Li, Z.; Hupp, J. T.; Farha, O. K., Single-Atom-Based Vanadium Oxide Catalysts Supported on Metal–Organic Frameworks: Selective Alcohol Oxidation and Structure–Activity Relationship. *J. Am. Chem. Soc.* **2018,** *140*, 8652-8656.

(48) Li, Z.; Peters, A. W.; Bernales, V.; Ortuño, M. A.; Schweitzer, N. M.; DeStefano, M. R.; Gallington, L. C.; Platero-Prats, A. E.; Chapman, K. W.; Cramer, C. J.; Gagliardi, L.; Hupp, J. T.; Farha, O. K., Metal–Organic Framework Supported Cobalt Catalysts for the Oxidative Dehydrogenation of Propane at Low Temperature. *ACS Cent. Sci.* **2017,** *3*, 31-38.

(49) Peters, A. W.; Otake, K.; Platero-Prats, A. E.; Li, Z.; DeStefano, M. R.; Chapman, K. W.; Farha, O. K.; Hupp, J. T., Site-Directed Synthesis of Cobalt Oxide Clusters in a Metal–Organic Framework. *ACS Appl. Mater. Interfaces* **2018,** *10*, 15073-15078.

(50) Li, Z.; Peters, A. W.; Platero-Prats, A. E.; Liu, J.; Kung, C.-W.; Noh, H.; DeStefano, M. R.; Schweitzer, N. M.; Chapman, K. W.; Hupp, J. T.; Farha, O. K., Fine-Tuning the Activity of Metal–Organic Framework-Supported Cobalt Catalysts for the Oxidative Dehydrogenation of Propane. *J. Am. Chem. Soc.* **2017,** *139*, 15251-15258.

(51) Rimoldi, M.; Bernales, V.; Borycz, J.; Vjunov, A.; Gallington, L. C.; Platero-Prats, A. E.; Kim, I. S.; Fulton, J. L.; Martinson, A. B. F.; Lercher, J. A.; Chapman, K. W.; Cramer, C. J.; Gagliardi, L.; Hupp, J. T.; Farha, O. K., Atomic Layer Deposition in a Metal–Organic Framework: Synthesis, Characterization, and Performance of a Solid Acid. *Chem. Mater.* **2017,** *29*, 1058-1068.

(52) Rimoldi, M.; Gallington, L. C.; Chapman, K. W.; MacRenaris, K.; Hupp, J. T.; Farha, O. K., Catalytically Active Silicon Oxide Nanoclusters Stabilized in a Metal–Organic Framework. *Chem. Eur. J.* **2017,** *23*, 8532-8536.

(53) Ahn, S.; Nauert, S. L.; Buru, C. T.; Rimoldi, M.; Choi, H.; Schweitzer, N. M.; Hupp, J. T.; Farha, O. K.; Notestein, J. M., Pushing the Limits on Metal–Organic Frameworks as a Catalyst Support: NU-1000 Supported Tungsten Catalysts for o-Xylene Isomerization and Disproportionation. *J. Am. Chem. Soc.* **2018,** *140*, 8535-8543.

(54) Mondloch, J. E.; Bury, W.; Fairen-Jimenez, D.; Kwon, S.; DeMarco, E. J.; Weston, M. H.; Sarjeant, A. A.; Nguyen, S. T.; Stair, P. C.; Snurr, R. Q.; Farha, O. K.; Hupp, J. T., Vapor-Phase Metalation by Atomic Layer Deposition in a Metal–Organic Framework. *J. Am. Chem. Soc.* **2013,** *135*, 10294-10297.

(55) Flytzani-Stephanopoulos, M.; Gates, B. C., Atomically Dispersed Supported Metal Catalysts. *Annu. Rev. Chem. Biomol. Eng.* **2012,** *3*, 545-574.

(56) Bartholomew, C. H.; Farrauto, R. J., Fundamentals of Industrial Catalytic Processes. 2nd ed.; *Wiley:* Hoboken, NJ, **2006**.

(57) Thomas, J. M.; Thomas, W. J., Principles and Practice of Heterogeneous Catalysis. *Wiley VCH:* New York, NY, **2005**.

(58) Thomas, J. M.; Raja, R.; Lewis, D. W., Single-Site Heterogeneous Catalysts. *Angew. Chem., Int. Ed.* **2005,** *44*, 6456-6482.

(59) Notestein, J. M.; Iglesia, E.; Katz, A., Grafted Metallocalixarenes as Single-Site Surface Organometallic Catalysts. *J. Am. Chem. Soc.* **2004,** *126*, 16478-16486.

(60) Stair, P. C., Synthesis of Supported Catalysts by Atomic Layer Deposition. *Top. Catal.* **2012,** *55*, 93-98.

(61) Lu, P.; Campbell, C. T.; Xia, Y., A sinter-resistant catalytic system fabricated by maneuvering the selectivity of SiO2 deposition onto the TiO2 surface versus the Pt nanoparticle surface. *Nano Lett.* **2013,** *13*, 4957-62.

(62) Bo, Z.; Eaton, T. R.; Gallagher, J. R.; Canlas, C. P.; Miller, J. T.; Notestein, J. M., Size-Selective Synthesis and Stabilization of Small Silver Nanoparticles on TiO2Partially Masked by SiO2. *Chem. Mater.* **2015,** *27*, 1269-1277.

(63) Boudart, M.; Djéga-Mariadassou, G., Kinetics of heterogeneous catalytic reactions. *Princeton University Press:* Princeton, N.J., **1984**.

(64) Kung, C.-W.; Mondloch, J. E.; Wang, T. C.; Bury, W.; Hoffeditz, W.; Klahr, B. M.; Klet, R. C.; Pellin, M. J.; Farha, O. K.; Hupp, J. T., Metal–Organic Framework Thin Films as Platforms for Atomic Layer Deposition of Cobalt Ions To Enable Electrocatalytic Water Oxidation. *ACS Appl. Mat. Interfaces* **2015,** *7*, 28223-28230.

(65) Peters, A. W.; Li, Z.; Farha, O. K.; Hupp, J. T., Atomically Precise Growth of Catalytically Active Cobalt Sulfide on Flat Surfaces and within a Metal–Organic Framework via Atomic Layer Deposition. *ACS Nano* **2015,** *9*, 8484-8490.

(66) Liu, T.-F.; Vermeulen, N. A.; Howarth, A. J.; Li, P.; Sarjeant, A. A.; Hupp, J. T.; Farha, O. K., Adding to the Arsenal of Zirconium-Based Metal–Organic Frameworks: the Topology as a Platform for Solvent-Assisted Metal Incorporation. *Eur. J. Inorg. Chem.* **2016,** *2016*, 4349-4352.

(67) Tanabe, K., Application of niobium oxides as catalysts. *Catal. Today* **1990,** *8*, 1-11.

(68) Wachs, I. E.; Jehng, J. M.; Deo, G.; Hu, H.; Arora, N., Catalytic Properties of Niobium Materials and Related Subjects (Proceedings of the Second International Symposium on Niobium Compounds)Redox properties of niobium oxide catalysts. *Catal. Today* **1996,** *28*, 199-205.

(69) Nowak, I.; Ziolek, M., Niobium Compounds: Preparation, Characterization, and Application in Heterogeneous Catalysis. *Chem. Rev.* **1999,** *99*, 3603-3624.

(70) Gao, X.; Wachs, I. E.; Wong, M. S.; Ying, J. Y., Structural and Reactivity Properties of Nb-MCM-41: Comparison with That of Highly Dispersed Nb2O5/SiO2 Catalysts. *J. Catal.* **2001,** *203*, 18-24.

(71) Aronne, A.; Turco, M.; Bagnasco, G.; Ramis, G.; Santacesaria, E.; Di Serio, M.; Marenna, E.; Bevilacqua, M.; Cammarano, C.; Fanelli, E., Gel derived niobium–silicon mixed oxides: Characterization and catalytic activity for cyclooctene epoxidation. *Appl. Catal. A Gen.* **2008,** *347*, 179-185.

(72) Nowak, I., Frontiers in mesoporous molecular sieves containing niobium: From model materials to catalysts. *Catal. Today* **2012,** *192*, 80-88.

(73) Tiozzo, C.; Bisio, C.; Carniato, F.; Marchese, L.; Gallo, A.; Ravasio, N.; Psaro, R.; Guidotti, M., Epoxidation with hydrogen peroxide of unsaturated fatty acid methyl esters over Nb(V)-silica catalysts. *Eur. J. Lipid Sci. Technol.* **2013,** *115*, 86-93.

(74) Gallo, A.; Tiozzo, C.; Psaro, R.; Carniato, F.; Guidotti, M., Niobium metallocenes deposited onto mesoporous silica via dry impregnation as catalysts for selective epoxidation of alkenes. *J. Catal.* **2013,** *298*, 77-83.

(75) Feliczak-Guzik, A.; Wawrzyńczak, A.; Nowak, I., Selective catalytic oxidations of cyclohexene, thioether and geraniol with hydrogen peroxide. Sensitivity to the structure of mesoporous niobosilicates. *Microporous Mesoporous Mater.* **2015,** *202*, 80-89.

(76) Turco, R.; Aronne, A.; Carniti, P.; Gervasini, A.; Minieri, L.; Pernice, P.; Tesser, R.; Vitiello, R.; Di Serio, M., Influence of preparation methods and structure of niobium oxide-based catalysts in the epoxidation reaction. *Catal. Today* **2015,** *254*, 99-103.

(77) D'Elia, V.; Dong, H.; Rossini, A. J.; Widdifield, C. M.; Vummaleti, S. V. C.; Minenkov, Y.; Poater, A.; Abou-Hamad, E.; Pelletier, J. D. A.; Cavallo, L.; Emsley, L.; Basset, J.-M., Cooperative Effect of Monopodal Silica-Supported Niobium Complex Pairs Enhancing Catalytic Cyclic Carbonate Production. *J. Am. Chem. Soc.* **2015,** *137*, 7728-7739.

(78) Jehng, J.-M.; Wachs, I. E., The molecular structures and reactivity of supported niobium oxide catalysts. *Catal. Today* **1990,** *8*, 37-55.

(79) Nowak, I.; Kilos, B.; Ziolek, M.; Lewandowska, A., Epoxidation of cyclohexene on Nb-containing meso- and macroporous materials. *Catal. Today* **2003,** *78*, 487-498.

(80) Sheldon, R. A., Synthetic and mechanistic aspects of metal-catalysed epoxidations with hydroperoxides. *J. Mol. Catal.* **1980,** *7*, 107-126.

(81) Thornburg, N. E.; Nauert, S. L.; Thompson, A. B.; Notestein, J. M., Synthesis−Structure–Function Relationships of Silica-Supported Niobium(V) Catalysts for Alkene Epoxidation with H2O2. *ACS Catal.* **2016,** *6*, 6124-6134.

(82) Li, P.; Klet, R. C.; Moon, S.-Y.; Wang, T. C.; Deria, P.; Peters, A. W.; Klahr, B. M.; Park, H.-J.; Al-Juaid, S. S.; Hupp, J. T.; Farha, O. K., Synthesis of nanocrystals of Zr-based metal-organic frameworks with csq-net: significant enhancement in the degradation of a nerve agent simulant. *Chem. Commun.* **2015,** *51*, 10925-10928.

(83) Toby, B. H.; Von Dreele, R. B., GSAS-II: the genesis of a modern open-source all purpose crystallography software package. *J. Appl. Crystallogr.* **2013,** *46*, 544-549.

(84) Le Bail, A.; Duroy, H.; Fourquet, J. L., Ab-initio structure determination of LiSbWO6 by X-ray powder diffraction. *Mat. Res. Bull.* **1988,** *23*, 447-452.

(85) Yakovenko, A. A.; Reibenspies, J. H.; Bhuvanesh, N.; Zhou, H.-C., Generation and applications of structure envelopes for porous metal-organic frameworks. *J. Appl. Crystallogr.* **2013,** *46*, 346-353.

(86) Yakovenko, A. A.; Wei, Z.; Wriedt, M.; Li, J.-R.; Halder, G. J.; Zhou, H.-C., Study of Guest

Molecules in Metal–Organic Frameworks by Powder X-ray Diffraction: Analysis of Difference Envelope Density. *Cryst. Growth Des.* **2014,** *14*, 5397-5407.

(87) Eaton, T. R.; Boston, A. M.; Thompson, A. B.; Gray, K. A.; Notestein, J. M., Counting Active Sites on Titanium Oxide–Silica Catalysts for Hydrogen Peroxide Activation through In Situ Poisoning with Phenylphosphonic Acid. *ChemCatChem* **2014,** *6*, 3215-3222.

(88) Nawrocki, J.; Rigney, M.; McCormick, A.; Carr, P. W., Chemistry of zirconia and its use in chromatography. *J. Chromatogr. A* **1993,** *657*, 229-282.

(89) Kouva, S.; Honkala, K.; Lefferts, L.; Kanervo, J., Review: monoclinic zirconia, its surface sites and their interaction with carbon monoxide. *Catal. Sci. Technol.* **2015,** *5*, 3473-3490.

(90) James, A. M.; Kowalczyk, P.; Fournier, R.; Simard, B., Electronic spectroscopy of the niobium dimer molecule: Experimental and theoretical results. *J. Chem. Phys.* **1993,** *99*, 8504-8518.

(91) Thornburg, N. E.; Liu, Y.; Li, P.; Hupp, J. T.; Farha, O. K.; Notestein, J. M., MOFs and their grafted analogues: regioselective epoxide ring-opening with Zr6 nodes. *Catal. Sci. Technol.* **2016,** *6*, 6480-6484.

(92) Deria, P.; Bury, W.; Hod, I.; Kung, C.-W.; Karagiaridi, O.; Hupp, J. T.; Farha, O. K., MOF Functionalization via Solvent-Assisted Ligand Incorporation: Phosphonates vs Carboxylates. *Inorg. Chem.* **2015,** *54*, 2185-2192.

(93) Klet, R. C.; Liu, Y.; Wang, T. C.; Hupp, J. T.; Farha, O. K., Evaluation of Bronsted acidity and proton topology in Zr- and Hf-based metal-organic frameworks using potentiometric acid-base titration. *J. Mat. Chem. A* **2016,** *4*, 1479-1485.

(94) Morlanés, N.; Notestein, J. M., Grafted Ta–calixarenes: Tunable, selective catalysts for direct olefin epoxidation with aqueous hydrogen peroxide. *J. Catal.* **2010,** *275*, 191-201.

(95) Fraile, J. M.; García, J. I.; Mayoral, J. A.; Vispe, E., Optimization of cyclohexene epoxidation with dilute hydrogen peroxide and silica-supported titanium catalysts. *Appl. Catal., A.* **2003,** *245*, 363-376.

(96) Fraile, J. M.; García, J. I.; Mayoral, J. A.; Vispe, E., Catalytic sites in silica-supported titanium catalysts: silsesquioxane complexes as models. *J. Catal.* **2005,** *233*, 90-99.

(97) Morlanés, N.; Notestein, J. M., Kinetic study of cyclooctene epoxidation with aqueous hydrogen peroxide over silica-supported calixarene–Ta(V). *Appl. Catal., A.* **2010,** *387*, 45-54.

(98) Clerici, M. G.; Kholdeeva, O. A., Liquid Phase Oxidation via Heterogeneous Catalysis:

Organic Synthesis and Industrial Applications. *Wiley,* **2013,** 526.

(99) Jones, C. W.; Clark, J. H., Application of hydrogen peroxide for the synthesis of fine chemicals. *The Royal Society of Chemistry,* **1999,** 79-178.

(100) Sienel, G.; Rieth, R.; Rowbottom, K. T., Epoxides In Ullmann's Encyclopedia of Industrial Chemistry. *Wiley,* **2000**.

(101) Fraile, J.; Garcia, J.; Mayoral, J.; Vispe, E., Catalytic sites in silica-supported titanium catalysts: silsesquioxane complexes as models. *J. Catal.* **2005,** *233*, 90-99.

(102) Gilbert, L.; Mercier, C., Solvent effects in heterogeneous catalysis : Application to the synthesis of fine chemicals. *Stud. Surf. Sci. Catal.* **1993,** *78*, 51-66.

(103) Balducci, L.; Bianchi, D.; Bortolo, R.; D'Aloisio, R.; Ricci, M.; Tassinari, R.; Ungarelli, R., Direct Oxidation of Benzene to Phenol with Hydrogen Peroxide over a Modified Titanium Silicalite. *Angew. Chem. Int. Ed.* **2003,** *42*, 4937-4940.

(104) Murata, K.; Yanyong, R.; Inaba, M., Effects of vanadium supported on ZrO2 and sulfolane on the synthesis of phenol by hydroxylation of benzene with oxygen and acetic acid on palladium catalyst. *Catal. Lett.* **2005,** *102*, 143-147.

(105) Nguyen, H. G. T.; Schweitzer, N. M.; Chang, C.-Y.; Drake, T. L.; So, M. C.; Stair, P. C.; Farha, O. K.; Hupp, J. T.; Nguyen, S. T., Vanadium-Node-Functionalized UiO-66: A Thermally Stable MOF-Supported Catalyst for the Gas-Phase Oxidative Dehydrogenation of Cyclohexene. *ACS Catal.* **2014,** *4*, 2496-2500.

(106) Perez Ferrandez, D. M.; de Croon, M. H. J. M.; Schouten, J. C.; Nijhuis, T. A., Gas-Phase Epoxidation of Propene with Hydrogen Peroxide Vapor. *Ind. Eng. Chem. Res.* **2013,** *52*, 10126-10132.

(107) Kwon, S.; Schweitzer, N. M.; Park, S.; Stair, P. C.; Snurr, R. Q., A kinetic study of vapor-phase cyclohexene epoxidation by H2O2 over mesoporous TS-1. *J. Catal.* **2015,** *326*, 107-115.

(108) Bregante, D. T.; Flaherty, D. W., Periodic Trends in Olefin Epoxidation over Group IV and V Framework-Substituted Zeolite Catalysts: A Kinetic and Spectroscopic Study. *J. Am. Chem. Soc.* **2017,** *139*, 6888-6898.

(109) Bregante, D. T.; Priyadarshini, P.; Flaherty, D. W., Kinetic and spectroscopic evidence for reaction pathways and intermediates for olefin epoxidation on Nb in *BEA. *J. Catal.* **2017,** *348*, 75-89.

(110) Bregante, D. T.; Thornburg, N. E.; Notestein, J. M.; Flaherty, D. W., Consequences of Confinement for Alkene Epoxidation with Hydrogen Peroxide on Highly Dispersed Group 4 and 5 Metal Oxide Catalysts. *ACS Catal.* **2018,** *8*, 2995-3010.

(111) Schoenfeldt, N. J.; Korinda, A. W.; Notestein, J. M., A heterogeneous, selective oxidation catalyst based on Mn triazacyclononane grafted under reaction conditions. *Chem. Commun.* **2010,** *46*, 1640-1642.

(112) Yamamoto, N.; Sato, S.; Takahashi, R.; Inui, K., Synthesis of homoallyl alcohol from 1,4-butanediol over ZrO2 catalyst. *Catal. Commun.* **2005,** *6*, 480-484.

(113) Yamamoto, N.; Sato, S.; Takahashi, R.; Inui, K., Synthesis of 3-buten-1-ol from 1,4-butanediol over ZrO2 catalyst. *J. Mol. Catal. A: Chem.* **2006,** *243*, 52-59.

(114) Ichikawa, N.; Sato, S.; Takahashi, R.; Sodesawa, T., Catalytic reaction of 1,3-butanediol over solid acids. *J. Mol. Catal. A: Chem.* **2006,** *256*, 106-112.

(115) Inoue, H.; Sato, S.; Takahashi, R.; Izawa, Y.; Ohno, H.; Takahashi, K., Dehydration of 1,4-butanediol over supported rare earth oxide catalysts. *Appl. Catal., A* **2009,** *352*, 66-73.

(116) Duan, H.; Sun, D.; Yamada, Y.; Sato, S., Dehydration of 2,3-butanediol into 3-buten-2-ol catalyzed by ZrO2. *Catal. Commun.* **2014,** *48*, 1-4.

(117) Notestein, J. M.; Katz, A.; Iglesia, E., Energetics of Small Molecule and Water Complexation in Hydrophobic Calixarene Cavities. *Langmuir* **2006,** *22*, 4004-4014.

(118) Martens, J. A.; Perez-Pariente, J.; Sastre, E.; Corma, A.; Jacobs, P. A., Isomerization and disproportionation of m-xylene: Selectivities Induced by the Void Structure of the Zeolite Framework. *Appl. Catal.* **1988,** *45*, 85-101.

(119) Guisnet, M.; Gnep, N. S.; Morin, S., Mechanisms of xylene isomerization over acidic solid catalysts. *Micropor. Mesopor. Mat.* **2000,** *35-36*, 47-59.

(120) Lanewala, M. A.; Bolton, A. P., Isomerization of the xylenes using zeolite catalysts. *J. Org. Chem.* **1969,** *34*, 3107-3112.

(121) Hino, M.; Arata, K., Synthesis of solid superacid of tungsten oxide supported on zirconia and its catalytic action for reactions of butane and pentane. *J. Chem. Soc., Chem. Commun.* **1988**, 1259-1260.

(122) Soultanidis, N.; Zhou, W.; Psarras, A. C.; Gonzalez, A. J.; Iliopoulou, E. F.; Kiely, C. J.; Wachs, I. E.; Wong, M. S., Relating n-Pentane Isomerization Activity to the Tungsten Surface

Density of WOx/ZrO2. *J. Am. Chem. Soc.* **2010,** *132*, 13462-13471.

(123) Larsen, G.; Lotero, E.; Petkovic, L. a. M.; Shobe, D. S., Alcohol Dehydration Reactions over Tungstated Zirconia Catalysts. *J. Catal.* **1997,** *169*, 67-75.

(124) Rorrer, J.; He, Y.; Toste, F. D.; Bell, A. T., Mechanism and kinetics of 1-dodecanol etherification over tungstated zirconia. *J. Catal.* **2017,** *354*, 13-23.

(125) Barton, D. G.; Shtein, M.; Wilson, R. D.; Soled, S. L.; Iglesia, E., Structure and Electronic Properties of Solid Acids Based on Tungsten Oxide Nanostructures. *J. Phys. Chem. B* **1999,** *103*, 630-640.

(126) Wilson, R. D.; Barton, D. G.; Baertsch, C. D.; Iglesia, E., Reaction and Deactivation Pathways in Xylene Isomerization on Zirconia Modified by Tungsten Oxide. *J. Catal.* **2000,** *194*, 175-187.

(127) Baertsch, C. D.; Soled, S. L.; Iglesia, E., Isotopic and Chemical Titration of Acid Sites in Tungsten Oxide Domains Supported on Zirconia. *J. Phys. Chem. B* **2001,** *105*, 1320-1330.

(128) Barton, D. G.; Soled, S. L.; Iglesia, E., Solid acid catalysts based on supported tungsten oxides. *Top. Catal.* **1998,** *6*, 87-99.

(129) Wang, Y.; Hou, Y.; Song, H., Ring-closing depolymerization of polytetrahydrofuran to produce tetrahydrofuran using heteropolyacid as catalyst. *Polym. Degrad. Stab.* **2017,** *144*, 17-23.

(130) Nie, G.; Li, G.; Liang, D.; Zhang, X., Alkylation of toluene with cyclohexene over phosphotungstic acid: A combined experimental and computational study. *J. Catal.* **2017,** *355*, 145-155.

(131) Kukovecz, Á.; Balogi, Z.; Kónya, Z.; Toba, M.; Lentz, P.; Niwa, S. I.; Mizukami, F.; Molnár, Á.; Nagy, J. B.; Kiricsi, I., Synthesis, characterisation and catalytic applications of sol–gel derived silica–phosphotungstic acid composites. *Appl. Catal., A.* **2002,** *228*, 83-94.

(132) Devassy, B. M.; Shanbhag, G. V.; Lefebvre, F.; Böhringer, W.; Fletcher, J.; Halligudi, S. B., Zirconia-supported phosphotungstic acid as catalyst for alkylation of phenol with benzyl alcohol. *J. Mol. Catal. A: Chem.* **2005,** *230*, 113-119.

(133) Macht, J.; Janik, M. J.; Neurock, M.; Iglesia, E., Mechanistic Consequences of Composition in Acid Catalysis by Polyoxometalate Keggin Clusters. *J. Am. Chem. Soc.* **2008,** *130*, 10369-10379.

(134) Hendon, C. H.; Rieth, A. J.; Korzyński, M. D.; Dincă, M., Grand Challenges and Future Opportunities for Metal–Organic Frameworks. *ACS Cent. Sci.* **2017,** *3*, 554-563.

(135) Rimoldi, M.; Howarth, A. J.; DeStefano, M. R.; Lin, L.; Goswami, S.; Li, P.; Hupp, J. T.; Farha, O. K., Catalytic Zirconium/Hafnium-Based Metal–Organic Frameworks. *ACS Catal.* **2017,** *7*, 997-1014.

(136) Teplensky, M. H.; Fantham, M.; Li, P.; Wang, T. C.; Mehta, J. P.; Young, L. J.; Moghadam, P. Z.; Hupp, J. T.; Farha, O. K.; Kaminski, C. F.; Fairen-Jimenez, D., Temperature Treatment of Highly Porous Zirconium-Containing Metal–Organic Frameworks Extends Drug Delivery Release. *J. Am. Chem. Soc.* **2017,** *139*, 7522-7532.

(137) Stassen, I.; Burtch, N.; Talin, A.; Falcaro, P.; Allendorf, M.; Ameloot, R., An updated roadmap for the integration of metal-organic frameworks with electronic devices and chemical sensors. *Chem. Soc. Rev.* **2017,** *46*, 3185-3241.

(138) Zhang, Y.; Degirmenci, V.; Li, C.; Hensen, E. J. M., Phosphotungstic Acid Encapsulated in Metal–Organic Framework as Catalysts for Carbohydrate Dehydration to 5-Hydroxymethylfurfural. *ChemSusChem* **2011,** *4*, 59-64.

(139) Wang, P.; Feng, J.; Zhao, Y.; Wang, S.; Liu, J., MOF-Derived Tungstated Zirconia as Strong Solid Acids toward High Catalytic Performance for Acetalization. *ACS Appl. Mater. Interfaces* **2016,** *8*, 23755-23762.

(140) Vermoortele, F.; Ameloot, R.; Alaerts, L.; Matthessen, R.; Carlier, B.; Fernandez, E. V. R.; Gascon, J.; Kapteijn, F.; De Vos, D. E., Tuning the catalytic performance of metal-organic frameworks in fine chemistry by active site engineering. *J. Mater. Chem.* **2012,** *22*, 10313-10321.

(141) Zang, Y.; Shi, J.; Zhang, F.; Zhong, Y.; Zhu, W., Sulfonic acid-functionalized MIL-101 as a highly recyclable catalyst for esterification. *Catal. Sci. Technol.* **2013,** *3*, 2044-2049.

(142) Khder, A. E. R. S.; Hassan, H. M. A.; El-Shall, M. S., Metal-organic frameworks with high tungstophosphoric acid loading as heterogeneous acid catalysts. *Appl. Catal., A.* **2014,** *487*, 110-118.

(143) Wan, H.; Chen, C.; Wu, Z.; Que, Y.; Feng, Y.; Wang, W.; Wang, L.; Guan, G.; Liu, X., Encapsulation of Heteropolyanion-Based Ionic Liquid within the Metal–Organic Framework MIL-100(Fe) for Biodiesel Production. *ChemCatChem* **2015,** *7*, 441-449.

(144) Li, B.; Leng, K.; Zhang, Y.; Dynes, J. J.; Wang, J.; Hu, Y.; Ma, D.; Shi, Z.; Zhu, L.; Zhang, D.; Sun, Y.; Chrzanowski, M.; Ma, S., Metal–Organic Framework Based upon the Synergy of a Brønsted Acid Framework and Lewis Acid Centers as a Highly Efficient Heterogeneous Catalyst for Fixed-Bed Reactions. *J. Am. Chem. Soc.* **2015,** *137*, 4243-4248.

(145) Nguyen, L. T. L.; Nguyen, C. V.; Dang, G. H.; Le, K. K. A.; Phan, N. T. S., Towards

applications of metal–organic frameworks in catalysis: Friedel–Crafts acylation reaction over IRMOF-8 as an efficient heterogeneous catalyst. *J. Mol. Catal. A: Chem.* **2011,** *349*, 28-35.

(146) Buru, C. T.; Li, P.; Mehdi, B. L.; Dohnalkova, A.; Platero-Prats, A. E.; Browning, N. D.; Chapman, K. W.; Hupp, J. T.; Farha, O. K., Adsorption of a Catalytically Accessible Polyoxometalate in a Mesoporous Channel-type Metal–Organic Framework. *Chem. Mater.* **2017,** *29*, 5174-5181.

(147) Sofia, L. T. A.; Krishnan, A.; Sankar, M.; Kala Raj, N. K.; Manikandan, P.; Rajamohanan, P. R.; Ajithkumar, T. G., Immobilization of Phosphotungstic Acid (PTA) on Imidazole Functionalized Silica: Evidence for the Nature of PTA Binding by Solid State NMR and Reaction Studies. *J. Phys. Chem. C* **2009,** *113*, 21114-21122.

(148) Kozhevnikov, I. V.; Kloetstra, K. R.; Sinnema, A.; Zandbergen, H. W.; van Bekkum, H., Study of catalysts comprising heteropoly acid H3PW12O40 supported on MCM-41 molecular sieve and amorphous silica. *J. Mol. Catal. A: Chem.* **1996,** *114*, 287-298.

(149) Kochubey, D. I.; Berdnikova, P. V.; Pai, Z. P.; Chesalov, Y. A.; Kanazhevskiy, V. V.; Khlebnikova, T. B., Structure and properties of tungsten peroxopolyoxo complexes – promising catalysts for organics oxidation. II: Cation type influence on the tungsten peroxocomplex structure. *J. Mol. Catal. A: Chem.* **2013,** *366*, 341-346.

(150) Ladera, R. M.; Ojeda, M.; Fierro, J. L. G.; Rojas, S., TiO2-supported heteropoly acid catalysts for dehydration of methanol to dimethyl ether: relevance of dispersion and support interaction. *Catal. Sci. Technol.* **2015,** *5*, 484-491.

(151) Kozhevnikov, I. V., Catalysis by Heteropoly Acids and Multicomponent Polyoxometalates in Liquid-Phase Reactions. *Chem. Rev.* **1998,** *98*, 171-198.

(152) Misono, M., Heterogeneous Catalysis by Heteropoly Compounds of Molybdenum and Tungsten. *Catal. Rev.* **1987,** *29*, 269-321.

(153) Bardin, B. B.; Davis, R. J., Effect of water on silica-supported phosphotungstic acid catalysts for 1-butene double bond shift and alkane skeletal isomerization. *Appl. Catal., A* **2000,** *200*, 219-231.

(154) Grinenval, E.; Garron, A.; Lefebvre, F., n-Butane Isomerization over Silica-Supported Heteropolyacids: Study of Some Parameters. *J. Catal.* **2013,** *2013*, 8.

(155) Figueras, F., Pillared Clays as Catalysts. *Catal. Rev.* **1988,** *30*, 457-499.

(156) Lee, W. Y.; Raythatha, R. H.; Tatarchuk, B. J., Pillared-clay catalysts containing mixed-metal

complexes: I. Preparation and characterization. *J. Catal.* **1989,** *115*, 159-179.

(157) Lambert, J.-F.; Poncelet, G., Acidity in pillared clays: origin and catalytic manifestations. *Top. Catal.* **1997,** *4*, 43-56.

(158) Zhu, S.; Zhu, Y.; Hao, S.; Zheng, H.; Mo, T.; Li, Y., One-step hydrogenolysis of glycerol to biopropanols over Pt-H4SiW12O40/ZrO2 catalysts. *Green Chem.* **2012,** *14*, 2607-2616.

(159) van Donk, S.; Bitter, J. H.; de Jong, K. P., Deactivation of solid acid catalysts for butene skeletal isomerisation: on the beneficial and harmful effects of carbonaceous deposits. *Appl. Catal. A Gen.* **2001,** *212*, 97-116.

(160) Srivastava, R.; Choi, M.; Ryoo, R., Mesoporous materials with zeolite framework: remarkable effect of the hierarchical structure for retardation of catalyst deactivation. *Chem. Commun.* **2006**, 4489-4491.

(161) Wang, P.; Zhang, W.; Zhang, Q.; Xu, Z.; Yang, C.; Li, C., Comparative study of n-butane isomerization over SO42−/Al2O3-ZrO2 and HZSM-5 zeolites at low reaction temperatures. *Appl. Catal. A Gen.* **2018,** *550*, 98-104.

(162) Beck, J. S.; Haag, W. O.; Buonomo, F.; Sanfilippo, D.; Trifirò, F.; Arnold, H.; Döbert, F.; Gaube, J., Organic Reactions: Sections 4.1 – 4.4. *Wiley-VCH Verlag GmbH,* **2008,** 2123-2231.

(163) Corma, A.; Iborra, S.; Mifsud, M.; Renz, M., A new, alternative, halogen-free synthesis for the fragrance compound Melonal using zeolites and mesoporous materials as oxidation catalysts. *Journal of Catalysis* **2005,** *234*, 96-100.

(164) Collins, D. J.; Mulrooney, K. J.; Medina, R. J.; Davis, B. H., Xylene isomerization and disproportionation over lanthanum Y catalyst. *J. Catal.* **1982,** *75*, 291-301.

(165) Min, H.-K.; Cha, S. H.; Hong, S. B., Mechanistic Insights into the Zeolite-Catalyzed Isomerization and Disproportionation of m-Xylene. *ACS Catal.* **2012,** *2*, 971-981.

(166) Su, F.; Wu, Q.; Song, D.; Zhang, X.; Wang, M.; Guo, Y., Pore morphology-controlled preparation of ZrO2-based hybrid catalysts functionalized by both organosilica moieties and Keggin-type heteropoly acid for the synthesis of levulinate esters. *J. Mater. Chem. A* **2013,** *1*, 13209-13221.

(167) Paille, G.; Gomez-Mingot, M.; Roch-Marchal, C.; Lassalle-Kaiser, B.; Mialane, P.; Fontecave, M.; Mellot-Draznieks, C.; Dolbecq, A., A Fully Noble Metal-Free Photosystem Based on Cobalt-Polyoxometalates Immobilized in a Porphyrinic Metal–Organic Framework for Water Oxidation. *J. Am. Chem. Soc.* **2018**.

(168) Buru, C. T.; Platero-Prats, A. E.; Chica, D. G.; Kanatzidis, M. G.; Chapman, K. W.; Farha, O. K., Thermally induced migration of a polyoxometalate within a metal-organic framework and its catalytic effects. *J. Mater. Chem. A* **2018,** *6*, 7389-7394.

(169) Malonzo, C. D.; Shaker, S. M.; Ren, L.; Prinslow, S. D.; Platero-Prats, A. E.; Gallington, L. C.; Borycz, J.; Thompson, A. B.; Wang, T. C.; Farha, O. K.; Hupp, J. T.; Lu, C. C.; Chapman, K. W.; Myers, J. C.; Penn, R. L.; Gagliardi, L.; Tsapatsis, M.; Stein, A., Thermal Stabilization of Metal–Organic Framework-Derived Single-Site Catalytic Clusters through Nanocasting. *J. Am. Chem. Soc.* **2016,** *138*, 2739-2748.

(170) Yan, X.; Lu, N.; Fan, B.; Bao, J.; Pan, D.; Wang, M.; Li, R., Synthesis of mesoporous and tetragonal zirconia with inherited morphology from metal-organic frameworks. *CrystEngComm* **2015,** *17*, 6426-6433.

(171) Tang, J.; Salunkhe, R. R.; Liu, J.; Torad, N. L.; Imura, M.; Furukawa, S.; Yamauchi, Y., Thermal Conversion of Core–Shell Metal–Organic Frameworks: A New Method for Selectively Functionalized Nanoporous Hybrid Carbon. *J. Am. Chem. Soc.* **2015,** *137*, 1572-1580.

(172) Thomas, J. M.; Raja, R.; Sankar, G.; Bell, R. G., Molecular-sieve catalysts for the selective oxidation of linear alkanes by molecular oxygen. *Nature* **1999,** *398*, 227.

(173) Yuan, H.-X.; Xia, Q.-H.; Zhan, H.-J.; Lu, X.-H.; Su, K.-X., Catalytic oxidation of cyclohexane to cyclohexanone and cyclohexanol by oxygen in a solvent-free system over metal-containing ZSM-5 catalysts. *Appl. Catal. A Gen.* **2006,** *304*, 178-184.

(174) Dias Ribeiro de Sousa Martins, L. M.; Carabineiro, S. A. C.; Wang, J.; Rocha, B. G. M.; Maldonado-Hódar, F. J.; Latourrette de Oliveira Pombeiro, A. J., Supported gold nanoparticles as reusable catalysts for oxidation reactions of industrial significance. *ChemCatChem* **2017,** *9*, 1211-1221.

(175) Schuchardt, U.; Cardoso, D.; Sercheli, R.; Pereira, R.; Da Cruz, R. S.; Guerreiro, M. C.; Mandelli, D.; Spinacé, E. V.; Pires, E. L., Cyclohexane oxidation continues to be a challenge. *Appl. Catal. A Gen.* **2001,** *211*, 1-17.

(176) Shylesh, S.; Samuel, P. P.; Singh, A., Chromium-containing small pore mesoporous silicas: Synthesis, characterization and catalytic behavior in the liquid phase oxidation of cyclohexane. *Appl. Catal. A Gen.* **2007,** *318*, 128-136.

(177) Sheldon, R. A.; Kochi, J. K., Metal-catalyzed oxidations of organic compounds in the liquid phase: A mechanistic approach. *Elsevier,* **1976,** Vol. 25, 272-413.

(178) Betsy, K. J.; Nayak, C.; Lazar, A.; Krishnan, A.; Bhattacharyya, D.; Jha, S. N.; Vinod, C. P.,

Selective oxidation of cyclohexane to cyclohexanone using chromium oxide supported mesoporous MCM-41 nanospheres: Probing the nature of catalytically active chromium sites. *ChemCatChem* **2018,** *10*, 3291-3298.

(179) Martins, L. M. D.; de Almeida, M. P.; Carabineiro, S.; Figueiredo, J.; Pombeiro, A., Heterogenisation of a C-Scorpionate FeII Complex on Carbon Materials for Cyclohexane Oxidation with Hydrogen Peroxide. *ChemCatChem* **2013,** *5*, 3847-3856.

(180) de Almeida, M. P.; Martins, L.; Carabineiro, S.; Lauterbach, T.; Rominger, F.; Hashmi, A.; Pombeiro, A.; Figueiredo, J., Homogeneous and heterogenised new gold C-scorpionate complexes as catalysts for cyclohexane oxidation. *Catal. Sci. Technol.* **2013,** *3*, 3056-3069.

(181) Silva, T. F.; Mac Leod, T. C.; Martins, L. M.; da Silva, M. F. C. G.; Schiavon, M. A.; Pombeiro, A. J., Pyrazole or tris (pyrazolyl) ethanol oxo-vanadium (IV) complexes as homogeneous or supported catalysts for oxidation of cyclohexane under mild conditions. *J. Mol. Catal. A: Chem.* **2013,** *367*, 52-60.

(182) Mishra, G. S.; Alegria, E. C.; Martins, L. M.; da Silva, J. J. F.; Pombeiro, A. J., Cyclohexane oxidation with dioxygen catalyzed by supported pyrazole rhenium complexes. *J. Mol. Catal. A: Chem.* **2008,** *285*, 92-100.

(183) Martins, L. M. D.; Martins, A.; Alegria, E. C.; Carvalho, A.; Pombeiro, A. J., Efficient cyclohexane oxidation with hydrogen peroxide catalysed by a C-scorpionate iron (II) complex immobilized on desilicated MOR zeolite. *Appl. Catal. A Gen.* **2013,** *464*, 43-50.

(184) Selvam, P.; Dapurkar, S., Catalytic activity of highly ordered mesoporous VMCM-48. *Appl. Catal. A Gen.* **2004,** *276*, 257-265.

(185) Férey, G., Hybrid porous solids: past, present, future. *Chem. Soc. Rev.* **2008,** *37*, 191-214.

(186) Yang, Q.; Liu, D.; Zhong, C.; Li, J.-R., Development of computational methodologies for metal–organic frameworks and their application in gas separations. *Chem. Rev.* **2013,** *113*, 8261-8323.

(187) Liu, J.; Chen, L.; Cui, H.; Zhang, J.; Zhang, L.; Su, C.-Y., Applications of metal–organic frameworks in heterogeneous supramolecular catalysis. *Chem. Soc. Rev.* **2014,** *43*, 6011-6061.

(188) Bae, Y.-S.; Mulfort, K. L.; Frost, H.; Ryan, P.; Punnathanam, S.; Broadbelt, L. J.; Hupp, J. T.; Snurr, R. Q., Separation of CO2 from CH4 using mixed-ligand metal− organic frameworks. *Langmuir* **2008,** *24*, 8592-8598.

(189) Bae, Y. S.; Snurr, R. Q., Development and evaluation of porous materials for carbon dioxide

separation and capture. *Angew. Chem. Int. Ed.* **2011,** *50*, 11586-11596.

(190) Kim, S.-Y.; Yoon, T.-U.; Kang, J. H.; Kim, A.-R.; Kim, T.-H.; Kim, S.-I.; Park, W.; Kim, K. C.; Bae, Y.-S., Observation of Olefin/Paraffin Selectivity in Azo Compound and Its Application into a Metal–Organic Framework. *ACS Appl. Mater. Interfaces* **2018,** *10*, 27521-27530.

(191) Getman, R. B.; Bae, Y.-S.; Wilmer, C. E.; Snurr, R. Q., Review and analysis of molecular simulations of methane, hydrogen, and acetylene storage in metal–organic frameworks. *Chem. Rev.* **2011,** *112*, 703-723.

(192) Kim, S.-Y.; Kim, A.-R.; Yoon, J. W.; Kim, H.-J.; Bae, Y.-S., Creation of mesoporous defects in a microporous metal-organic framework by an acetic acid-fragmented linker co-assembly and its remarkable effects on methane uptake. *Chem. Eng. J.* **2018,** *335*, 94-100.

(193) Kim, S.-I.; Yoon, T.-U.; Kim, M.-B.; Lee, S.-J.; Hwang, Y. K.; Chang, J.-S.; Kim, H.-J.; Lee, H.-N.; Lee, U.-H.; Bae, Y.-S., Metal–organic frameworks with high working capacities and cyclic hydrothermal stabilities for fresh water production. *Chem. Eng. J.* **2016,** *286*, 467-475.

(194) Ahn, S.; Thornburg, N. E.; Li, Z. Y.; Wang, T. C.; Gallington, L. C.; Chapman, K. W.; Notestein, J. M.; Hupp, J. T.; Farha, O. K., Stable Metal-Organic Framework-Supported Niobium Catalysts. *Inorg. Chem.* **2016,** *55*, 11954-11961.

(195) Kim, A.-R.; Yoon, T.-U.; Kim, E.-J.; Yoon, J. W.; Kim, S.-Y.; Yoon, J. W.; Hwang, Y. K.; Chang, J.-S.; Bae, Y.-S., Facile loading of Cu (I) in MIL-100 (Fe) through redox-active Fe (II) sites and remarkable propylene/propane separation performance. *Chem. Eng. J.* **2018,** *331*, 777-784.

(196) Yoon, J. W.; Seo, Y. K.; Hwang, Y. K.; Chang, J. S.; Leclerc, H.; Wuttke, S.; Bazin, P.; Vimont, A.; Daturi, M.; Bloch, E., Controlled reducibility of a metal–organic framework with coordinatively unsaturated sites for preferential gas sorption. *Angew. Chem. Int. Ed.* **2010,** *49*, 5949-5952.

(197) Tang, J.; Wang, J., Fe-based metal organic framework/graphene oxide composite as an efficient catalyst for Fenton-like degradation of methyl orange. *RSC Adv* **2017,** *7*, 50829-50837.

(198) Li, L.; Yang, Q.; Chen, S.; Hou, X.; Liu, B.; Lu, J.; Jiang, H.-L., Boosting selective oxidation of cyclohexane over a metal–organic framework by hydrophobicity engineering of pore walls. *Chem. Commun.* **2017,** *53*, 10026-10029.

(199) Xiao, D. J.; Oktawiec, J.; Milner, P. J.; Long, J. R., Pore Environment Effects on Catalytic Cyclohexane Oxidation in Expanded Fe2 (dobdc) Analogues. *J. Am. Chem. Soc.* **2016,** *138*, 14371-14379.

(200) Kim, A.-R.; Yoon, T.-U.; Kim, S.-I.; Cho, K.; Han, S.-S.; Bae, Y.-S., Creating high CO/CO2 selectivity and large CO working capacity through facile loading of Cu (I) species into an iron-based mesoporous metal-organic framework. *Chem. Eng. J.* **2018,** *348*, 135-142.

(201) Shul'pin, G. B.; Kozlov, Y. N.; Shul'pina, L. S.; Kudinov, A. R.; Mandelli, D., Extremely efficient alkane oxidation by a new catalytic reagent H2O2/Os3 (CO) 12/pyridine. *Inorg. chem.* **2009,** *48*, 10480-10482.

(202) Shul'pin, G. B., C–H functionalization: thoroughly tuning ligands at a metal ion, a chemist can greatly enhance catalyst's activity and selectivity. *Dalton Trans.* **2013,** *42*, 12794-12818.

(203) Walton, K. S.; Snurr, R. Q., Applicability of the BET method for determining surface areas of microporous metal− organic frameworks. *J. Am. Chem. Soc.* **2007,** *129*, 8552-8556.

(204) Yoon, J. W.; Kim, A.-R.; Kim, M. J.; Yoon, T.-U.; Kim, J.-H.; Bae, Y.-S., Low-temperature Cu (I) loading on a mesoporous Metal–Organic framework for adsorptive separation of C3H6/C3H8 mixtures. *Microporous Mesoporous Mater.* **2018**.

(205) Mahmood, A.; Xia, W.; Mahmood, N.; Wang, Q.; Zou, R., Hierarchical heteroaggregation of binary metal-organic gels with tunable porosity and mixed valence metal sites for removal of dyes in water. *Sci. rep.* **2015,** *5*, 10556.

(206) Jin, M.; Kim, S. S.; Kim, Y. D.; Park, J.-N.; Kim, J. H.; Ko, C. H.; Kim, J.-N.; Kim, J. M., Redox-buffer effect of Fe 2+ ions on the selective olefin/paraffin separation and hydrogen tolerance of a Cu+-based mesoporous adsorbent. *J. Mater. Chem. A* **2013,** *1*, 6653-6657.

(207) Martins, L. M.; Pombeiro, A. J., Tris (pyrazol-1-yl) methane metal complexes for catalytic mild oxidative functionalizations of alkanes, alkenes and ketones. *Coordin. Chem. Rev.* **2014,** *265*, 74-88.

(208) Lv, H.; Zhao, H.; Cao, T.; Qian, L.; Wang, Y.; Zhao, G., Efficient degradation of high concentration azo-dye wastewater by heterogeneous Fenton process with iron-based metal-organic framework. *J. Mol. Catal. A: Chem.* **2015,** *400*, 81-89.

(209) Yang, X.-j.; Xu, X.-m.; Xu, J.; Han, Y.-f., Iron oxychloride (FeOCl): an efficient Fenton-like catalyst for producing hydroxyl radicals in degradation of organic contaminants. *J. Am. Chem. Soc.* **2013,** *135*, 16058-16061.

(210) Van-Dunem, V.; Carvalho, A. P.; Martins, L.; Martins, A., Improved Cyclohexane Oxidation Catalyzed by a Heterogenized Iron (II) Complex on Hierarchical Y Zeolite through Surfactant Mediated Technology. *Chemcatchem* **2018,** *10*, 4058-4066.

(211) Kitagawa, S.; Kitaura, R.; Noro, S., Functional porous coordination polymers. *Angew Chem Int Ed Engl* **2004,** *43*, 2334-75.

(212) Howarth, A. J.; Liu, Y.; Li, P.; Li, Z.; Wang, T. C.; Hupp, J. T.; Farha, O. K., Chemical, thermal and mechanical stabilities of metal–organic frameworks. *Nat Rev Mater* **2016,** *1*, 15018.

(213) Rowsell, J. L.; Yaghi, O. M., Metal–organic frameworks: a new class of porous materials. *Micropor Mesopor Mat* **2004,** *73*, 3-14.

(214) Ferey, G., Hybrid porous solids: past, present, future. *Chem Soc Rev* **2008,** *37*, 191-214.

(215) Jiang, N.; Deng, Z.; Liu, S.; Tang, C.; Wang, G., Synthesis of metal organic framework (MOF-5) with high selectivity for CO2/N2 separation in flue gas by maximum water concentration approach. *Korean J Chem Eng* **2016,** *33*, 2747-2755.

(216) Thornburg, N. E.; Thompson, A. B.; Notestein, J. M., Periodic Trends in Highly Dispersed Groups IV and V Supported Metal Oxide Catalysts for Alkene Epoxidation with H2O2. *Acs Catal* **2015,** *5*, 5077-5088.

(217) Thornburg, N. E.; Nauert, S. L.; Thompson, A. B.; Notestein, J. M., Synthesis−Structure–Function Relationships of Silica-Supported Niobium (V) Catalysts for Alkene Epoxidation with H2O2. *Acs Catal* **2016,** *6*, 6124-6134.

(218) Contreras, C. A.; Ignacio-de Leon, P. A. A.; Notestein, J. M., Synthesis of a family of peracid-silica materials and their use as alkene epoxidation reagents. *Micropor Mesopor Mat* **2016,** *225*, 289-295.

(219) Bregante, D. T.; Thornburg, N. E.; Notestein, J. M.; Flaherty, D. W., Consequences of Confinement for Alkene Epoxidation with Hydrogen Peroxide on Highly Dispersed Group 4 and 5 Metal Oxide Catalysts. *Acs Catal* **2018,** *8*, 2995-3010.

(220) Sreethawong, T.; Yamada, Y.; Kobayashi, T.; Yoshikawa, S., Catalysis of nanocrystalline mesoporous TiO2 on cyclohexene epoxidation with H2O2: Effects of mesoporosity and metal oxide additives. *J Mol Catal a-Chem* **2005,** *241*, 23-32.

(221) Jones, C. W., Applications of hydrogen peroxide and derivatives. *Royal Society of Chemistry* **2007**.

(222) Sheldon, R. A.; Van Bekkum, H., Fine chemicals through heterogeneous catalysis. *John Wiley & Sons* **2008**.

(223) Fan, W. B.; Wu, P.; Tatsumi, T., Unique solvent effect of microporous crystalline

titanosilicates in the oxidation of 1-hexene and cyclohexene. *J Catal* **2008,** *256*, 62-73.

(224) Agarwala, A.; Bandyopadhyay, D., The radical versus non-radical reactive intermediates in the Iron(III) porphyrin catalyzed oxidation reactions by hydroperoxides, hydrogen peroxide and iodosylarene. *Catal Lett* **2008,** *124*, 256-261.

(225) Langhendries, G.; De Vos, D. E.; Baron, G. V.; Jacobs, P. A., Quantitative sorption experiments on Ti-zeolites and relation with α-olefin oxidation by H2O2. *J Catal* **1999,** *187*, 453-463.

(226) Lee, J.; Farha, O. K.; Roberts, J.; Scheidt, K. A.; Nguyen, S. T.; Hupp, J. T., Metal–organic framework materials as catalysts. *Chem Soc Rev* **2009,** *38*, 1450-1459.

(227) Ahn, S.; Thornburg, N. E.; Li, Z.; Wang, T. C.; Gallington, L. C.; Chapman, K. W.; Notestein, J. M.; Hupp, J. T.; Farha, O. K., Stable Metal-Organic Framework-Supported Niobium Catalysts. *Inorg Chem* **2016,** *55*, 11954-11961.

(228) Leus, K.; Muylaert, I.; Vandichel, M.; Marin, G. B.; Waroquier, M.; Van Speybroeck, V.; Van der Voort, P., The remarkable catalytic activity of the saturated metal organic framework V-MIL-47 in the cyclohexene oxidation. *Chem Commun (Camb)* **2010,** *46*, 5085-7.

(229) Leus, K.; Vandichel, M.; Liu, Y. Y.; Muylaert, I.; Musschoot, J.; Pyl, S.; Vrielinck, H.; Callens, F.; Marin, G. B.; Detavernier, C.; Wiper, P. V.; Khimyak, Y. Z.; Waroquier, M.; Van Speybroeck, V.; Van der Voort, P., The coordinatively saturated vanadium MIL-47 as a low leaching heterogeneous catalyst in the oxidation of cyclohexene. *J Catal* **2012,** *285*, 196-207.

(230) Barthelet, K.; Marrot, J.; Riou, D.; Férey, G., A breathing hybrid organic–inorganic solid with very large pores and high magnetic characteristics. *Angew Chem Int Ed* **2002,** *41*, 281-284.

(231) Llewellyn, P.; Reinoso, F. R.; Rouqerol, J.; Seaton, N., Characterization of porous solids VII: proceedings of the 7th International Symposium on the Characterization of Porous Solids (COPS-VII), Aix-en-Provence, France, 26-28 May 2005. *Elsevier:* **2006** Vol. 160.

(232) Bae, Y. S.; Yazaydin, A. O.; Snurr, R. Q., Evaluation of the BET Method for Determining Surface Areas of MOFs and Zeolites that Contain Ultra-Micropores. *Langmuir* **2010,** *26*, 5475-5483.

(233) Khan, N. A.; Jun, J. W.; Jeong, J. H.; Jhung, S. H., Remarkable adsorptive performance of a metal-organic framework, vanadium-benzenedicarboxylate (MIL-47), for benzothiophene. *Chem Commun (Camb)* **2011,** *47*, 1306-8.

(234) Neumann, R.; Levin-Elad, M., Vanadium silicate xerogels in hydrogen peroxide catalyzed

oxidations. *Appl Catal A* **1995,** *122*, 85-97.

(235) Salavati, H.; Teimouri, A., Efficient Epoxidation of Alkenes with Hydrogen Peroxide and Electrochemical Behavior in Water Over Heteropolymolybdate/Silica Nanocomposite. *Int J Electrochem Sc* **2017,** *12*, 7829-7843.

(236) Reddy, J. S.; Liu, P.; Sayari, A., Vanadium containing crystalline mesoporous molecular sieves Leaching of vanadium in liquid phase reactions. *Appl Catal A* **1996,** *148*, 7-21.

(237) Kang, K.; Ahn, W., Physiochemical properties of transition metal-grafted MCM-48 prepared using matallocene precursors. *J Mol Catal. A:Chem* **2000,** *159*, 403-410.

(238) Tiozzo, C.; Palumbo, C.; Psaro, R.; Bisio, C.; Carniato, F.; Gervasini, A.; Carniti, P.; Guidotti, M., The stability of niobium-silica catalysts in repeated liquid-phase epoxidation tests: A comparative evaluation of in-framework and grafted mixed oxides. *Inorganica Chim Acta* **2015,** *431*, 190-196.

(239) Satterfield, C.; Stein, T., Decomposition of hydrogen peroxide vapor on relatively inert surfaces. *J Ind Eng Chem* **1957,** *49*, 1173-1180.

(240) Kwon, S.; Schweitzer, N. M.; Park, S.; Stair, P. C.; Snurr, R. Q., A kinetic study of vapor-phase cyclohexene epoxidation by H 2 O 2 over mesoporous TS-1. *J Catal* **2015,** *326*, 107-115.

(241) Feng, D.; Wang, K.; Wei, Z.; Chen, Y.-P.; Simon, C. M.; Arvapally, R. K.; Martin, R. L.; Bosch, M.; Liu, T.-F.; Fordham, S.; Yuan, D.; Omary, M. A.; Haranczyk, M.; Smit, B.; Zhou, H.-C., Kinetically tuned dimensional augmentation as a versatile synthetic route towards robust metal–organic frameworks. *Nature Communications* **2014,** *5*, 5723.

(242) Moden, B.; Zhan, B. Z.; Dakka, J.; Santiesteban, J. G.; Iglesia, E., Kinetics and mechanism of cyclohexane oxidation on MnAPO-5 catalysts. *Journal of Catalysis* **2006,** *239*, 390-401.

(243) Feng, H.; Elam, J. W.; Libera, J. A.; Pellin, M. J.; Stair, P. C., Oxidative dehydrogenation of cyclohexane over alumina-supported vanadium oxide nanoliths. *J Catal* **2010,** *269*, 421-431.

(244) Nauert, S. L.; Schax, F.; Limberg, C.; Notestein, J. M., Cyclohexane oxidative dehydrogenation over copper oxide catalysts. *J Catal* **2016,** *341*, 180-190.

(245) Nauert, S. L., Rosen, A. S., Kim, H., Snurr, R. Q., Stair, P. C., & Notestein, J. M., Evidence for copper dimers in low-loaded CuOx/SiO2 catalysts for cyclohexane oxidative dehydrogenation. *Acs Catal* **2018,** *8*, 9775-9789.